Ferromagnetic oxide multilayers investigated by magneto-optic Kerr effect and anomalous Hall effect

INAUGURAL-DISSERTATION

zur
Erlangung des Doktorgrades
der Mathematisch-Naturwissenschaftlichen Fakultät
der Universität zu Köln

vorgelegt von

Lin Yang

aus Liling, China

Köln 2022

Berichterstatter: Prof. Dr. Paul H. M. van Loosdrecht
Prof. Dr. Ioannis Giapintzakis

Vorsitzender der
Prüfungskommission: Prof. Dr. Jan Jolie
Beisitzender: Dr. Hamoon Hedayat

Tag der letzten mündlichen Prüfung: 06. Oct. 2022

Erklärung

"Ich versichere, dass ich die von mir vorgelegte Dissertation selbständig angefertigt, die benutzten Quellen und Hilfsmittel vollständig angegeben und die Stellen der Arbeit − einschließlich Tabellen, Karten und Abbildungen −, die anderen Werken im Wortlaut oder dem Sinn nach entnommen sind, in jedem Einzelfall als Entlehnung kenntlich gemacht habe; dass diese Dissertation noch keiner anderen Fakultät oder Universität zur Prüfung vorgelegen hat; dass sie − abgesehen von unten angegebenen Teilpublikationen − noch nicht veröffentlicht worden ist, sowie, dass ich eine solche Veröffentlichung vor Abschluss des Promotionsverfahrens nicht vornehmen werde. Die Bestimmungen der Promotionsordnung sind mir bekannt. Die von mir vorgelegte Dissertation ist von Prof. Dr. Paul H. M. van Loosdrecht betreut worden."

Köln, date 11.Jul.2022

sign here Lin Yang

Publications

1. L. Yang, L. Wysocki, J. Schöpf, L. Jin, A. Kovács, F. Gunkel, R. Dittmann, P. H. van Loosdrecht, and I. Lindfors-Vrejoiu, Origin of the hump anomalies in the Hall resistance loops of ultrathin $SrRuO_3/SrIrO_3$ multilayers, Phys. Rev. Materials 5, 014403 (2021).

2. L. Yang, L. Jin, L. Wysocki, J. Schöpf, D. Jansen, B. Das, L. Kornblum, P. H. van Loosdrecht, and I. Lindfors-Vrejoiu, Enhancing the ferromagnetic interlayer coupling between epitaxial $SrRuO_3$ layers, Phys. Rev. B, 104,064444 (2021).

Contents

Chapter 1 Introduction

Contents

Ferromagnetic multilayers have been the subject of intensive study due to their potential use in applications related to magnetic storage devices and spintronics, such as reading heads, sensors, magnetic random-access memories, topological quantum computing[1-5]. To realize these applications, the interest in the study of fundamental physics, like the anomalous Hall effect (AHE), magnetic coupling, and magnetic anisotropy, has been greatly stimulated[6-10]. Many researchers have studied these properties in the ferromagnetic multilayers with metallic spacers[11-19], the ferromagnetic oxide multilayers with insulating spacers or metal-insulator transition spacer should also be studied in detail due to their complex coupling between spin, charge, orbital, and lattice degrees of freedoms[20-23] and current-driven applications[20].

1.1 Motivation

In 2016, J. Matsuno *et al*.[24] reported that the skyrmions were discovered in $SrRuO_3/SrIrO_3$ ferromagnetic oxide heterostructures, which were produced by the strong interfacial Dzyaloshinskii-Moriya interaction (DMI) due to the broken spatial inversion symmetry and the strong spin-orbit coupling in $SrIrO_3$. The hump-like anomalies of anomalous Hall effect (AHE) resistance loops attributed to the manifestation of the topological Hall effect (THE) were treated as the proof of the presence of skyrmions. Furthermore, it has been reported that magnetic skyrmions can be used as an ideal information carrier due to their small size, particle properties, high density, high stability (even at room temperature), and low energy consumption[25-29]. The investigation of skyrmions in $SrRuO_3$-based films has been since 2016 a hot topic.

Stemming from J. Matsuno's work, there were lots of reports of the hump-like features observed in Hall resistance loops of a single layer[30-33], a variety of $SrRuO_3$ multilayer[34-43], and other multilayers, such as, $Tm_3Fe_5O_{12}/Pt$[44], Cr_2O_3/Pt[45], and $La_{0.7}Sr_{0.3}MnO_3/SrIrO_3$[46] bilayers. However, the interpretation of these hump-like features in AHE resistance loops as a fingerprint of the THE contribution due to skyrmions has been under debate for several years. Because the origin of hump-like features in AHE loops can be explained both by the two-channel AHE model[37,40-42] and the magnetic skyrmions induced THE[34,47]. Thus, in my Ph.D work I aimed to figure out whether the hump-like features in AHE loops can experimentally confirm the presence of skyrmions or not.

Besides, the magnetic coupling between magnetic layers in a multilayer system has attracted much attention because of the application areas of magnetic recording, sensors, and spin electronics[48]. Moreover, the exchange coupling together with the epitaxial strain induced by the substrate and the interactions at the coherent epitaxial interfaces can work as knobs to modify or control the magnetic properties of the multilayer system. The type (ferromagnetic or antiferromagnetic) of magnetic layers, their magnetic properties and the spacer layers' thickness and physical properties determine the magnetic interlayer coupling (IC) in a multilayer system[49].

Most studies of magnetic interlayer coupling in multilayers selected spacers with metallic properties instead of insulating spacers since the former shows the possibility of bringing a stronger magnetic coupling than the latter. The magnetic coupling in the samples with insulating spacers tends to decay with the thickness of the spacers, while the magnetic coupling in metallic spacer show coupling strength oscillation with the spacer thickness[50]. However, in some particular cases, strong interlayer coupling with insulating spacers is desired, since the weak coupling is not beneficial to investigate and control the magnetic domains. For instance, when one expects to obtain the stable and electric field-driven magnetic skyrmions in $SrRuO_3$ layers sandwiched between two different non-magnetic large spin-orbit coupling oxides, the spacer should be poorly conducting[49]. Different spacers, such as $SrTiO_3$, $La_{0.7}Sr_{0.3}MnO_3$, and $SrIrO_3$[49,51,52], were chosen to achieve this goal. However, decoupling or weak ferromagnetic coupling was proved. Based on this, I will search for a solution to enhance the interlayer coupling in a $SrRuO_3$-based multilayer system.

Lastly, magnetic anisotropy (MA) is another important property of magnetic materials and relevant for technological applications. And materials with different strength of magnetic anisotropy can be used for different applications. More precisely, the materials with high, medium, or low MA can be fabricated by the permanent magnets, information storage media, or magnetic cores in transformers and magnetic recording heads, respectively[53]. The magnetic skyrmions are topologically nontrivial spin textures, and one can treat them as a unique magnetic domain structure that is determined by a competition between different magnetic interactions, i.e., magnetic anisotropy energy, DMI, spin-spin exchange energy, magnetic dipole-dipole interaction, and Zeeman energy. Therefore, magnetic anisotropy can be a tool to tune the stability of magnetic skyrmions[54,55]. Currently, most of the work has concentrated on the magnetic anisotropy of $SrRuO_3$ single crystal or single layer thin films, and few works focus on that of $SrRuO_3$-based multilayers due to the more complex coupling between spin, charge, orbital, and lattice degrees of freedoms and interaction at interfaces[56,57]. For instance, finding an excellent spacer layer to tune the magnetic anisotropy of $SrRuO_3$ multilayers is challenging[49,51,52]. Here I am addressing how this is affected by making epitaxial multilayers of $SrRuO_3$ with $LaNiO_3$ spacers of different thickness.

1.2 Scope of this thesis

In this thesis, to promote theoretical research and the potential application of the unique physical properties of ferromagnetic oxide multilayers, I will focus on investigating the origin of hump-like features in the AHE, the way to enhance the magnetic anisotropy, and tailoring the magnetic anisotropy in $SrRuO_3$ multilayers. A brief overview of the next chapters of this thesis is given below:

Chapter 2: In this chapter, the fundamental properties, including the crystal structure, magnetic and electronic properties of the individual layers and substrates of the $SrRuO_3$ (SRO)-based heterostructures, i.e., $SrRuO_3$, $SrIrO_3$, $LaNiO_3$, and $SrTiO_3$ are given first.

The fundamental physical phenomena of magnetic anisotropy, interlayer magnetic coupling, and the anomalous Hall effect are treated first. Subsequently, the theory of the magneto-optic Kerr effect is discussed, which is used to investigate the magnetic properties of the samples.

Chapter 3: This chapter introduces the experimental methods. All the samples were prepared by pulsed laser deposition. The analytic techniques, including reflective high-energy electron diffraction (RHEED), the magneto-optic Kerr effect (MOKE), the atomic force microscopy (AFM), magneto-transport measurements, superconducting quantum interference device (SQUID) magnetometry, and x-ray magnetic circular dichroism (XMCD) measurement for the sample were described.

Chapter 4: This chapter focuses on the origin of the hump anomalies in the Hall resistance loops of ultrathin $SrRuO_3/SrIrO_3$ multilayers. We deliberately considered the $SrIrO_3/SrRuO_3/SrIrO_3$ epitaxial trilayers and multilayers to eliminate, or at least minimize, the role of interfacial Dzyaloshinskii-Moriya interaction (DMI). In a perfectly symmetric ultra-thin film heterostructure, the interfacial DMI should be canceled entirely. Indeed, our $SrIrO_3/SrRuO_3/SrIrO_3$ trilayer samples did not exhibit any hump-like anomalies in the Hall-effect loops. Conversely, hump-like anomalies were observed over an extensive temperature range in the Hall effect loops of the multilayer samples, in which a $SrRuO_3/SrIrO_3$ bilayer was stacked thrice or six times, and the origin of the Hall effect loops with hump anomalies is discussed.

Chapter 5: This chapter presents the enhancing of the magnetic interlayer coupling between two epitaxial ferromagnetic $SrRuO_3$ layers separated by ultrathin $LaNiO_3$ in epitaxial heterostructures. The goal was to ensure the ferromagnetic coupling of two $SrRuO_3$ layers separated by a non-ferromagnetic spacer so that the field values for the reversal of the magnetization of the two layers become identical. Findings revealed that the ferromagnetic $SrRuO_3$ layers separated by two monolayers thick $LaNiO_3$ (about 0.8 nm), exhibited a weak interlayer coupling. However, the coupling becomes strongly ferromagnetic when the $LaNiO_3$ spacer is four monolayers thick and there is a reversal of the magnetization of the two $SrRuO_3$ layers at a common value of the perpendicular magnetic field. The enhancement of the magnetic interlayer coupling affected by the conductivity of the $LaNiO_3$ layer was confirmed.

Chapter 6: This chapter investigates the tailoring of magnetic anisotropy and magnetotransport of $SrRuO_3/LaNiO_3$ multilayers. Since the tailoring of magnetic anisotropy and dipolar interactions in multilayers tends to stabilize the skyrmions, multilayers are often a better candidate for achiving this. The magnetic anisotropy was studied using SQUID magnetometry, where in-plane and out-of-plane magnetization of the multilayers could be measured. The magnetotransport was studied with a homemade setup, which can measure the Hall effect and the MOKE simultaneously. We found that the magnetic anisotropy of the $LaNiO_3/SrRuO_3$ multilayers changes from in-plane to out-of-plane with the decrease in the $LaNiO_3$ spacer layer from 4 monolayers

(MLs) to 2 MLs. The contribution of the octahedral tilt angles and the bond lengths in conjunction with the interlayer coupling are the possible causes for the effective tailoring of magnetic anisotropy.

Chapter 7: This chapter will summarize the main results and show the contribution of this thesis, including drawing a conclusion and giving an outlook of my work.

1.3 References

[1] S. Yu, J. Tang, Y. Wang, F. Xu, X. Li, and X. Wang, Science and Technology of Advanced Materials **23** (1), 140 (2022).

[2] A. Hirohata, K. Yamada, Y. Nakatani, I.-L. Prejbeanu, B. Diény, P. Pirro, and B. Hillebrands, Journal of Magnetism and Magnetic Materials **509**, 166711 (2020).

[3] J. Anthony C. Bland, *Ultrathin Magnetic Structures I: An Introduction to the Electronic, Magnetic and Structural Properties*. (Springer Science & Business Media, 1994).

[4] X. Zhang, Y. Zhou, K. M. Song, T.-E. Park, J. Xia, M. Ezawa, X. Liu, W. Zhao, G. Zhao, and S. Woo, Journal of Physics: Condensed Matter **32** (14), 143001 (2020).

[5] P. Grünberg, Journal of Physics: Condensed Matter **13** (34), 7691 (2001).

[6] Y. Ijiri, Journal of Physics: Condensed Matter **14** (37), R947 (2002).

[7] P. J. van der Zaag and Julie A. Borchers.

[8] X. Chen, Q. Wu, L. Zhang, Y. Hao, M.g-G. Han, Y. Zhu, and X. Hong, Applied Physics Letters **120** (24), 242401 (2022).

[9] M. Glas, D. Ebke, I. M. Imort, P. Thomas, and G. Reiss, Journal of Magnetism and Magnetic Materials **333**, 134 (2013).

[10] C. Rizal, B. Moa, and B. B. Niraula, Magnetochemistry **2** (2) (2016).

[11] J. C. Slonczewski, Journal of Magnetism and Magnetic Materials **247** (3), 324 (2002).

[12] P. Ruiz-Díaz, T. R. Dasa, and V. S. Stepanyuk, Phys Rev Lett **110** (26), 267203 (2013).

[13] Y. Liu, J. Zhang, S. Jiang, Q. Liu, X. Li, and G. Yu, Journal of Magnetism and Magnetic Materials **420**, 70 (2016).

[14] P. Zhang, K. Xie, W. Lin, D. Wu, and H. Sang, Applied Physics Letters **104** (8), 082404 (2014).

[15] T. H. Dang, Q. Barbedienne, D. Q. To, E. Rongione, N. Reyren, F. Godel, S. Collin, J. M. George, and H. Jaffrès, Phys Rev B **102** (14), 144405 (2020).

[16] S. Chen, Y. Xiao, W. H. Xie, Z. Zhang, B. Ma, and Q. Y. Jin, Applied Physics Letters **105** (26), 262403 (2014).

[17] F. Stobiecki, M. Urbaniak, M. Tekielak, B. Szymański, T. Luciński, M. Schmidt, and A. Maziewski, Journal of Magnetism and Magnetic Materials **310** (2, Part 3), 2292 (2007).

[18] J. W. Knepper and F. Y. Yang, Phys Rev B **71** (22), 224403 (2005).

[19] M. Carbucicchio, M. Rateo, G. Ruggiero, and G. Turilli, Journal of Magnetism and Magnetic Materials **242-245**, 601 (2002).

[20] Y. Ohuchi, J. Matsuno, N.Ogawa, Y. Kozuka, M. Uchida, Y. Tokura, and M. Kawasaki, Nature Communications **9** (1), 213 (2018).

[21] C. L. Platt, M. R. McCartney, F. T. Parker, and A. E. Berkowitz, Phys Rev B **61** (14), 9633 (2000).

[22] M. Ziese, I. Vrejoiu, and D. Hesse, Phys Rev B **81** (18), 184418 (2010).

[23] Y. Gu, Q. Wang, W. Hu, W. Liu, Z. Zhang, F. Pan, and C. Song, Journal of Physics D: Applied Physics **55** (23), 233001 (2022).

[24] J. Matsuno, N.Ogawa, K. Yasuda, F. Kagawa, W. Koshibae, N. Nagaosa, Y. Tokura, and M. Kawasaki, Science Advances **2** (7), e1600304.

[25] A. Fert, N. Reyren, and V. Cros, Nature Reviews Materials **2** (7), 17031 (2017).

[26] K. Everschor-Sitte, J. Masell, R. M. Reeve, and M. Kläui, Journal of Applied Physics **124** (24), 240901 (2018).

[27] E. Y. Vedmedenko, R. K. Kawakami, D. D. Sheka, P. Gambardella, A. Kirilyuk, A. Hirohata, C. Binek, O. Chubykalo-Fesenko, S. Sanvito, B. J. Kirby, J. Grollier, K. Everschor-Sitte, T. Kampfrath, C. Y. You, and A. Berger, Journal of Physics D: Applied Physics **53** (45), 453001 (2020).

[28] S. Luo and L. You, APL Materials **9** (5), 050901 (2021).

[29] Z. Ma and L. Li, physica status solidi (a) **219** (1), 2100333 (2022).

[30] M. Nakamura, D. Morikawa, X. Yu, F. Kagawa, T.-H. Arima, Y. Tokura, and M. Kawasaki, Journal of the Physical Society of Japan **87** (7), 074704 (2018).

[31] P. Zhang, A. Das, E. Barts, M. Azhar, L. Si, K. Held, M. Mostovoy, and T. Banerjee, Physical Review Research **2** (3), 032026 (2020).

[32] Q. Qin, L. Liu, W. Lin, X. Shu, Q. Xie, Z. Lim, C. Li, S. He, G. M. Chow, and J. Chen, Advanced Materials **31** (8), 1807008 (2019).

[33] S. D. Seddon, D. E. Dogaru, S. J. R. Holt, D. Rusu, J. J. P. Peters, A. M. Sanchez, and M. Alexe, Nature Communications **12** (1), 2007 (2021).

[34] L. Wang, Q. Feng, Y. Kim, R. Kim, K.i H. Lee, S. D. Pollard, Y. J. Shin, H. Zhou, W. Peng, D. Lee, W. Meng, H. Yang, J. H. Han, M. Kim, Q. Lu, and T. W. Noh, Nature Materials **17** (12), 1087 (2018).

[35] D. Zheng, Y.-W. Fang, S. Zhang, P. Li, Y. Wen, B. Fang, X. He, Y. Li, C. Zhang, W. Tong, W. Mi, H. Bai, H. N. Alshareef, Z.Q. Qiu, and X. Zhang, ACS Nano **15** (3), 5086 (2021).

[36] E. Skoropata, A. R. Mazza, A. Herklotz, J. M. Ok, G. Eres, M. Brahlek, T. R. Charlton, H. N. Lee, and T. Z. Ward, Phys Rev B **103** (8), 085121 (2021).

[37] L. Wysocki, J. Schöpf, M. Ziese, L. Yang, A. Kovács, L. Jin, R. B. Versteeg, A. Bliesener, F. Gunkel, L. Kornblum, R. Dittmann, P. H. M. van Loosdrecht, and I. Lindfors-Vrejoiu, ACS Omega **5** (11), 5824 (2020).

[38] L. Wu, F. Wen, Y. Fu, J. H. Wilson, X. Liu, Y. Zhang, D. M. Vasiukov, M. S. Kareev, J. H. Pixley, and J. Chakhalian, Phys Rev B **102** (22), 220406 (2020).

[39] G. Kim, K. Son, Y. E. Suyolcu, L. Miao, N. J. Schreiber, H. P. Nair, D. Putzky, M. Minola, G. Christiani, P. A. van Aken, K. M. Shen, D. G. Schlom, G. Logvenov, and B. Keimer, Physical Review Materials **4** (10), 104410 (2020).

[40] G. Kimbell, P. M. Sass, B. Woltjes, E. K. Ko, T. W. Noh, W. Wu, and J. W. A. Robinson, Physical Review Materials **4** (5), 054414 (2020).

[41] A. Gerber, Phys Rev B **98** (21), 214440 (2018).

[42] D. Kan, T. Moriyama, K. Kobayashi, and Y. Shimakawa, Phys Rev B **98** (18), 180408 (2018).

[43] L. Wang, Q. Feng, H. G. Lee, E. K. Ko, Q. Lu, and T. W. Noh, Nano Letters **20** (4), 2468 (2020).

[44] A. S. Ahmed, A. J. Lee, N. Bagués, B. A. McCullian, A. M. A. Thabt, A. Perrine, P.-K. Wu, J. R. Rowland, M. Randeria, P. C. Hammel, D. W. McComb, and F. Yang, Nano Letters **19** (8), 5683 (2019).

[45] Y. Cheng, S. Yu, M. Zhu, J. Hwang, and F. Yang, Physical Review Letters **123** (23), 237206 (2019).

[46] Y. Li, L. Zhang, Q. Zhang, C. Li, T. Yang, Y. Deng, L. Gu, and D. Wu, ACS Applied Materials & Interfaces **11** (23), 21268 (2019).

[47] K.-Y. Meng, A. S. Ahmed, M. Baćani, A.-O. Mandru, X. Zhao, N. Bagués, B. D. Esser, J. Flores, D. W. McComb, H. J. Hug, and F. Yang, Nano Letters **19** (5), 3169 (2019).

[48] W. Liu, X.-H. Liu, W.-B. Cui, W.-J. Gong, and Z.-D. Zhang, Chinese Physics B **22** (2), 027104 (2013).

[49] L. Wysocki, R. Mirzaaghayev, M. Ziese, L. Yang, J. Schöpf, R. B. Versteeg, A. Bliesener, J. Engelmayer, A. Kovács, L. Jin, F. Gunkel, R. Dittmann, P. H. M. van Loosdrecht, and I. Lindfors-Vrejoiu, Applied Physics Letters **113** (19), 192402 (2018).

[50] M. D. Stiles, Journal of Magnetism and Magnetic Materials 200 (1), 322 (1999).

[51] M. Ziese, I. Vrejoiu, E. Pippel, P. Esquinazi, D. Hesse, C. Etz, J. Henk, A. Ernst, I. V. Maznichenko, W. Hergert, and I. Mertig, Physical Review Letters **104** (16), 167203 (2010).

[52] G. Herranz, B. Martínez, J. Fontcuberta, F. Sánchez, M. V. García-Cuenca, C. Ferrater, and M. Varela, Journal of Applied Physics **93** (10), 8035 (2003).

[53] M. T. Johnson, P. J. H. Bloemen, F. J. A. den Broeder, and J. J. de Vries, Reports on Progress in Physics **59** (11), 1409 (1996).

[54] S. W. Cho, S. G. Jeong, H. Y. Kwon, S. Song, S. Han, J. H. Han, S. Park, W. S. Choi, S. Lee, and Jun W. Choi, Acta Materialia **216**, 117153 (2021).

[55] X. S. Wang, H. Y. Yuan, and X. R. Wang, Communications Physics **1** (1), 31 (2018).

[56] L. Landau, J. W. Reiner, and L. Klein, Journal of Applied Physics **111** (7), 07B901 (2012).

[57] H. Wang, G. Laskin, W. He, H. Boschker, M. Yi, J. Mannhart, and P. A. van Aken, Advanced Functional Materials **32** (22), 2108475 (2022).

Chapter 2 Materials and physical phenomena

Contents

To investigate the physical properties of $SrRuO_3$ heterostructures, it is pertinent to know the properties, specifically, the crystal structure, the magnetic properties, and the conductivity of individual layers and substrates. This chapter begins with a brief introduction to the oxides used in the experiments. Subsequently, the theory of the magneto-optic Kerr effect is explained, which is the basis of the investigation of the samples' magnetic properties.

2.1 $SrRuO_3$

Perovskite $SrRuO_3$-based thin films have been of significant interest to researchers for more than half a century due to their exotic properties, such as surprising itinerant ferromagnetism[1,2], metal-insulator transitions[3,4], tunable magnetic anisotropy[5,6], unusual transport properties[7-12], and interlayer coupling[13-16].

2.1.1 Structural Properties

Figure 2.1 shows the room temperature structure of $SrRuO_3$, which exhibits orthorhombic symmetry *Pbnm* (No. 62)[17], with lattice parameters a=5.5670 Å, b=5.5304 Å, and c=7.8446 Å. Relative to the thin-film standard ABO_3 perovskite structure, $SrRuO_3$ shows a slight rotation of the oxygen octahedra. The orthorhombic phase can be visualized by the rotation of the BO_6 (RuO_6) octahedra counterclockwise about the $[010]_{cubic}$ and $[001]_{cubic}$ directions and clockwise rotation about the $[100]_{cubic}$ direction of an ABO_3 cubic perovskite (pseudocubic with a_{pc}= 3.93 Å). These directions become inequivalent after rotation[18].

The structure of $SrRuO_3$ thin films can be affected by temperature. For example, the degree of orthorhombic distortion decreases with the decreasing temperature. The structure of a single crystal of SRO is cubic above 677 ℃. Between 677 ℃ and 547 ℃, it distorts slightly into a tetragonal phase, and below 547℃, it transfers to orthorhombic or pseudocubic structure, as shown in figure 2.2[18,19]. In addition, other factors, such as types of substrates and thickness of epitaxial thin films, i.e., strain-induced factors, are also prone to induce this structural transition[20-22].

2.1.2 Magnetic Properties

In magnetic physics, the magnetism originates from the magnetic moment or magnetic dipole of magnetic materials. The permanent magnetic moments arise from the spin magnetic moments of electrons and nucleus, and orbital magnetic moment of electrons. Moreover, the magnetic properties of materials are mainly introduced by the magnetic moments of the electrons. Since the magnetic moments of the nuclei of the atoms are typically thousands of times smaller than the magnetic moments of the electrons, thus, they can often be ignored.

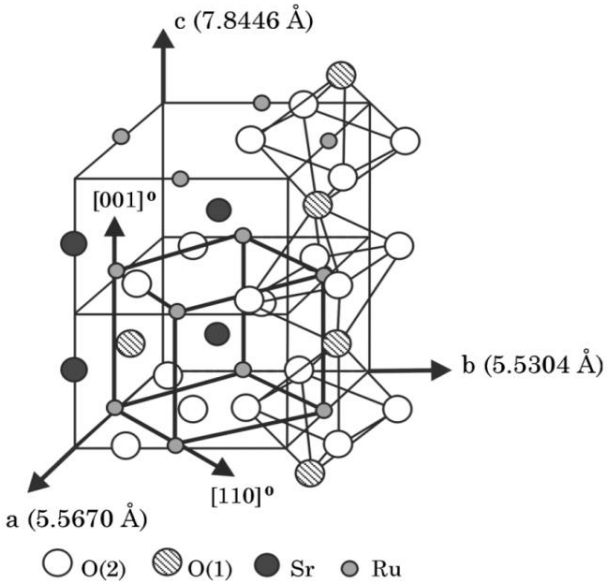

Figure 2.1: Schematic view of the orthorhombic unit cell of $SrRuO_3$. Reproduced with permission from Q. Gan *et al*., © 1999 American Institute of Physics[23].

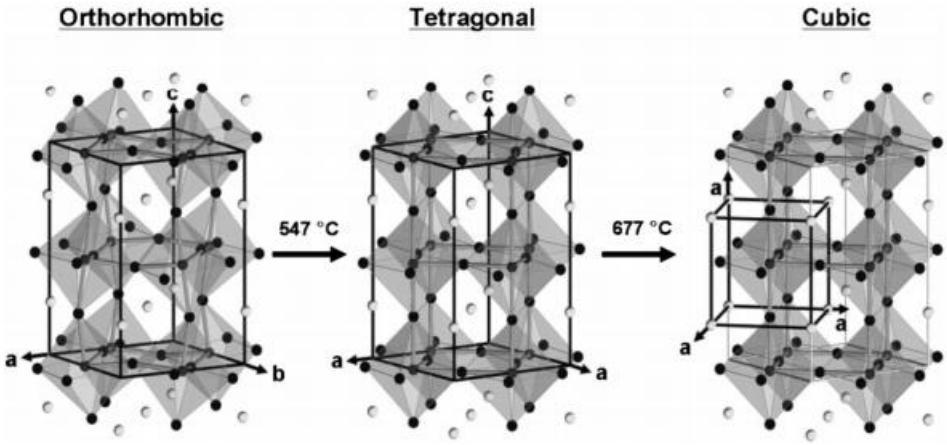

Figure 2.2: A sequence of phase transitions of unstrained bulk $SrRuO_3$ from orthorhombic to tetragonal and then cubic symmetry at 547 °C and 677 °C, respectively. The unit cell of the orthorhombic $SrRuO_3$ consists of four formula units of the ideal cubic perovskite structure. The Ru atoms occupy high-symmetry positions with respect to the orthorhombic shape of the cell. The O and Sr atoms are displaced from their high-symmetry positions due to the octahedral tilting. The tetragonal $SrRuO_3$ is a one-tilt system, where the RuO_6 octahedra are rotated only about the [001] direction. Gray, black, and white balls represent Ru, O, and Sr atoms, respectively. Reproduced with permission from K. J. Choi *et al*., © 2010 WILEY-VCH Verlag GmbH & Co. KGaA, Weinheim[24].

$SrRuO_3$ exhibits ferromagnetism which comes from the 4*d* electrons of the Ru ions[25]. It has a ferromagnetic transition temperature T_c of ~160 K in single crystals[26] and ~ 150 K in the thin films grown on the $SrTiO_3$ substrates[27]. The saturated magnetic moment of the SRO is ~1.6 μ_B/Ru atom, where μ_B is Bohr magneton[28].

2.1.2.1 Magnetic anisotropy

Magnetic anisotropy describes how an object's magnetic properties can depend on direction[29]. The magnetization direction depends on several contributions for magnetic thin films, such as shape anisotropy, magnetocrystalline anisotropy, growth-induced uniaxial anisotropy, magnetoelastic anisotropy, interface anisotropy, and exchange bias. These contributions define the energy density $\boldsymbol{E}$. The magnetization $\boldsymbol{M}$ is aligned in the direction for which $\boldsymbol{E}$ is minimized. For material with coherent rotation of the magnetization (i.e., the film has a mono-domain state and the magnitude of the magnetization vector is constant.), we can describe the energy density E by the classic Stoner-Wohlfarth model[30] as:

$$E = -H \bullet M + \sum_i E_i \qquad 2.1,$$

with Zeeman term $-\boldsymbol{H} \bullet \boldsymbol{M}$ and anisotropy contributions $\boldsymbol{E}_i$. For the minimum of $\boldsymbol{E}$ of isotropic media, magnetization $\boldsymbol{M}$ is aligned parallel to the external magnetic field $\boldsymbol{H}$. In anisotropic media, the anisotropy contributions change the energy landscape, and a different direction from $\boldsymbol{H}$ can be favored for $\boldsymbol{M}$. The magnetic anisotropy can originate from spin-orbit coupling and dipole-dipole interaction. The spin-orbit coupling is responsible for magneto-crystalline anisotropy and magnetoelastic anisotropy. The dipole-dipole interaction originates from the shape anisotropy[31]. For SRO thin films, the essential contributions to the magnetic anisotropy are magnetocrystalline anisotropy[32], magnetoelastic anisotropy[8].

(1) Magnetocrystalline anisotropy

A ferromagnetic material has magnetocrystalline anisotropy when the required energy for magnetization in a specific direction is larger than others. These directions are usually related to the principal axes of its crystal lattice.

The investigation of magnetocrystalline anisotropy of bulk or single-crystal SRO was made difficult by the lack of high-quality single crystals. In 1976, Kanbayasi reported that a crystal with a tetragonal phase has easy axes only in the (001) plane and an anisotropy field larger than 10 T. The strong magnetocrystalline anisotropy stems from the strong spin-orbit coupling of the heavy Ru ions[33]. After two years, he found crystals show pseudocubic anisotropy with the $[110]_{pc}$ directions (in the pseudocubic cell) being the easy axes and an anisotropy field of ~2 T[34].

For the thin films, the investigation of magnetocrystalline anisotropy gets more complex. For example, the twin-free $SrRuO_3$ films grown on miscut $SrTiO_3$ substrates show a single easy axis in the (001) plane. Above T_C, the easy axis is the b axis which is ~ 45° relative to the film normal[36]. Below T_C, there is an orientational transition[37] in which the easy axis continuously changes its angle with respect to the normal from ~ 45° to 30° at low temperatures, at a practically constant rate of ~ 0.1 deg/K[35] (see figure 2.3).

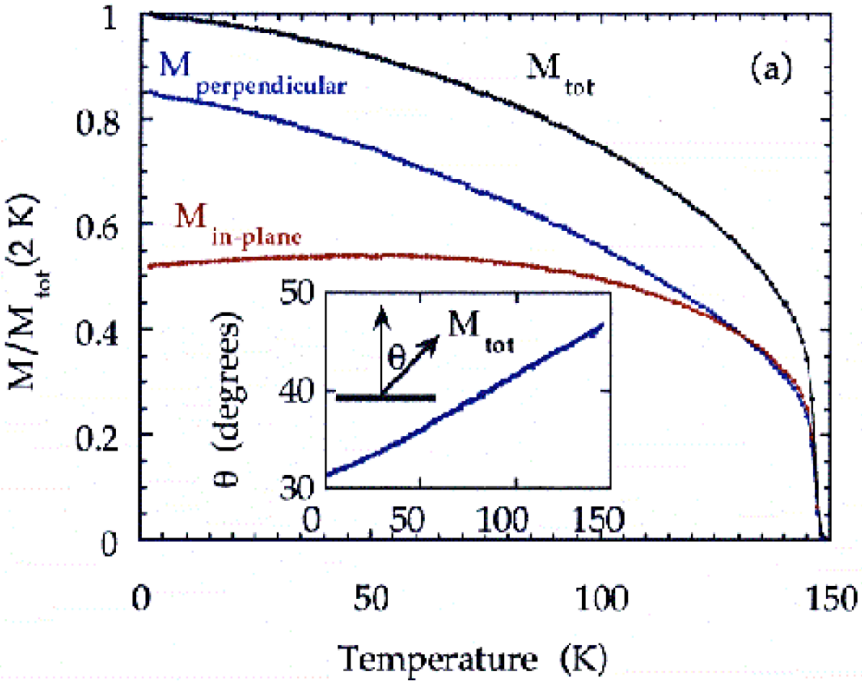

Figure 2.3: (a) Temperature dependence of the in-plane, out-of-plane, and total remanent magnetization of a $SrRuO_3$ film. The film was cooled in a saturating field down to 5 K and the magnetization was measured upon warming after removing the applied field. The temperature dependence of the angle between the magnetic moment and the normal to the film plane is also shown from Ref.[35] . Reproduced with permission from L. Klein *et al*., © 1996 *IOP Publishing Ltd*.

(2) Magnetoelastic anisotropy

Magnetoelastic anisotropy arises from the strain dependence of the anisotropy constants that causes magnetic materials to change their shape or dimensions during magnetization. To prevent lattice deformation in samples, stress must be applied. If the crystal is not subjected to stress, magnetostriction alters the effective magnetocrystalline anisotropy. Then, the magnetic anisotropy of the samples tends to be tailored.

It has been reported that in-plane compressive strain in $SrRrO_3$ coherently grown on $SrTiO_3$ (001) substrate has the easy magnetic axis normal to the surface and suppressed T_C of about 150 K[5]. However, the $SrRuO_3$ films grown on $Ba_{1-x}Sr_xTiO_3/BaTiO_3$ bilayer buffer layers with tunable in-plane lattice constant by changing the Ba/Sr ratio in the $Ba_{1-x}Sr_xTiO_3$ layer, the easy axis of magnetization isperpendicular to the surface in compressively strained films and rotates into the in-plane direction in strain-free films[38].

2.1.2.2 Magnetic interlayer coupling

This section introduced the theory of magnetic interlayer coupling based on Yasser Shokr's Ph.D. thesis (see details in section 3.3)[9].

The interlayer coupling between two ferromagnetic layers separated either by a non–magnetic or an antiferromagnetic spacer layer can be summarized as a competition between the following mechanisms[39]:

(a) Ruderman-Kittel-Kasuya-Yosida (RKKY) coupling from the correlation energy between two FM layers through the conduction electrons of the spacer layer[40-42].

(b) Direct exchange interaction at interface induced by the exchange bias between the FM layer and AFM layer[43-46].

(c) Magnetostatic interactions like orange-peel (Néel) coupling originating from the two neighboring ferromagnetic layers with rough interfaces[39,47], coupling by magnetostatic stray field due to magnetic domain structures[48] or from the sample edges in small-sized structures[49].

(d) Direct ferromagnetic coupling through pinholes[7,50,51].

These mechanisms will be described in more detail in the following subsections. In this thesis, the parallel coupling is assigned with a positive sign and antiparallel coupling as negative.

(1) RKKY

RKKY describes the magnetic layer as arrays of localized spin, which interact with conduction electrons via a contact exchange potential[43,52]. The dependence of the interlayer coupling on the spacer layer thickness originates from the change of density of states caused by the spin-dependent confinement of the electrons (or holes) in the quantum well when the magnetic films are aligned parallel. The spacer layers should be paramagnetic or diamagnetic to describe the magnetic coupling with the quantum well model and show metallic properties. Phenomenologically, the interlayer coupling energy per unit area is written as[43,53]:

$$J_{\mathrm{RKKY}} = -J_1 \cos(\theta) \qquad 2.2,$$

where "θ" is the angle between the magnetization directions of the two ferromagnetic layers, and J_1 is the interlayer coupling constant. An example of the explanation for the origin of RKKY interaction of the magnetic 3*d* transition metals and noble metals is shown in figure 2.4.

Figure 2.4 (a) shows the difference in the band structure of magnetic 3*d* transition metals and noble metal. In figure 2.4(b), the spin-up electrons can penetrate the whole stack with little reflection at the interface. The transition for the spin-down electrons is

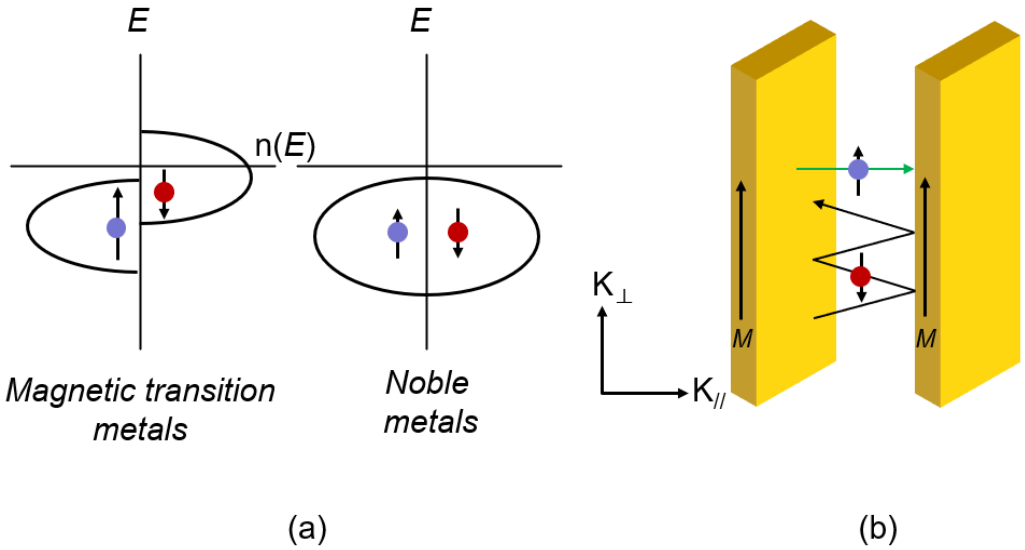

Figure 2.4: (a) Schematic for the density of the states (n(E)) in ferromagnetic 3*d* transition metals and noble metals. (b) Schematic to explain the origin of the RKKY interaction. The spin-up (↑) electron penetrates the whole stack with little reflection at the interfaces. The spin-down (↓) electron is reflected back and forth between the interfaces. The figures are adapted from Ref.[9].

reduced due to the splitting of the band in the magnetic films, which brings a high reflection for the electrons in the interlayer with spins opposite to the film magnetization and makes standing electron waves. The direction of motion of the electrons is perpendicular to the interfaces. Upon increasing the spacer thickness, the magnetic interlayer coupling shows an oscillatory thickness dependence. Since the discrete levels are shifted downwards with increasing the interlayer thickness, new levels come in and are populated upon crossing the Fermi energy (E_F). When such a new level just crosses E_F, this will increase the total electronic energy. Since the system tends to stay at a stable and lowest energy state, the magnetization direction of one layer will be changed from parallel to antiparallel. When the discrete levels become far below E_F, with low energy, a parallel alignment of magnetization directions will be more favorable.

(2) Coupling across antiferromagnetic layers

For an antiferromagnetic (AFM) layer as an interlayer spacer, the proximity effects will exist at the interfaces and the magnetic state of the antiferromagnetic spacer layer. That means both the exchange coupling at the AFM/FM interfaces and the internal exchange coupling within the AFM must be considered. Thus, atoms in AFM material have magnetic moments coupled to other atoms in AFM and FM. Moreover, the competition between the internal exchange coupling within the AFM and the FM/AFM interfacial interaction can lead to magnetic frustration, where not all the nearest-neighbor spins

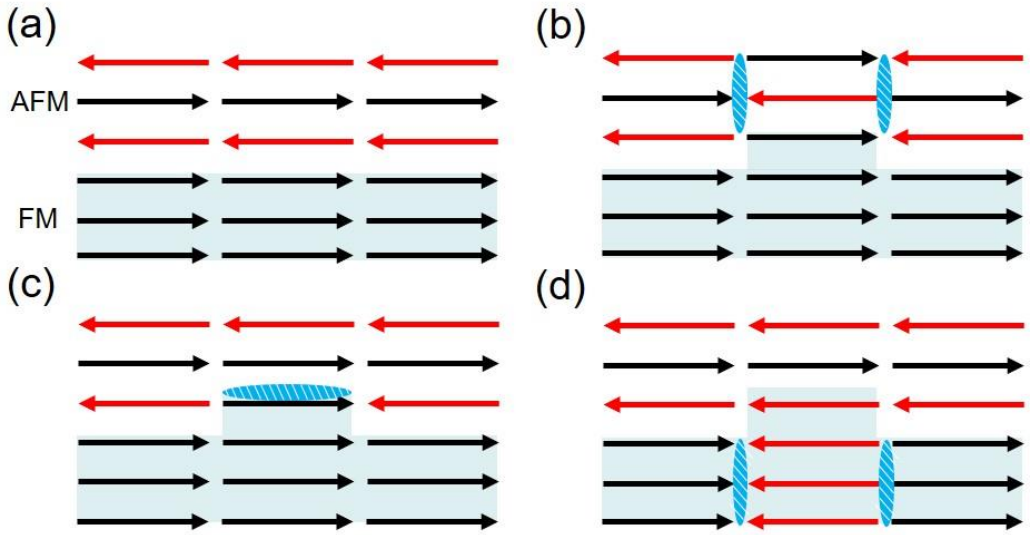

Figure 2.5: Spin frustration at an FM/AFM interface: (a) No frustration, perfect interface. (b) Frustration caused by a step in the AFM. (c) Frustration at the interface. (d) Frustration in the FM. The figures are adapted from Ref. [54].

can be in their local minimum energy configuration[54]. In addition, the spin configuration in the FM and AFM layers is affected by the interface roughness.

In figure 2.5, the different cases of the spin frustration configuration at an FM/AFM interface are illustrated. Figure 2.5 (a) is an example of perfect interfaces of simple layerwise AFM spin structure[55]. For this perfect interface, all pairs of spins are aligned along with their preferred spin directions, which causes a direction change for the spins in the AFM layers with each additional layer. In contrast, all spins in the FM layer are pointing in the same direction. When the sample shows thickness fluctuations, there will be a competition between the exchange coupling through the odd and even layers. In figure 2.5 (b), the FM-AFM interaction is frustrated in the AFM layer, where a step is at the interface. In contrast, in figure 2.5 (c-d), frustration occurs at the interface and within the FM layer. The local minimum energy configuration of the nearest neighbor determines where the frustration occurs. To be more specific, the frustration depends on the strength of the AFM-FM interactions, the thickness of the FM and AFM layers, the vertical and lateral extent of the interfacial defects, and system temperatures[55-57].

(3) Magnetostatic coupling

The magnetostatic coupling usually is smaller than the exchange interaction in bulk magnetic materials, while in a magnetic film with finite lateral extension, the magnetostatic coupling can play an essential role and strongly affect its magnetic properties. The “magnetic poles” are generated at the surface of the magnetic film,

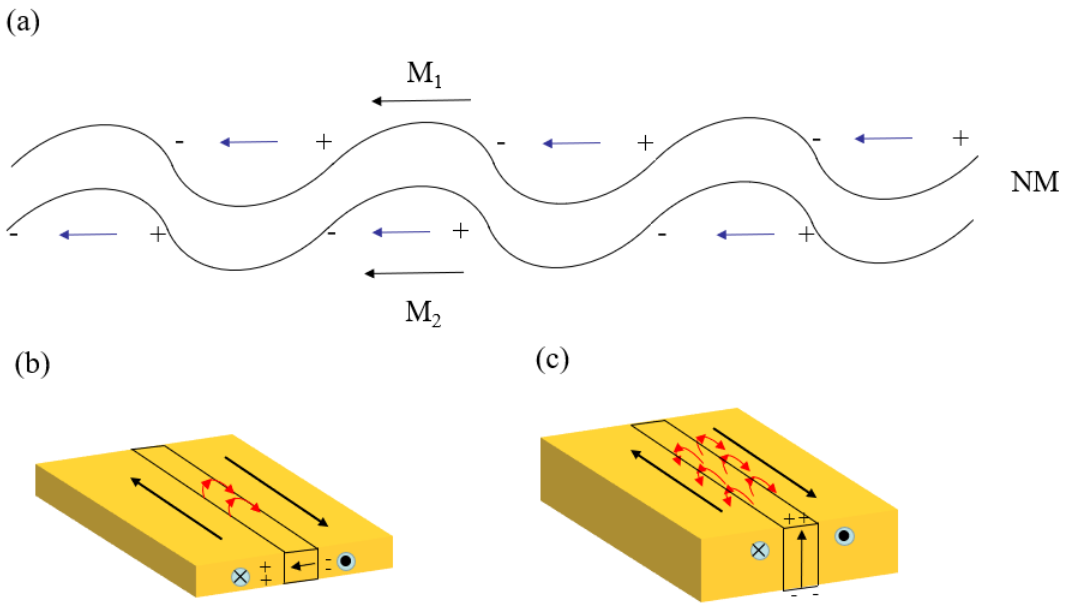

Figure 2.6: Schematic representation of (a) Néel's "orange–peel" coupling in ferromagnetic layers separated by nonmagnetic spacers, and (b) Néel wall and (c) Bloch wall coupling in single layer film. The figures are adapted from Ref.[9].

which brings a demagnetizing field. The distribution of these poles will affect the demagnetizing field. That means the strength of the demagnetizing field can be tuned by the geometry and the magnetization of the FM layer.

According to the resources, the magnetostatic coupling is divided into two types, i.e., Néel "orange-peel" coupling and domain walls induced coupling. The first one is generated between two neighboring FM layers, which have correlated roughness. The dipoles are located at the protrusions and valleys of the interfaces. The magnetostatic interactions between the dipoles give rise to the parallel alignment of the respective magnetizations of the two FM layers. Besides, in the case of multilayers, these exposed poles tend to reduce the strength of the RKKY-like coupling. This kind of coupling is known as Néel "orange-peel" coupling and is surface roughness dependent, as shown in figure 2.6(a).

Another kind of magnetostatic coupling originates from domain walls (DWs), i.e., the Bloch wall and Néel wall, which is inspired by a single layer film with local magnetostatic interactions between domain boundaries, as shown in figures 2.6(b) and 2.6(c). Here, the DW is defined as the transition region at which the magnetization changes direction from one domain to the other. The stray field in the DW will exert a local force on an adjacent film in a multilayer structure. That can modify the structure and energy of the domain walls and introduce an effective attraction or repulsion between two domain walls in adjacent films.

The total energy of a domain wall includes the exchange, the anisotropy, and the magnetostatic energies, which determine the spin configuration in the domain wall. The Bloch walls will be present in very thick films or bulk materials, while the Néel walls will be in a thin film. The stray magnetic fields in the materials with Bloch wall and Néel walls will play a significant role in generating the magnetostatic coupling.

(4) Interlayer coupling through pinholes

This coupling mechanism explains the interlayer coupling between two magnetic layers, which are coupled through pinholes in the spacer layer. Let us give a simple case, for two FM layers separated by an inhomogeneous space layer, pinholes in the spacer can occur through which the FM layers are directly coupled. Furthermore, coupling through pinholes depends strongly on the quality of the layers and will decrease rapidly as the thickness increase of the spacer layer. Thus, it is necessary to consider the pinhole coupling for a system with thin spacer layers[58].

2.1.3 Magnetotransport

In this thesis, to investigate the magnetotransport properties of $SrRuO_3$-based films, the magnetic resistance (resistance change) measurement and anomalous Hall effect (AHE) measurement techniques are employed. The change of resistance and the generation of Hall voltage are modified by the classical Lorentz force, which acts on the charge carriers. Specifically, magnetoresistance is described as a dependence of the electrical resistance on an external magnetic field for a nonmagnetic or ferromagnetic material (often ferromagnetic), which reveals the scattering mechanisms of electrons. The AHE requires a combination of magnetic polarization and spin-orbit coupling to generate a finite Hall voltage even in the absence of an external magnetic field. In ferromagnetic materials, the AHE is quantum mechanics in nature (spin-orbit coupling) and connect the electronic properties with the magnetization[59,60].

2.1.3.1 Magnetoresistance

The magnetic resistance was discovered by William Thomson, later known as Lord Kelvin, in 1856[61]. He confirmed that the resistance of an iron conductor changed when submitted to an external magnetic field. When the magnetic field was applied along the conductor, the resistance increased by 0.2%, and when the field was perpendicular to the conductor, the resistance decreased by 0.4%. In addition, he did the same experiment with nickel. Moreover, he found that its resistance showed similar behaviors to nickel but the magnitude of the resistance was greater, which is defined as anisotropic magnetoresistance.

2.1.3.2 AHE

To study the AHE with Hall effect measurement, one must divide the Hall effect into different components, such as ordinary Hall effect, AHE, and topological effect (if possible).

The ordinary Hall effect was discovered in gold leaves by Edwin Hall in 1879[62]. It is the production of the Hall voltage across an electrical conductor that was transverse to an electric current in the conductor and to an applied magnetic field perpendicular to the current (see figure 2.7(a)). After that, the AHE was reported in ferromagnets such as Co and Ni, which is ten times larger than the nonmagnetic metal[63]. The transverse voltage ("anomalous" Hall voltage) is roughly proportional to the magnetization M_z while the ordinary voltage is proportional to the magnetic field (see figure 2.7(b)). Pugh[64] and Lippert[65] reported that the total Hall resistivity, ρ_{xy}, is given by an empirical formula:

$$\rho_{xy} = R_0 B_z + \mu_0 R_s M_z \qquad 2.3,$$

where R_0 is the ordinary Hall coefficient and it depends on the type and density of carriers. The R_s is the anomalous hall coefficient. Considering the magnetic H field is defined as:

$$H_{xy} = \frac{B_z}{\mu_0 \mu_r} - M_z \qquad 2.4.$$

The equation 2.3 can be rewritten as:

$$\rho_{xy} = \left(\frac{R_0}{\mu_0 \mu_r} \right) B_z + (R_s - R_0) M_z \qquad 2.5,$$

when B_z is small, the magnetization is not saturated, the second item dominated for the ρ_{xy}. When B_z is large enough and the magnetization gets saturated, the first item is the dominated contribution to ρ_{xy}. Thus, this provides us a simple way to distinguish the ordinary Hall effect and AHE.

Usually, the AHE simply can be divided into different types based on the origins:

(1) Intrinsic AHE

In 1954, Karplus and Luttinger[67] gave the first insight into the intrinsic AHE. They found that when applying an electric field to an ideal crystal with periodic intrinsic spin-orbit coupling, the electrons will acquire an additional contribution to their group

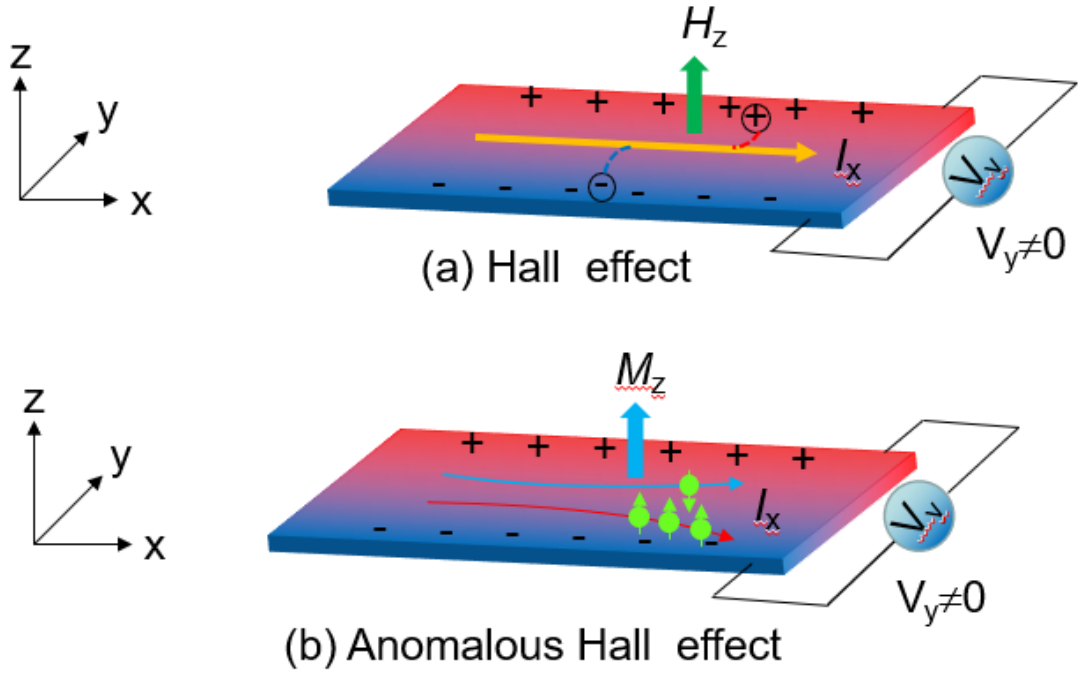

Figure 2.7: (a) Hall effect: the longitudinal current I_x under vertical external magnetic field Hz contributes to the transversal voltage V_y due to the Lorentz force experienced by the charge carriers. (b) Anomalous Hall effect (AHE): the electrons with majority and minority spin (due to spontaneous magnetization M_z) having opposite "anomalous velocity" due to spin-orbit coupling, which causes unbalanced electron concentration at two transversal sides and leads to finite voltage V_y. The figures are adapted from Ref.[66].

velocity (anomalous velocity). Moreover, the anomalous velocity is perpendicular to the field. The anomalous velocity from all occupied electrons in the opposite direction contributes to the anomalous Hall conductivity where the electron's spin is imbalanced, as shown in figure 2.8 (a). This contribution solely depends on the band structure of the system and is independent of scattering. Nowadays, this anomalous velocity is referred to as Berry-phase curvature after the introducing of the Berry phase concept. The cross-product of electric field and Berry-Phase curvature in momentum space moves the electrons of different spin in opposite perpendicular directions.

(2) Extrinsic AHE

In the above description for the intrinsic AHE from Karplus and Luttinger, the intrinsic AHE occurs in the absence of disorder which was criticized by Smit. He stated that the asymmetric scattering from impurities due to spin-orbit interactions was significant on the steady-state and hence for AHE, named skew scattering[69] (impurity scattering) (see figure 2.8(b)). After that, another impurity-induced AHE, side-jump induced AHE was reported by Berger[70] (see figure 2.8(c)).

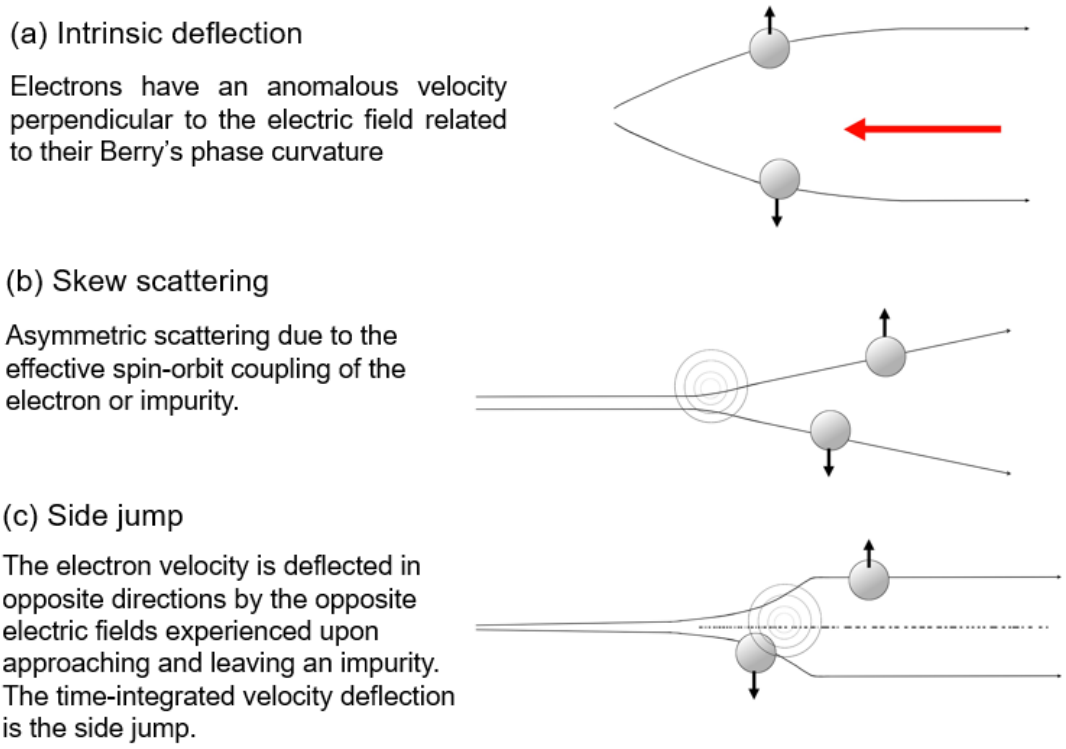

Figure 2.8: Three main mechanisms of AHE: (a) intrinsic deflection, (b) skew scattering, (c) and side jump that can give rise to an AHE. In any real material all these mechanisms act to influence electron motion. The figures are adapted from Ref.[68].

Skew-scattering can be described as that an electron changes its traveling direction, φ, from $\varphi = 0$ to $\varphi = \varphi'$ due to a magnetic scattering center, which ρ_{xy} is proportional to the ρ_{xx}, e.g., $\rho_{xy} \propto \rho_{xx}$ in a simple single-spin model. Here the direction (positive or negative) is determined by the time-reversal symmetry breaking induced by the magnetic moment, resulting in a net transverse current flow. The side-jump mechanism also relies on this symmetry breaking, but with the same propagation angle at the scattering center, so that ρ_{xy} is proportional to the ρ^2_{xx}, i.e., $\rho_{xy} \propto \rho^2_{xx}$. The electron wave-packet undergoes an effectively instantaneous change in position transverse to its travel direction. The direction of this scattering is spin-dependent.

Now, for a system with negligible phonon scattering, the AHE resistivity can be described as[71]:

$$\rho_{xy}^{A} = (\partial \rho_{xx0} + \beta \rho_{xx0}^{2}) + b\rho_{xx}^{2} \qquad 2.6,$$

where the coefficients α, β, and b are the skew scattering, side-jump, and intrinsic contributions to, respectively. The first two parameters depend on the impurity scattering in a specific sample, but parameter b is independent of scattering. Thus, it is possible to distinguish the skew and side-jump scattering from equation 2.6, but hard to experimentally distinguish the side-jump scattering and intrinsic scattering. In the

future, further investigation about how to separate the AHE into different contributions for a system with a negligible side-jump scattering is highly demanded.

The AHE in SRO has non-monotonic temperature dependence, and the origin of this behavior has been a matter of debate[72,73]. The debate centers on whether the AHE conductivity is driven by asymmetric scattering of impurities or by intrinsic effects due to band structure. Experimentally the resistivity dependence of the AHE can distinguish between different extrinsic contributions but not between intrinsic and extrinsic contributions. Intrinsic and extrinsic effects may be distinguishable by the zero-temperature limit of the AHE, but there is no consensus[74,75].

2.2 $SrTiO_3$ substrate

The substrates play a significant role in the growth of epitaxial films. The substrate should be a single crystal substrate. The choice of substrate is limited by various factors, such as crystal symmetry, orientation, minimum lattice parameter mismatch, surface energy consideration, surface termination, chemical nature, thermal expansion coefficient, and most importantly, the application for which the film is being deposited[76]. The growth of high-quality epitaxial materials requires that the substrates have structural and chemical compatibility with the desired film. Chemical incompatibility can lead to various interfacial reaction layers or interdiffusion of unwanted elements between the film and the substrate. Structural incompatibility, typically manifested through substrate lattice parameters with very different values from the film, or large differences in thermal expansion between the film and substrate, can significantly affect the film's structural and electrical properties.

To grow the high-quality $SrRuO_3$-based film, numerous substrate materials are available. Table 2.1 summarizes other substrate materials, including the unit-cell parameters, the resulting $SrRuO_3$ strain, and other critical physical properties[18,77]. The most common (and successful) substrate material used to deposit $SrRuO_3$ thin films is $SrTiO_3$. $SrTiO_3$ has a cubic perovskite unit cell with a lattice parameter of 3.905 Å, which provides good lattice matching with $SrRuO_3$. The SRO unit cell orientation, which lies close to the $[110]_{pc}$ ($[010]_o$) direction[78] tends to adopt that of the STO substrate to minimize the in-plane strain[79]. Here, the pseudocubic notation is used, indicated by a subscript pc. This provides us with an elegant tool for controlling the magnetocrystalline anisotropy of the SRO film without the requirement of ultrathin films, additional layers, or complex layer structures and device geometries.

In addition, a clean and well-defined surface is important for good thin film growth. Typically, the surface is cleaned using organic solvents (for example, acetone and ethanol), then annealed in oxygen at an elevated temperature. Also, the terminating layer of the substrate has a significant influence on the initial growth of a deposited thin film[19,80]. For the growth of high quality $SrRuO_3$ thin films, having singly terminated surfaces (either SrO or TiO_2 in the case of $SrTiO_3$) has been found

Table 2.1: A selection of frequently used oxide substrate materials and their structural and transport properties. $SrRuO_3$ strain is defined as $(d_l-d_s)/d_s$, where d_l and d_s refer to the bulk in-plane lattice parameters of $SrRuO_3$ layer and the substrate, respectively. The table is adapted from Ref.[18,77].

Substrate	Symmetry at 300 K	α (Å)	b (Å)	c (Å)	$SrRuO_3$ strain (%)	Transport properties
$LaAlO_3$	Cubic	3.82	3.82	3.82	2.61	Insulating
$SrTiO_3$	Cubic	3.905	3.905	3.905	0.446	Insulating
Nb doped $SrTiO_3$	Cubic	3.905	3.905	3.905	0.446	Conducting
$NdGaO_3$	Orthorhombic	5.43	5.50	7.71	1.72	Insulating
$DyScO_3$	Orthorhombic	5.44	5.71	7.89	-0.574	Insulating
$La_{0.18}Sr_{0.82}Al_{0.65}Ta_{0.35}O_3$ (LSAT)	Cubic	3.868	3.868	3.868	1.2	Insulating
Bulk $SrRuO_3$	Orthorhombic	5.567	5.53	7.845	-	Conducting

to be important. Fortunately, a method has been developed using an HF treatment to make the surface of $SrTiO_3$ singly terminated[81]. The method reliably yields a TiO_2-terminated surface with straight step edges.

2.3 $SrIrO_3$

2.3.1 Introduction to $SrIrO_3$

The Ruddlesden–Popper perovskite series of iridates $Sr_{n+1}Ir_nO_{3n+1}$ with strong spin orbit coupling (SOC) has attracted increasing interest in condensed matter physics and materials communities due to the observed or predicted versatile novel physics such as topological states[82], superconductivity[83], ferroelectricity[84], anomalous quantum Hall effect[85] and fractional quantum Hall effect[86].

A typical example, the perovskite $SrIrO_3$ ($n = \infty$), stands out since it has been theoretically proposed as a key building block for engineering topological phases at interfaces and in superlattices. For example, J. M. Carter *et al*. proposed that the $SrIrO_3$ has a Dirac node crossing at the Fermi level under the tight-binding Hamiltonian the frame of construction based on the $J_{eff} = 1/2$ single band model[87]. This Dirac node hosts electron carriers for the semimetal background state of SIO and can evolve into different kinds of topological states depending on the specific symmetry breaking[88].

From the insight of the experiment, J. Matsuno *et al*.[89] reported that topological phases could be realized SRO when it is interfaced with complex Ir oxides with very

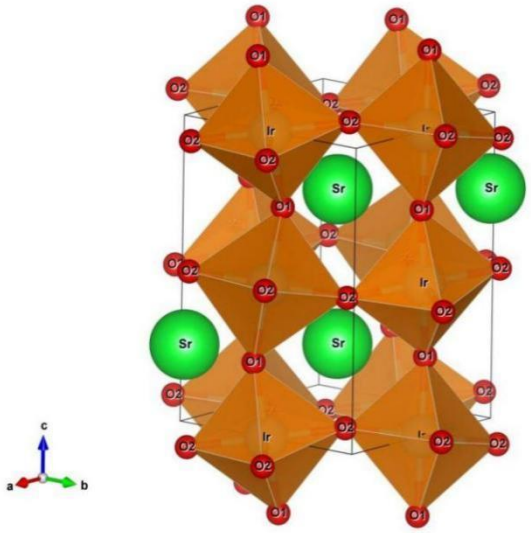

Figure 2.9: Schematic view of the orthorhombic unit cell of $SrIrO_3$. Sr, Ir and O atoms are shown in green, blue and red. The octahedra shown are rotated about the *c*–axis and tilted about [110]-axis.

strong spin-orbit coupling. They investigated the ferromagnet thickness dependence and stated that the broken inversion symmetry at the SRO/SIO interface and strong spin-orbit coupling of $SrIrO_3$ generated the interface DM interaction, then introducing the skyrmion phase.

2.3.2 Crystal structure properties

The structure of $SrIrO_3$ is orthorhombic with the space group *Pbnm* (No.62). The lattice parameters at room temperature are a = 5.56 Å, b = 5.59 Å, and c = 7.88 Å[90]. Each Ir atom is connected by six atoms of oxygen to create an IrO_6 octahedron (see figure 2.9). The nearest-neighbor IrO_6 octahedral tilt in the opposite sense about the [110] axis at about 12°. Moreover, they rotate around the c-axis at about 11° in the same direction if they are in different layers but the opposite direction. If they are in the same layers, resulting in a unit cell with four formula units. The tilting and rotation of the octahedra simultaneously cause unit cell distortion with two types of Ir–O–Ir angles, at 156.49(8)° and 153.7(5)°, respectively[91,92].

2.3.3 Conductivity and Magnetic properties

In the three-dimensional limit, the $SrIrO_n$ was considered as a narrow-band semimetal bordering a Mott transition due to a combination of strong SOC and electron correlations. Moreover, it was revealed to be a paramagnetic semimetal. Since the enhanced interlayer hopping induced by the three-dimensionality, compassion with Sr_2IrO_4 and $Sr_3Ir_2O_7$ (n=2), the J_{eff}= 1/2 band mixes the J_{eff}= 3/2 band at a certain extent in $SrIrO_3$[94,95] (see figure 2.10). The semimetallic ground state has been confirmed experimentally and theoretically[87,96]. It is of particular interest to achieve

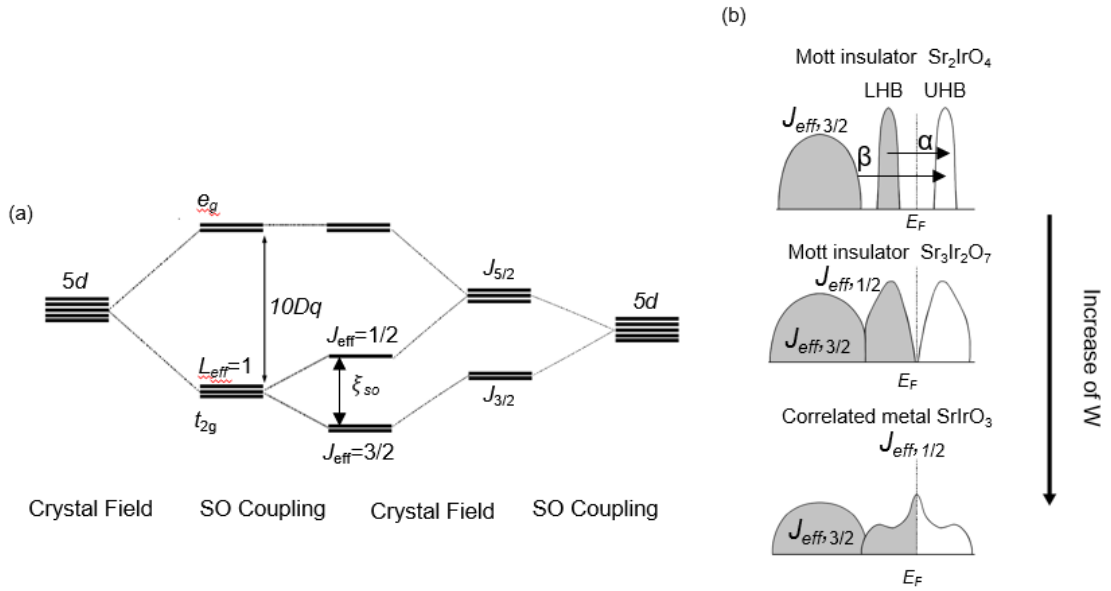

Figure 2.10: Electronic structure of orthorhombic $SrIrO_3$: (a) Orbit configuration of 5d5 with SOC and U[7]; (b) schematic picture of the band evolution with dimensionality increases in $S_{rn+1}Irn_{O3n+1}$ iridates. W represents the bandwidth. The α denotes the excitation of electrons from LHB to UHB, and the β for the excitation from J_{eff} = 3/2 band to the UHB, seen from the optical conductivity spectra[18]. The figure is adapted from Ref.[93].

the proposed topological and/or magnetic states via tuning the SOC, U (Coulomb repulsion), and/or lattice symmetry.

2.4 $LaNiO_3$

$LaNiO_3$ (LNO) is a perovskite oxide crystallizing in a three-dimensional nearly cubic structure with a small rhombohedral distortion (ß = 90.41°)[97,98]. It is reasonably well approximated by a pseudocubic cell with a = 3.838 Å. Like most of the rare-earth nickelates of the form $RENiO_3$ (RE = rare earth), which show a metal-insulator transition (MIT), the (001)-oriented LNO films possess an MIT for changing the thicknesses of t = 2-4 unit cells (u.c.)[99-103]. The conduction band of LNO and other perovskite nickelates ($RNiO_3$, where R is rate earth) is formed by the overlap of the Ni 3*d* orbitals and the O 2*p* orbitals. This overlap is correlated with the ionic radii of the rare earth and influenced by the temperature[104]. With decreasing temperatures, the NiO_6 octahedra buckle, and the overlap reduces, which results in a metal-insulator transition[105,106].

Besides, LNO lacks magnetic order in its bulk form since the Ni^{3+} ion has a low-spin $3d^{7}$ configuration with one electron in the higher energy. e.g., states. The conductivity of LNO is very sensitive to oxygen stoichiometry. The deficiency of oxygen during the fabrication process will lead to the creation of Ni^{2+} ions and deteriorate conductive properties. As for the film form of LNO, in most of the cases, it

was proven as paramagnetic[99,108]. However, H. Guo *et al*. reported that the crystals without Ni^{2+} impurities exhibit metallic properties and an unexpected but clear antiferromagnetic transition. M. K. Margaret *et al*. followed their work and confirmed the emergence of long-range magnetic ordering at the film-substrate interface in ultrathin (111)-oriented LNO thin films up to 26 u.c. by synchrotron x-ray diffraction, AHE measurement, and dynamical x-ray diffraction simulations[98].

2.5 Magneto-optic Kerr effect

2.5.1 Introduction to MOKE

The Kerr effect is described as the rotation of the plane of polarization of the incident light. This phenomenon was first reported by John Kerr in 1877 [41]. However, a similar effect was first discovered by Faraday in 1845[109], when he found out that the plane of polarization of light transmitted through a magnetic sample was rotated. The angle of polarization rotation observed in the Kerr and Faraday effect is dependent on the strength of the magnetization of the sample surface and the magnetization orientation of the sample surface with respect to the plane of incidence light. This influence of magnetization orientation can be described by the different magnetization geometries of the Kerr effect. The details will be discussed in subsection 2.5.5.

In general, the rotation effect of MOKE can be described in the form of a dielectric tensor which accounts for the effect of the magnetic medium. The dielectric law is given as:

$$\boldsymbol{D} = \boldsymbol{\varepsilon}_{ij}\boldsymbol{E} \qquad 2.7,$$

where ε is the dielectric permittivity tensor which connects the electric field vector $\boldsymbol{E}$ of the plane of the light wave along with $\boldsymbol{D}$, the induced electrical displacement vector. The generalized dielectric permittivity tensor[110] is given as:

$$\boldsymbol{\varepsilon}_{ij} = \varepsilon \begin{bmatrix} 1 & -iQ_v m_z & iQ_v m_y \\ iQ_v m_z & 1 & -iQ_v m_x \\ -iQ_v m_y & iQ_v m_x & 1 \end{bmatrix} + \begin{bmatrix} B_x m_x^2 & B_y m_x m_y & B_y m_x m_z \\ B_y m_x m_y & B_x m_y^2 & B_y m_y m_z \\ B_y m_x m_z & B_y m_y m_z & B_x m_z^2 \end{bmatrix} \qquad 2.8,$$

where Q_v is the Voigt constant in which it is material dependent that describes the magneto-optical rotation of the plane of polarization of light. This Voigt term is a complex material parameter that is to the first order proportional to the magnetization of the sample. B_x and B_y are constants describing the Voigt effect, and m_i are the components of the unit vector of magnetization along the cubic axis. Q_v, B_x and B_y are complex and not well known for the majority of materials. However, the real parts of these constants are the most dominant. By using the term in equation 2.7, the dielectric law can be generalized as follows:

$$\boldsymbol{D} = \varepsilon\left(\boldsymbol{E} + iQ_v\boldsymbol{m}\times\boldsymbol{E}\right) \qquad 2.9.$$

In equation 2.9, ε is the dielectric permittivity tensor, vector $\boldsymbol{D}$ represents the secondary light amplitude which is produced by the magneto-optic interaction between $\boldsymbol{E}$ and the magnetization vector $\boldsymbol{m}$ in the sample. From equation 2.9, the cross product, proves the gyroelectric nature of the Kerr effect and analogy to the Lorentz force. In general, what is observed in MOKE is the magneto-optic response of the medium which is in the form of a change in the polarization of the incident light. This change is made of two types, the change of the in-phase component of the reflected light causing a rotational change in the plane of polarization of the incident light and the out-of-phase change which causes the elliptical change to the polarization of incident light.

2.5.2 Polarization of light

According to Maxwell's theory, light is an electromagnetic wave[61]. It can be treated as a combination of transverse electric and magnetic fields travelling along the direction of propagation. The travelling electric and magnetic fields are defined as equations 2.9 and 2.10, respectively. Figure 2.11 shows an illustration of an electromagnetic wave[61].

$$E\ (r,t) = \varepsilon_p E_0 e^{i(k\times r-\omega t)} \qquad 2.10$$

$$B\ (r,t) = \frac{1}{c}\left(k_0\times\varepsilon_p\right)E_0 e^{i(k\times r-\omega t)} \qquad 2.11,$$

where ε_p is the unit polarization vector and $k = (\omega/c)$, k_0 is the wave vector along the direction of propagation. The electric field vector is named the polarization vector, which leads to the state of the polarization of the electromagnetic wave. Since the electric field vector consists of a rapid succession of different polarization states lying in the xy plane[61]. Natural light is called unpolarized. This means the electric field vector always has different orientations on this plane. The configurations of the electromagnetic wave can be linearly, circular, and elliptical polarization. When the electric field vector has a fixed orientation on the plane perpendicular to the propagation direction, the electromagnetic wave is linearly polarized. Other possible configurations are circular and elliptical polarization. The possible polarization of light is shown in figure 2.12.

When light impinges on a surface, the vectors along the propagation direction of the incoming and reflected beams define as the plane (scattering plane) of incident light[111]. If the light is linearly polarized on the plane of incidence, the light is called

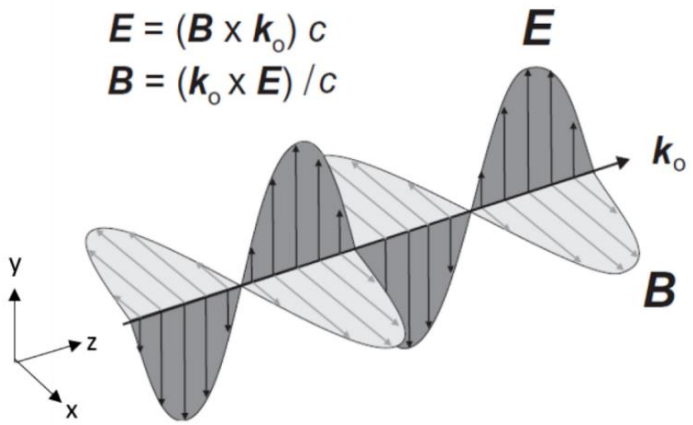

Figure 2.11: The schematic view of a traveling electromagnetic wave. The electric and magnetic field are transverse to each other and the propagation direction k_0. The electric field vector is named the polarization vector as it defines the polarization state of the electromagnetic wave. The figure is adapted from Ref.[61].

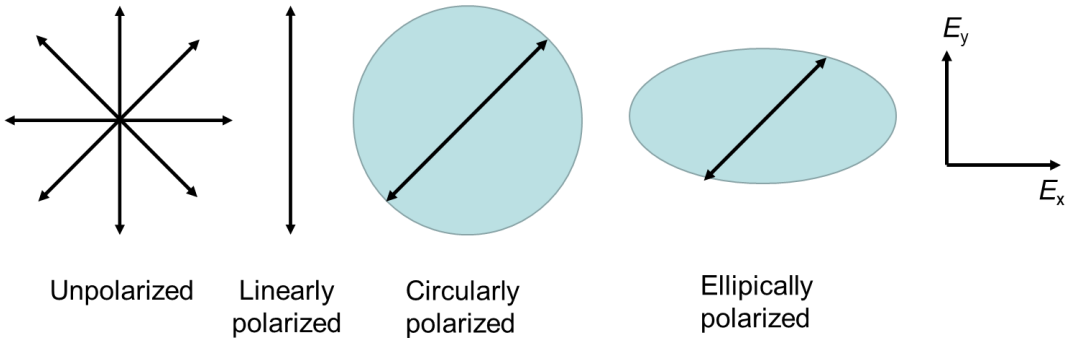

Figure 2.12: Possible polarization states of light. The figure is adapted from Ref.[9].

p-polarized (from parallel). If the light is linearly polarized perpendicular to the plane of incidence, it generates called *s*-polarized light (see figure 2.13).

2.5.3 Definition of the magneto-optical Kerr effect

When s- or p-polarized light is reflected from a magnetic film, its polarization becomes elliptic, and the principal polarization axis is rotated[61]. These two consequences, Kerr ellipticity and Kerr rotation, make up the magneto-optical Kerr effect, as shown in figure 2.15.

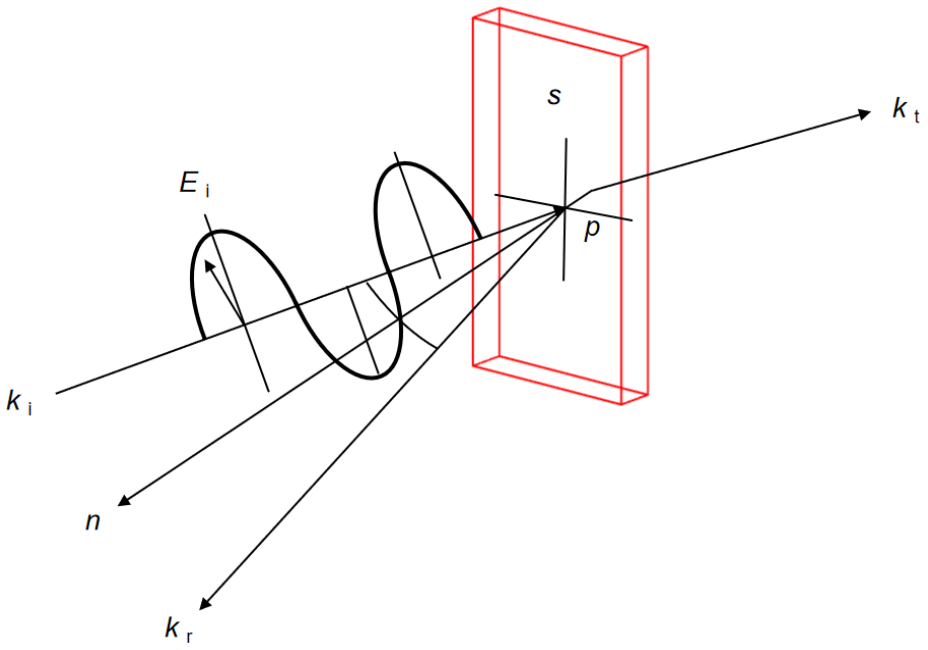

Figure 2.13: Light being refracted from a medium, with the s- and p-polarization directions defined. The k_i and k_r vectors define the plane of incidence. The figure is adapted from Ref.[115].

The angle φ in figure 2.14 represents the Kerr rotation and denotes the rotation of the major axis with respect to its original polarization direction. The Kerr rotation is given by equation 2.16:

$$\tan 2\varphi = \frac{2E_{0x}E_{0y}\cos\varphi}{E_{0x}^2 - E_{0y}^2} \qquad 2.12,$$

where E_{0x} and E_{0y} denote the electric field amplitudes of the linearly polarized light in the x and y directions [61], φ is the phase difference between these amplitudes.

The angle ε in figure 2.14 is the ratio between the normal components of the resulting elliptical polarized light[61]. It is called the Kerr ellipticity and is given by

$$\tan\varepsilon = \frac{|E_{\min}|}{|E_{\max}|} = \frac{|E_{0R} - E_{0L}|}{|E_{0R} + E_{0L}|} \qquad 2.13,$$

where E_{0R} and E_{0L} are the basis states of the right-circularly polarized light and left-circularly polarized light, respectively. MOKE is often represented by the complex Kerr angle, θ_K, given by equation 2.14.

$$\theta_K = \varphi + i\varepsilon \qquad 2.14$$

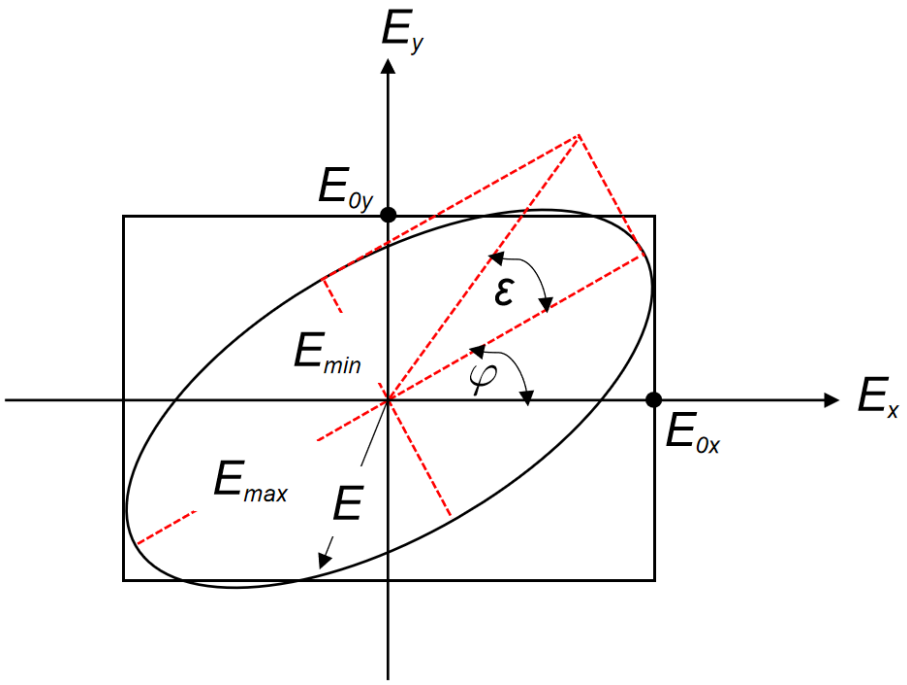

Figure 2.14: Electric field vector after a linearly polarized light impinges on a magnetic surface and experiences the Kerr effect. The angle φ is called the Kerr rotation and the angle ε is called the Kerr ellipticity. The figure is adapted from the Ref.[61].

2.5.4 Physical origin

There are two physical origins to explain the MOKE, i.e., semi-classical way and quantum theory.

The semi-classical explanation of the MOKE is as follows. Linear polarization can be separated into the equal superposition of phase and amplitude-coherent left and right circular polarization (LCP and RCP, respectively). When the electric field of LCP (RCP) propagates through a medium, the electrons will be excited, resulting in them to orbit in left (right) circular orbits. With a magnetic field in the medium, the electrons will feel different Lorentz forces, either away from or towards, the center of the orbit and the radius of the orbit will either increase or decrease. However, if the magnetic field is removed, the orbits will have the same radius, and linear polarization will be unchanged. Thus, when a material is excited by a light source, the superposition of LCP and RCP is different in comparison to the incident light. The linear polarization state will be rotated, and the different absorption rates between LCP and RCP will change the ellipticity.

However, this classical explanation is qualitatively correct. To quantify magneto-optic effects in ferromagnets, an effective field of the same order as the Weiss field is required[112]. When light travels through a dielectric material, it may experience different

refractive indexes depending on the direction of propagation. For material with optically isotropic properties, the permittivity tensor can be described as:

$$\varepsilon(\omega) = \begin{pmatrix} \varepsilon_{xx} & 0 & 0 \\ 0 & \varepsilon_{\mathrm{xx}} & 0 \\ 0 & 0 & \varepsilon_{\mathrm{xx}} \end{pmatrix} \qquad 2.15.$$

If the material is optically anisotropic, the permittivity tensor with non-zero off-diagonal terms will be shown as equation 2.19[113]:

$$\varepsilon(\omega) = \begin{pmatrix} \varepsilon_{xx} & \varepsilon_{xy} & -\varepsilon_{xz} \\ -\varepsilon_{xy} & \varepsilon_{yy} & \varepsilon_{yz} \\ \varepsilon_{xz} & -\varepsilon_{yz} & \varepsilon_{zz} \end{pmatrix} \qquad 2.16.$$

The magneto-optic effects can also be well explained by quantum theory. Linear magneto-optic effects are generated by the interaction of photons with electron spins via the spin-orbit interaction[113,114]. This statement can be proved by analyzing the Hamiltonian function for isolated one-electron and the magneto-optic effects, and the orbital motion of an electron in an electrostatic field[112].

2.5.5 Geometries of Kerr effect

There are three different geometries of MOKE, i.e., longitudinal MOKE, transverse MOKE, and polar MOKE, where their differences are relative to the plane of light incidence, as shown in figure 2.15.

For longitudinal geometry, the direction of the sample's magnetization is parallel to the plane of incidence light. And the transverse MOKE occurs when the direction of magnetization is perpendicular to the plane of light incidence. In polar MOKE, the linearly polarized light induces the electrons to oscillate parallel to its plane of polarization, which in this case it is the plane of electric field *E*. In this thesis, we use the polar MOKE configuration to design the home-made setup.

From figure 2.16, R_N is the regularly reflected light where it is polarized in the same plane as the incident light. The Lorentz force induces a small vibration in the direction perpendicular to the primary motion and the magnetization direction. This secondary motion is proportional to the Lorentz movement, generating the Kerr amplitude R_K for reflection. Therefore, the difference in angle between R_N and R_K results in the magnetization-dependent polarization rotation.

2.5.6 Measurement theory

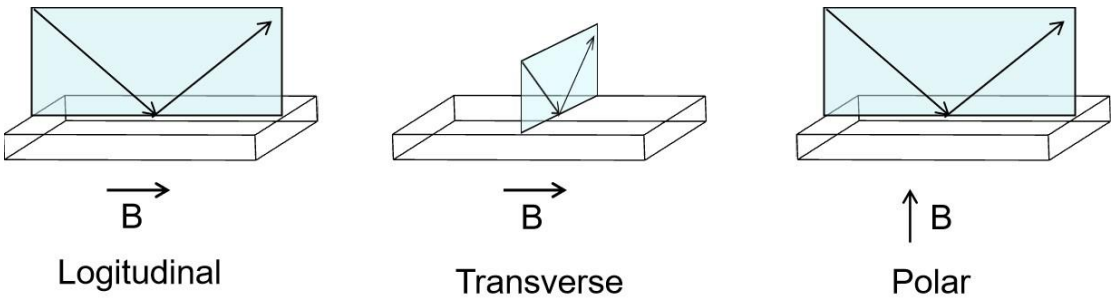

Figure 2.15: The longitudinal, transverse, and the polar magneto-optical Kerr effect (MOKE) measurement geometries are defined in terms of the relative orientation of the magnetic field **B** and the plane of incidence light. The figure is adapted from the Ref.[115].

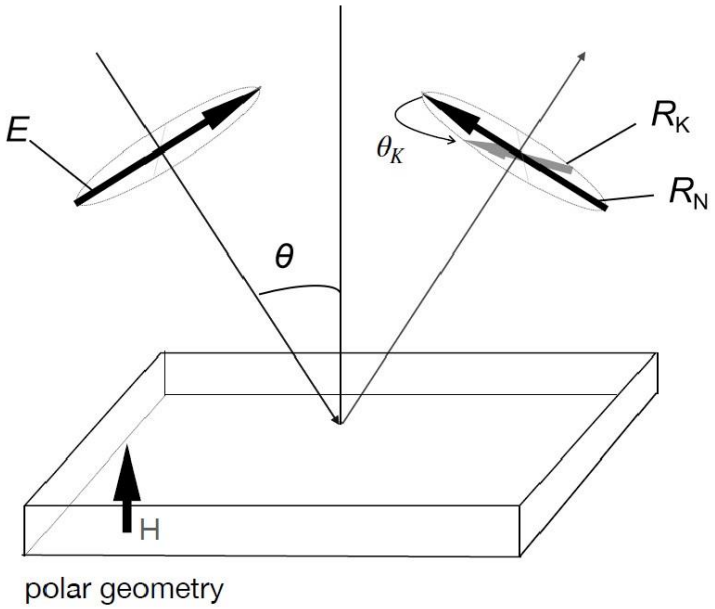

Figure 2.16: Diagram of the polar MOKE showing the magnetization direction and the Lorentz movement direction, which gives the Kerr effect in reflection. The figure is adapted from the Ref. [110].

The MOKE setup in our lab, shown in figure 2.17, was built by Simon Schäfer and Rolf B. Versteeg. After that, Jörg Schöpf updated it which enable us to simultaneously measure the Kerr rotation and Hall effect resistance. The measurement theory for the system was also presented in their master or Ph.D. thesis[116,117].

2.5.6.1 Intensity modulation

The setup response is calculated in the Jones matrix formalism. After the monochromator, the light passes a polarizer, which vertically polarizes the incident light:

$$\begin{pmatrix} 0 \\ 1 \end{pmatrix} \qquad 2.17.$$

The linearly polarized light is reflected from a sample represented by the reflection matrix:

$$\tilde{\rho}_{\text{circ}} = \begin{pmatrix} \tilde{\rho}_{+} & 0 \\ 0 & \tilde{\rho}_{-} \end{pmatrix} \qquad 2.18$$

given in circular basis.

The complex circular reflection coefficients are:

$$\tilde{\rho}_{\pm} = r_{\pm} e^{i\phi_{\pm}} \qquad 2.19,$$

where $r_{\pm}$ is the amplitude and $\varphi_{\pm}$ is the phase. When linearly polarized light reflects from the sample, the polarization variable is:

$$\zeta_{\text{m}} = \frac{\tilde{\rho}_{+}}{\tilde{\rho}_{-}} = \frac{r_{+}}{r_{-}} e^{i(\varphi_{+} - \varphi_{-})} \qquad 2.20.$$

The polarization rotation and ellipticity ratio are in this case:

$$\theta_{\text{k}} = \frac{1}{2}(\varphi_{+} - \varphi_{-}) \qquad \varepsilon_{\text{m}} = \frac{r_{-} - r_{+}}{r_{+} + r_{-}} \qquad 2.21.$$

In Cartesian coordinates, the sample reflection matrix is:

$$\tilde{\rho}_{\text{lin}} = \vec{F}^{-1} \cdot \tilde{\rho}_{\text{circ}} \cdot \vec{F} = \frac{1}{2} \begin{pmatrix} 1 & 1 \\ -i & i \end{pmatrix} \begin{pmatrix} \tilde{\rho}_{+} & 0 \\ 0 & \tilde{\rho}_{-} \end{pmatrix} \begin{pmatrix} 1 & i \\ 1 & -i \end{pmatrix} \qquad 2.22.$$

The PEM is a phase retarder, with the addition that the amount of retardation is now a periodic function in time:

$$O = \begin{pmatrix} e^{i\frac{\delta}{2}} & 0 \\ 0 & e^{-i\frac{\delta}{2}} \end{pmatrix}, \quad \delta(t) = \delta_0 \sin \omega t \qquad 2.23.$$

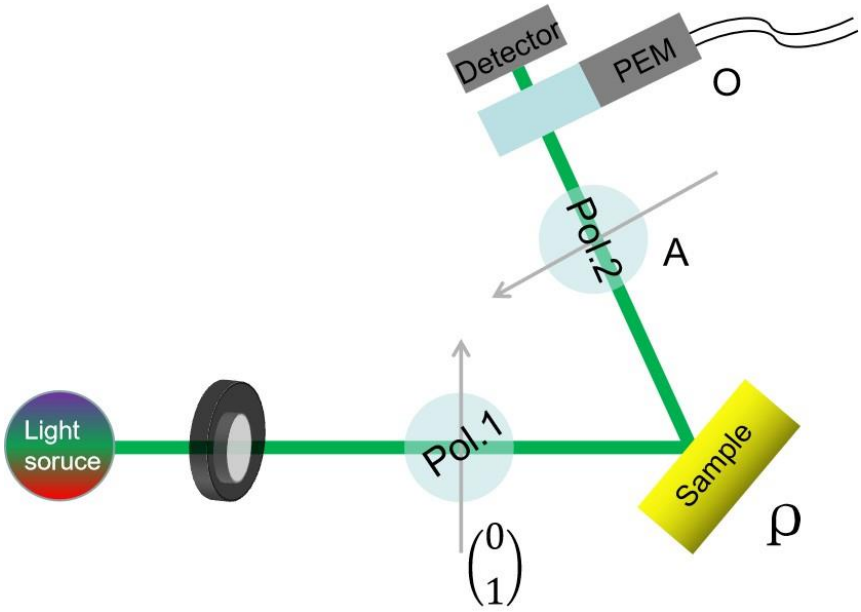

Figure 2.17: Schematic of the polarizing elements in the setup. Monochromatic light is polarized in the y-direction by polarizer one, reflected by the sample, modulated by the PEM, passes polarizer two and is collected by the detector. The symbols of the Jones matrices are attached. The figure is adapted from Ref. [118].

The second polarizer (the analyzer) is set to an angle of 135° (or 45°). Other configurations are possible, but will yield a worse signal-to-noise ratio in most experiments[119]. Thus, our general expression is simplified as follows:

$$A\left(135^{\circ}\right)=\begin{pmatrix}\cos^2\frac{3\pi}{4} & \cos\frac{3\pi}{4}\sin\frac{3\pi}{4}\\ \sin\frac{3\pi}{4}\cos\frac{3\pi}{4} & \sin^2\frac{3\pi}{4}\end{pmatrix}=\begin{pmatrix}\frac{1}{2} & -\frac{1}{2}\\ -\frac{1}{2} & \frac{1}{2}\end{pmatrix} \qquad 2.24.$$

Combining all the elements, the full Jones matrix representation of the beam path is:

$$\begin{aligned}\mathrm{E}_{\mathrm{out}} &= A\cdot O\cdot F^{-1}\cdot\rho_{\mathrm{circ}}\cdot F\begin{pmatrix}0\\1\end{pmatrix}\\ &=\frac{1}{2}\cdot\begin{pmatrix}\frac{1}{2} & -\frac{1}{2}\\ -\frac{1}{2} & \frac{1}{2}\end{pmatrix}\begin{pmatrix}e^{i\frac{\delta}{2}} & 0\\ 0 & e^{-i\frac{\delta}{2}}\end{pmatrix}\begin{pmatrix}1 & 1\\ -i & i\end{pmatrix}\begin{pmatrix}\tilde{\rho}_+ & 0\\ 0 & \tilde{\rho}_-\end{pmatrix}\begin{pmatrix}1 & i\\ 1 & -i\end{pmatrix}\begin{pmatrix}0\\1\end{pmatrix} \qquad 2.25.\\ &=\frac{e^{-i\frac{\delta}{2}}}{4}\cdot\begin{pmatrix}ie^{i\delta}\left(\tilde{\rho}_+-\tilde{\rho}_-\right)-\left(\tilde{\rho}_++\tilde{\rho}_-\right)\\ \left(\tilde{\rho}_++\tilde{\rho}_-\right)-ie^{i\delta}\left(\tilde{\rho}_+-\tilde{\rho}_-\right)\end{pmatrix}\\ &=\frac{e^{-i\frac{\delta}{2}}}{4}\cdot\left(ie^{i\delta}\left(\tilde{\rho}_+-\tilde{\rho}_-\right)-\left(\tilde{\rho}_++\tilde{\rho}_-\right)\right)\cdot\begin{pmatrix}1\\-1\end{pmatrix}\end{aligned}$$

The signal intensity arriving at the detector is the absolute square of this value:

$$I_{\text{out}} = \left|E_{\text{out}}\right|^2 = \frac{1}{8}\cdot\left|ie^{i\delta}\left(\tilde{\rho}_+ - \tilde{\rho}_-\right) - \left(\tilde{\rho}_+ + \tilde{\rho}_-\right)\right|^2 \qquad 2.26.$$

We note here that $\tilde{\rho}_+$ and $\tilde{\rho}_-$ are complex valued, and of the form $\tilde{\rho}_\pm = r_\pm e^{i\theta_\pm}$. We also define $\Delta\theta = \frac{1}{2}\left(\theta_+ - \theta_-\right)$ after a lengthy calculation, we receive:

$$I = \frac{1}{4}\left[r_+^2 + r_-^2 + \left(r_+^2 - r_-^2\right)\sin\delta + 2r_+ r_- \cos\delta \sin\Delta\theta\right] \qquad 2.27.$$

From equation 2.21, we estimate the difference in reflectivity to be small: $|r_+ - r_-| \ll r_+ + r_-$. This allows us to use the following approximations:

$$\frac{r_+^2 - r_-^2}{r_+^2 + r_-^2} \approx 2\,\frac{r_+ - r_-}{r_+ + r_-} = 2\,\varepsilon_m \qquad 2.28$$

$$\frac{r_+ r_-}{r_+^2 + r_-^2} \approx \frac{1}{2} \qquad 2.29.$$

Additionally, we use the shorthand

$$I = \frac{1}{2}R\left[1 + 2\varepsilon_m \sin\delta + \cos\delta \sin\left(-2\theta_k\right)\right] \qquad 2.30.$$

The above intensity expression contains the terms of interest: the rotation θ_K, and ellipticity ratio ε. The PEM modulates the intensity by $\delta(t) = \delta_0 \sin(\omega t)$. The sine and cosine function terms are expanded in Bessel function terms J as[120]:

$$\cos\left(\delta_0 \sin(\omega t)\right) = J_0\left(\delta_0\right) + 2\sum_{n=1}^{\infty} J_{2n}\left(\delta_0\right)\cos(2n\omega t)$$
$$= J_0\left(\delta_0\right) + 2J_2\left(\delta_0\right)\cos(2\omega t) + \text{higher order even } \omega \text{ terms} \qquad 2.31.$$

$$\sin\left(\delta_0 \sin(\omega t)\right) = 2\sum_{n=0}^{\infty} J_{2n+1}\left(\delta_0\right)\sin((2n+1)\omega t)$$
$$= 2J_1\left(\delta_0\right)\sin(\omega t) + \text{higher order uneven } \omega \text{ terms}$$

Here, the orders higher than 2ω are ignored. The modulated intensity arriving at the detector thus is:

$$I = I(0) + I(\omega) + I(2\omega) + \text{higher order } \omega \text{ terms} \qquad 2.32$$

with:

$$I(0) = \frac{R}{2}\left(1 + 2J_0\left(\delta_0\right)\sin\left(-2\theta_k\right)\right) \qquad 2.33$$

$$I(\omega) = \frac{R}{2}\left(4J_1\left(\delta_0\right)\varepsilon_m\right) \qquad 2.34$$

$$I(2\omega) = \frac{R}{2}\left(2J_2\left(\delta_0\right)\sin\left(-2\theta_k\right)\right) \qquad 2.35.$$

The component without temporally modulated intensity is $I(0)$. The $I(0)$ intensity is determined by mechanically chopping the incident light at a frequency $f_{\text{chopper}} << f_{\text{PEM}}$ depending on the retardation amplitude δ_0 through the zero'th order Bessel functions $J_0(\delta_0)$. Similarly, $J_1(\delta_0)$, and $J_2(\delta_0)$ are determined by the first and second-order Bessel functions. Detectors and lock-in amplifiers show different sensitivities to DC values and the modulated ω and 2ω signals which are in the kHz range. This dependency is captured with effective constants A and B for the different frequency components.

In the measurement, we will get signals from lock-in amplifiers I_{DC}, $I_{\text{f,}}$ and $I_{2\text{f}}$. Here the I_{f} and $I_{2\text{f}}$ can be easily derived from $\omega=2\pi f$, equations 2.34, and 2.35. To extract the Kerr rotation and ellipticity, we will divide the PEM-modulated signals by the DC signal:

$$\frac{I_f}{I_{DC}} = A \cdot \frac{4J_1\left(\delta_0\right)\varepsilon_m}{1 + 2J_0\left(\delta_0\right)\sin\left(-2\theta_k\right)} \approx 4AJ_1\left(\delta_0\right)\theta_k = \mathrm{C}_1 \cdot \varepsilon_m \qquad 2.36$$

$$\frac{I_{2f}}{I_{DC}} = B \cdot \frac{2J_2\left(\delta_0\right)\sin\left(-2\theta_k\right)}{1 + 2J_0\left(\delta_0\right)\sin\left(-2\theta_k\right)} \approx -4BJ_2\left(\delta_0\right)\theta_k = \mathrm{C}_2 \cdot \theta_k \qquad 2.37.$$

2.5.7 Calibration of the Kerr rotation

The calibration of the Kerr rotation is easy to achieve by rotating a positive and negative incident angle ($\pm\varphi$) of polarizer one, which polarizes the incident light. Then we can quantify the signal as follows:

$$\left.\frac{I_{2f}}{I_{DC}}(\lambda)\right|_{\pm\varphi} = C_2(\lambda)(\pm\varphi) \qquad 2.38.$$

Then we can determine the calibration constant $C_2(\lambda)$ by:

$$C_2(\lambda) = \frac{\left.\frac{I_{2f}}{I_{DC}}(\lambda)\right|_{\varphi} - \left.\frac{I_{2f}}{I_{DC}}(\lambda)\right|_{-\varphi}}{2\varphi} \qquad 2.39.$$

Combining the equation 2.38 and 2.39, the measured Kerr rotation angle can be rewritten as:

$$\theta(\lambda) = \frac{\frac{I_{2f}}{I_{DC}}(\lambda)}{C_2(\lambda)} \qquad 2.40.$$

For a single wavelength measurement (temperature or field sweep), the ratio I_{2f}/I_{DC} is measured for known incident positive and negative incident polarization rotations (normally, ±1°, ±2°, ±3°). The measured ratios are then fitted with the function 2.39, as shown in figure 2.18.

2.5.8 The Kerr spectroscopy of $SrRuO_3$

The magneto-optical studies carried out on $SrRuO_3$ single crystal, and thin film $SrRuO_3$ have shown large magneto-optical effects[121,122]. The Kerr spectroscopy of $SrRuO_3$ can indicate the relation between electron structure and MOKE spectrum.

For example, a Kerr spectrum of a [101] oriented single crystal of $SrRuO_3$ was taken at T = 15 K by Polar MOKE measurement, as shown in figure 2.19. The grey curve, which shows a peak position at 1.75 eV and 2.85 eV, is the theoretical Kerr spectrum from the simulation. The red dots curve shows the experimental peaks observed at ~1.65 eV and ~2.65 eV[117], which is in good quantitative agreement with the theoretical peaks. The peak at lower energy comes from the plasma resonance[123] in the diagonal optical conductivity σ_{xx}. The higher one is affected by strong hybridization of O(2*p*) and Ru(4*d*) states which induce the O(2*p*)→Ru(4*d*) interband transition[121,122].

According to the above introduction of theoretical and experimental Kerr spectrum, one can choose a suitable wavelength responding to the key energy to maximize the measured Kerr rotation angle. Actually, the $I(0)$ is a constant depending on the source intensity, which means the intensity of the light measured by the detector is wavelength-dependent. Besides, defects or impurities for the real samples exist in different samples.

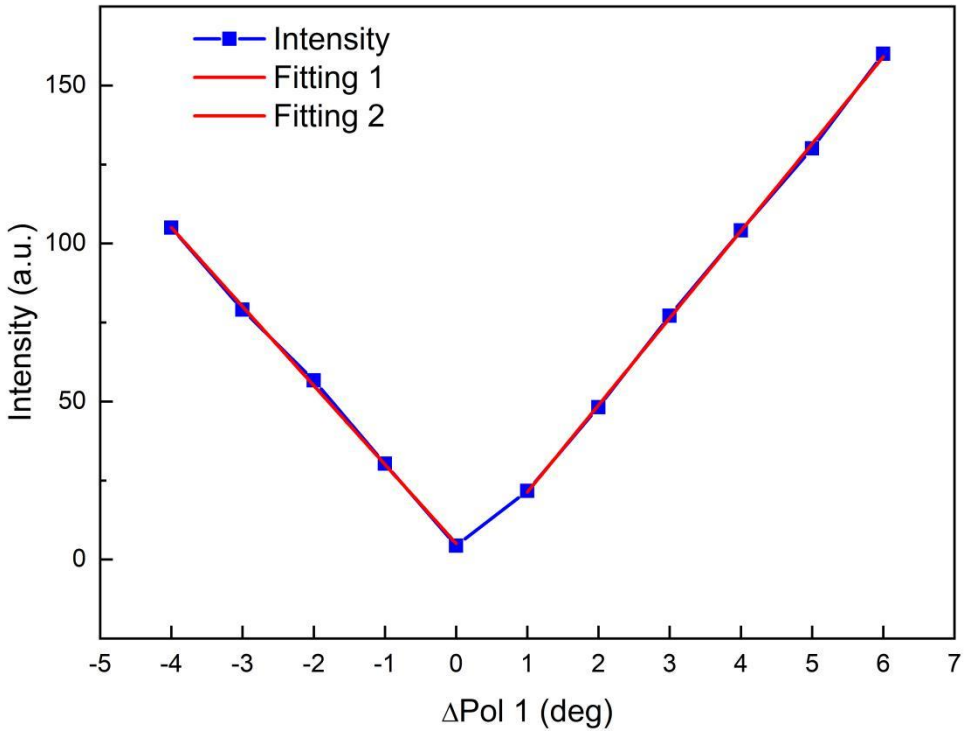

Figure 2.18: Calibration and fitting data with the small rotation angle of polarizer for a $LaNiO_3/SrRuO_3$ heterostructure.

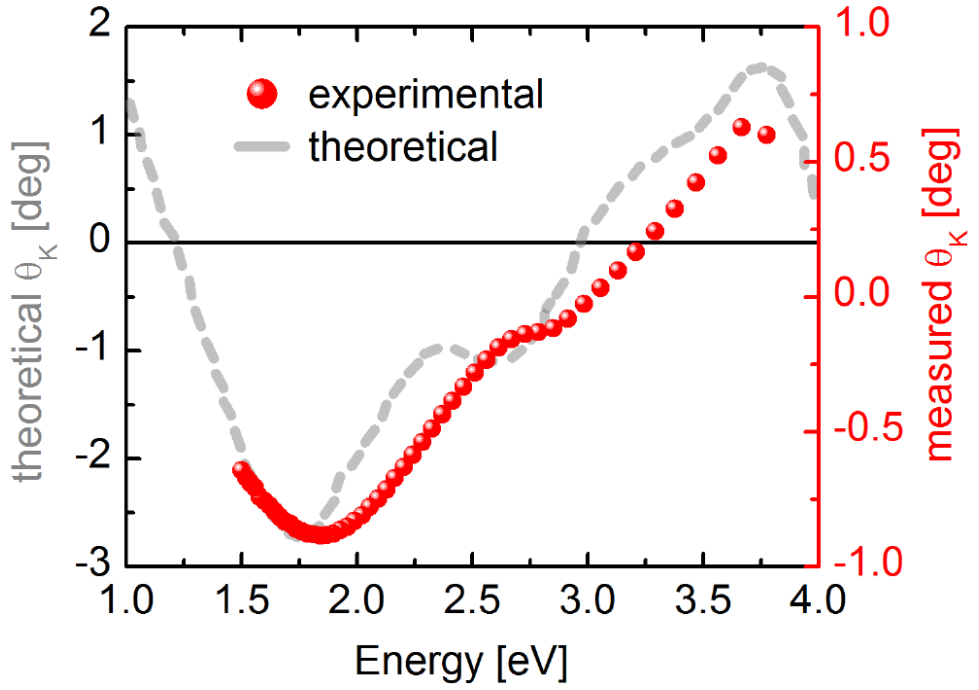

Figure 2.19: (a) The gray dashed line gives the theoretical $\theta_K(E)$ spectrum. The red spheres give the measured $\theta_K(E)$ at μ0Ha = +0.5 T at T = 15 K. Peaks are observed at 1.75 eV and 2.85 eV. The figure is taken from Ref.[117].

The Kerr spectrum tends to be different between them. Then a suitable wavelength is required to maximize the intensity for measurement.

2.6 References

[1] J. Xia, W. Siemons, G. Koster, M. R. Beasley, and A. Kapitulnik, Phys Rev B **79** (14), 140407 (2009).

[2] M. Kim and B. I. Min, Phys Rev B **91** (20) (2015).

[3] Z. Sefrioui, D. Arias, M. A. Navacerrada, M. Varela, G. Loos, M. Lucía, J. Santamaría, F. Sánchez-Quesada, and M. A. López de la Torre, Applied Physics Letters **73** (23), 3375 (1998).

[4] J. M. Rondinelli, N. M. Caffrey, S. Sanvito, and N. A. Spaldin, Phys Rev B **78** (15), 155107 (2008).

[5] C. U. Jung, H. Yamada, M. Kawasaki, and Y. Tokura, Applied Physics Letters **84** (14), 2590 (2004).

[6] Z. Zeng, J. Feng, X. Zheng, C. Wang, J.W. Liu, Z. X. Lu, F.-X. Jiang, X.-H. Xu, Z. M. Wang, and R.-W. Li, Applied Physics Letters **116** (14), 142401 (2020).

[7] I. Bakonyi, E. Simon, B. G. Tóth, L. Péter, and L. F. Kiss, Phys Rev B **79** (17), 174421 (2009).

[8] F. Bern, M. Ziese, A. Setzer, E. Pippel, D. Hesse, and I. Vrejoiu, Journal of Physics: Condensed Matter **25** (49), 496003 (2013).

[9] Y. Shokr, Ph.D. thesis, Freien Universität Berlin (2016).

[10] Y. Ohuchi, J. Matsuno, N.Ogawa, Y. Kozuka, M. Uchida, Y. Tokura, and M. Kawasaki, Nature Communications **9** (1), 213 (2018).

[11] D. J. Groenendijk, C. Autieri, T. C. van Thiel, W. Brzezicki, J. R. Hortensius, D. Afanasiev, N. Gauquelin, P. Barone, K. H. W. van den Bos, S. van Aert, J. Verbeeck, A. Filippetti, S. Picozzi, M. Cuoco, and A. D. Caviglia, Physical Review Research **2** (2), 023404 (2020).

[12] M. Ziese, F. Bern, P. D. Esquinazi, and I. Lindfors-Vrejoiu, Physica status solidi (b) **257** (7), 1900628 (2020).

[13] I. Lindfors-Vrejoiu and M. Ziese, physica status solidi (b) **254** (5), 1600556 (2017).

[14] Q. Qin, W. Song, S. He, P. Yang, and J. Chen, Journal of Physics D: Applied Physics **50** (21), 215002 (2017).

[15] L. Wysocki, R. Mirzaaghayev, M. Ziese, L. Yang, J. Schöpf, R. B. Versteeg, A. Bliesener, J. Engelmayer, A. Kovács, L. Jin, F. Gunkel, R. Dittmann, P. H. M. van Loosdrecht, and I. Lindfors-Vrejoiu, Applied Physics Letters **113** (19), 192402 (2018).

[16] L. Yang, L. Jin, L. Wysocki, J. Schöpf, D. Jansen, B. Das, L. Kornblum, P.H. M. van Loosdrecht, and I. Lindfors-Vrejoiu, Phys Rev B **104** (6), 064444 (2021).

[17] C. W. Jones, P. D. Battle, P. Lightfoot, and W. T. A. Harrison, Acta Crystallographica Section C **45** (3), 365 (1989).

[18] G. Koster, L. Klein, W. Siemons, G. Rijnders, J. Steven Dodge, C.-B. Eom, D. H. A. Blank, and M. R. Beasley, Reviews of Modern Physics **84** (1), 253

(2012).
[19] J. Choi, C. B. Eom, G. Rijnders, H. Rogalla, and D. H. A. Blank, Applied Physics Letters **79** (10), 1447 (2001).
[20] D. Kan and Y. Shimakawa, Crystal Growth & Design **11** (12), 5483 (2011).
[21] D. Kan, R. Aso, H. Kurata, and Y. Shimakawa, Advanced Functional Materials **23** (9), 1129 (2013).
[22] W. Lu, W. Song, P. Yang, J. Ding, G. Moog Chow, and J. Chen, Scientific Reports **5** (1), 10245 (2015).
[23] Q. Gan, R. A. Rao, C. B. Eom, L. Wu, and F. Tsui, Journal of Applied Physics **85** (8), 5297 (1999).
[24] K. J. Choi, S. Hyub Baek, H. W. Jang, L. J. Belenky, M. Lyubchenko, and C.-B. Eom, Advanced Materials **22** (6), 759 (2010).
[25] M. S. Laad and E. Müller-Hartmann, Physical Review Letters **87** (24), 246402 (2001).
[26] K. Yoshimura, T. Imai, T. Kiyama, K. R. Thurber, A. W. Hunt, and K. Kosuge, Physical Review Letters **83** (21), 4397 (1999).
[27] Q. Gan, R. A. Rao, C. B. Eom, J. L. Garrett, and Mark Lee, Applied Physics Letters **72** (8), 978 (1998).
[28] G. Cao, S. McCall, M. Shepard, J. E. Crow, and R. P. Guertin, Phys Rev B **56** (1), 321 (1997).
[29] Wikipedia contributors, Magnetic anisotropy, https://en.wikipedia.org/w/index.php?title=Magnetic_anisotropy&oldid=1067920859 (last visited May 10, 2022). Wikipedia.
[30] C. Tannous and J. Gieraltowski, European Journal of Physics **29** (3), 475 (2008).
[31] D. Sander, Journal of Physics: Condensed Matter **16** (20), R603 (2004).
[32] A. Kanbayasi, Journal of the Physical Society of Japan **41** (6), 1879 (1976).
[33] L. Wu, F. Wen, Y. Fu, J. H. Wilson, X. Liu, Y. Zhang, D. M. Vasiukov, M. S. Kareev, J. H. Pixley, and J. Chakhalian, Phys Rev B **102** (22), 220406 (2020).
[34] A. Kanbayasi, Journal of the Physical Society of Japan **44** (1), 108 (1978).
[35] L. Klein, J. S. Dodge, C. H. Ahn, J. W. Reiner, L. Mieville, T. H. Geballe, M. R. Beasley, and A. Kapitulnik, Journal of Physics: Condensed Matter **8** (48), 10111 (1996).
[36] Y. Kats, I. Genish, L. Klein, J. W. Reiner, and M. R. Beasley, Physical Review B **71** (10), 100403 (2005).
[37] L. D. Landau, J. S. Bell, M. J. Kearsley, L. P. Pitaevskii, E .M. Lifshitz, and J. B. Sykes, *Electrodynamics of continuous media*. (elsevier, 2013).
[38] K. Terai, T. Ohnishi, M. Lippmaa, H. Koinuma, and M. Kawasaki, Japanese Journal of Applied Physics **43** (No. 2A), L227 (2004).
[39] M. Matczak, B. Szymański, M. Urbaniak, M. Nowicki, H. Głowiński, P. Kuświk, M. Schmidt, J. Aleksiejew, J. Dubowik, and F. Stobiecki, Journal of Applied Physics **114** (9), 093911 (2013).
[40] M. A. Ruderman and C. Kittel, Physical Review **96** (1), 99 (1954).

41 T. Kasuya, Progress of Theoretical Physics, **16**, 45 (1956).

42 Kei Yosida, Physical Review **106** (5), 893 (1957).

43 M. D. Stiles, Journal of Magnetism and Magnetic Materials **200** (1), 322 (1999).

44 W. Kuch, L. I. Chelaru, F. Offi, J. Wang, M. Kotsugi, and J. Kirschner, Nature Materials **5** (2), 128 (2006).

45 J. Wu, J. Choi, A. Scholl, A. Doran, E. Arenholz, Y. Z. Wu, C. Won, Chanyong Hwang, and Z. Q. Qiu, Phys Rev B **80** (1), 012409 (2009).

46 B. Zhang, C.-B. Wu, and W. Kuch, Journal of Applied Physics **115** (23), 233915 (2014).

47 J. Moritz, F. Garcia, J. C. Toussaint, B. Dieny, and J. P. Nozières, Europhysics Letters (EPL) **65** (1), 123 (2004).

48 W. Kuch, L. I. Chelaru, K. Fukumoto, F. Porrati, F. Offi, M. Kotsugi, and J. Kirschner, Phys Rev B **67** (21), 214403 (2003).

49 V. Baltz, B. Rodmacq, A. Bollero, J. Ferré, S. Landis, and B. Dieny, Applied Physics Letters **94** (5), 052503 (2009).

50 J. F. Bobo, H. Kikuchi, O. Redon, E. Snoeck, M. Piecuch, and R. L. White, Phys Rev B **60** (6), 4131 (1999).

51 F. Stobiecki, B. Szymanski, M. Urbaniak, T. Lucinski, J. Dubowik, M. Kopcewicz, J. Jagielski, and Y. P. Lee, Journal of the Korean Physical Society **45** (1), 1 (2004).

52 P. Bruno, Phys Rev B **52** (1), 411 (1995).

53 P. Bruno and C. Chappert, Physical Review Letters **67** (12), 1602 (1991).

54 J. C. Slonczewski, Journal of Magnetism and Magnetic Materials **150** (1), 13 (1995).

55 D. T. Pierce, J. Unguris, R. J. Celotta, and M. D. Stiles, Journal of Magnetism and Magnetic Materials **200** (1), 290 (1999).

56 A. Berger and H. Hopster, Physical Review Letters **73** (1), 193 (1994).

57 H. Hopster, Physical Review Letters **83** (6), 1227 (1999).

58 V. M. Uzdin, C. Demangeat, Journal of Magnetism and Magnetic Materials, **165**, 458 (1997).

59 M. Onoda and N. Nagaosa, Journal of the Physical Society of Japan **71** (1), 19 (2002).

60 N. A. Sinitsyn, Journal of Physics: Condensed Matter **20** (2), 023201 (2007).

61 J. Stöhr, H.C.S. Joachim Stšhr, and H.C. Siegmann, *Magnetism: From Fundamentals to Nanoscale Dynamics*. (Springer, 2006).

62 G. S. Leadstone, Physics Education **14** (6), 374 (1979).

63 E. M. Pugh and N. Rostoker, Reviews of Modern Physics **25** (1), 151 (1953).

64 E. M. Pugh, Physical Review **36** (9), 1503 (1930).

65 E. M. Pugh and T. W. Lippert, Physical Review **42** (5), 709 (1932).

66 C. Liu, S. Zhang, X. Qi, arXiv: 1508.07106, Mesoscale and Nanoscale Physics (2015).

67 R. Karplus and J. M. Luttinger, Physical Review **95** (5), 1154 (1954).

[68] N. Nagaosa, J. Sinova, S. Onoda, A. H. MacDonald, and N. P. Ong, Reviews of Modern Physics **82** (2), 1539 (2010).

[69] J. Smit, Physica **24** (1), 39 (1958).

[70] L. Berger, Phys Rev B **5** (5), 1862 (1972).

[71] H.-Y. Yang, B. Singh, B. Lu, C.-Y. Huang, F. Bahrami, W.-C. Chiu, D. Graf, S.-M. Huang, B. Wang, H. Lin, D. Torchinsky, A. Bansil, and F. Tafti, Applied Physics Letters Material **8** (1), 011111 (2020).

[72] L. Klein, J. R. Reiner, T. H. Geballe, M. R. Beasley, and A. Kapitulnik, Phys Rev B **61** (12), R7842 (2000).

[73] R. Mathieu, A. Asamitsu, H. Yamada, K. S. Takahashi, M. Kawasaki, Z. Fang, N. Nagaosa, and Y. Tokura, Physical Review Letters **93** (1), 016602 (2004).

[74] G. Bergmann, Eur. Phys. J. B **54** (1), 19 (2006).

[75] N. Nagaosa, Journal of the Physical Society of Japan **75** (4), 042001 (2006).

[76] J. M. Phillips, MRS Bulletin **20** (4), 35 (1995).

[77] M. D. Biegalski, L. Qiao, Y. Gu, A. Mehta, Q. He, Y.Takamura, A. Borisevich, and L.Qing Chen, Applied Physics Letters **106** (16), 162904 (2015).

[78] A. F. Marshall, L. Klein, J. S. Dodge, C. H. Ahn, J. W. Reiner, L. Mieville, L. Antagonazza, A. Kapitulnik, T. H. Geballe, and M. R. Beasley, Journal of Applied Physics **85** (8), 4131 (1999).

[79] J. C. Jiang, X. Q. Pan, and C. L. Chen, Applied Physics Letters **72** (8), 909 (1998).

[80] G. Rijnders, D. H. A. Blank, J. Choi, and C.-B. Eom, Applied Physics Letters **84** (4), 505 (2004).

[81] M. Kawasaki, K.Takahashi, T. Maeda, R. Tsuchiya, M. Shinohara, O. Ishiyama, T. Yonezawa, M. Yoshimoto, and H. Koinuma, Science **266** (5190), 1540 (1994).

[82] X. Wan, A.M. Turner, A. Vishwanath, and S.Y. Savrasov, Phys Rev B **83** (20), 205101 (2011).

[83] T. Han, Y.n Wang, J.Yang, L. He, J. Xu, D. Liang, H. Han, M. Ge, C. Y. Xi, W. K. Zhu, C. Zhang, and Y. Zhang, Applied Physics Letters **109** (19), 192409 (2016).

[84] S.-W. Cheong and M. Mostovoy, Nature Materials **6** (1), 13 (2007).

[85] K.-Y. Yang, Y.-M. Lu, and Y. Ran, Phys Rev B **84** (7), 075129 (2011).

[86] H. L. Stormer, Reviews of Modern Physics **71** (4), 875 (1999).

[87] J.-M. Carter, V. V. Shankar, M. A. Zeb, and H.-Y. Kee, Phys Rev B **85** (11), 115105 (2012).

[88] L. Zhang, B. Pang, Y. B. Chen, and Y. Chen, Critical Reviews in Solid State and Materials Sciences **43** (5), 367 (2017).

[89] J. Matsuno, N. Ogawa, K. Yasuda, F. Kagawa, W. Koshibae, N. Nagaosa, Y. Tokura, and M. Kawasaki, Science Advances **2** (7), e1600304.

[90] P. E. R. Blanchard, E. Reynolds, B. J. Kennedy, J. A. Kimpton, M. Avdeev, and A. A. Belik, Phys Rev B **89** (21), 214106 (2014).

[91] J. M. Longo, J. A. Kafalas, and R. J. Arnott, Journal of Solid State Chemistry **3** (2), 174 (1971).

[92] J. G. Zhao, L. X. Yang, Y. Yu, F. Y. Li, R. C. Yu, Z. Fang, L. C. Chen, and C. Q. Jin, Journal of Applied Physics **103** (10), 103706 (2008).
[93] B. J. Kim, Hosub Jin, S. J. Moon, J. Y. Kim, B. G. Park, C. S. Leem, Jaejun Yu, T. W. Noh, C. Kim, S. J. Oh, J. H. Park, V. Durairaj, G. Cao, and E. Rotenberg, Physical Review Letters **101** (7), 076402 (2008).
[94] J. W. Kim, Y. Choi, Jungho Kim, J. F. Mitchell, G. Jackeli, M. Daghofer, J. van den Brink, G. Khaliullin, and B. J. Kim, Physical Review Letters **109** (3), 037204 (2012).
[95] S. J. Moon, H. Jin, K. W. Kim, W. S. Choi, Y. S. Lee, J. Yu, G. Cao, A. Sumi, H. Funakubo, C. Bernhard, and T. W. Noh, Physical Review Letters **101** (22), 226402 (2008).
[96] Y. F Nie, P. D C King, C. H Kim, M. Uchida, H. I Wei, B. D Faeth, J. P Ruf, J. P C Ruff, L. Xie, X. Pan, C. J Fennie, D. G Schlom, and K. M Shen, Physical Review Letters **114** (1), 016401 (2015).
[97] W. Wang, L. Li, J. Liu, B. Chen, Y. Ji, J0 Wang, G0 Cheng, Y. Lu, G. Rijnders, G. Koster, W. Wu, and Z. Liao, npj Quantum Materials **5** (1), 73 (2020).
[98] M. M. Kane, A. Vailionis, L. J. Riddiford, A. Mehta, A. T. N'Diaye, C. Klewe, P. Shafer, E. Arenholz, and Y. Suzuki, npj Quantum Materials **6** (1), 44 (2021).
[99] J. Son, P. Moetakef, J. M. LeBeau, D. Ouellette, L. Balents, S. J. Allen, and S. Stemmer, Applied Physics Letters **96** (6), 062114 (2010).
[100] E. J. Moon, B. A. Gray, M. Kareev, J. Liu, S. G. Altendorf, F. Strigari, L. H. Tjeng, J. W. Freeland, and J. Chakhalian, New Journal of Physics **13** (7), 073037 (2011).
[101] E. Sakai, M. Tamamitsu, K. Yoshimatsu, S. Okamoto, K. Horiba, M. Oshima, and H. Kumigashira, Phys Rev B **87** (7), 075132 (2013).
[102] J. Fowlie, M. Gibert, G. Tieri, A. Gloter, J. Íñiguez, A. Filippetti, S. Catalano, S.Gariglio, A.Schober, M.Guennou, J. Kreisel, O. Stéphan, and J.-M. Triscone, Advanced Materials **29** (18), 1605197 (2017).
[103] Y. Li, J. Zhou, and D. Wu, ACS Applied Materials & Interfaces **11** (3), 3565 (2019).
[104] K. Tsubouchi, I. Ohkubo, H. Kumigashira, Y. Matsumoto, T. Ohnishi, M. Lippmaa, H. Koinuma, and M. Oshima, Applied Physics Letters **92** (26), 262109 (2008).
[105] J. B. Torrance, P. Lacorre, A. I. Nazzal, E. J. Ansaldo, and C. Niedermayer, Physical review. B, Condensed matter **45** (14), 8209 (1992).
[106] J. L. García-Muñoz, J. Rodríguez-Carvajal, and P. Lacorre, Physical review. B, Condensed matter **50** (2), 978 (1994).
[107] A. Rüegg and G. A. Fiete, Phys Rev B **84** (20), 201103 (2011).
[108] L. Sun, T. Yu, Y.-F. Chen, J. Zhou, and N.-B. Ming, Journal of Materials Research **12** (4), 931 (1997).
[109] N. O. Urs, B. Mozooni, P. Mazalski, M. Kustov, P. Hayes, S. Deldar, E. Quandt, and J. McCord, AIP Advances **6** (5), 055605 (2016).
[110] A. Hubert and R. Schäfer, *Magnetic domains : the analysis of magnetic*

microstructures. (Berlin : Springer, 1998).
[111] H. E. Edens, Master's thesis, University of Amsterdam, (2002).
[112] P. N. Argyres, Physical Review **97** (2), 334 (1955).
[113] J. Zak, E. R. Moog, C. Liu, and S. D. Bader, Journal of Applied Physics **68** (8), 4203 (1990).
[114] P. S. Pershan, Journal of Applied Physics **38** (3), 1482 (1967).
[115] A. Arora, S. Ghosh, and V. Sugunakar, Review of Scientific Instruments **82** (12), 123903 (2011).
[116] J. Schöpf, Master thesis, Universität zu Köln (2019).
[117] R. B. Versteeg, Ph.D. thesis, Universität zu Köln (2019).
[118] S. Schäfer, Master thesis, Universität zu Köln (2015).
[119] S. Polisetty, J. Scheffler, S. Sahoo, Yi Wang, T. Mukherjee, X. He, and Ch Binek, Review of Scientific Instruments **79** (5), 055107 (2008).
[120] K. Sato, Japanese Journal of Applied Physics **20** (12), 2403 (1981).
[121] H. Ohta, E. Kulatov, J. S. Dodge, Yu Uspenskii, and S. Halilov, Journal of the Magnetics Society of Japan **22** (S_2_MORIS_97), S2_185 (1998).
[122] J. S. Dodge, E. Kulatov, L. Klein, C. H. Ahn, J. W. Reiner, L. Miéville, T. H. Geballe, M. R. Beasley, A. Kapitulnik, H. Ohta, Yu Uspenskii, and S. Halilov, Phys Rev B **60** (10), R6987 (1999).
[123] H. Feil and C. Haas, Physical Review Letters **58** (1), 65 (1987).

Chapter 3 Experimental methods

Contents

This chapter outlines the experimental techniques used to prepare and characterize magnetic heterostructures.

3.1 Film growth

3.1.1 Pulsed Laser Deposition

Pulsed Laser Deposition (PLD) is commonly used to make thin films of complex materials, such as strongly-correlated electronic materials[1,2], colossal magnetoresistance materials[3,4], ferroelectrics[5], high-temperature superconductors[6,7] and compound semiconductors[8].

PLD is a competitive technique for several reasons. Firstly, it enables the stoichiometric transfer of the target material to the film[9]. Secondly, it is easy to fabricate different thicknesses and multilayers films by controlling the growth time, the pulse repetition rate, and varying targets. Thirdly, the laser is outside the chamber, which can minimize any impurities caused by in-vacuum power components. The laser can serve many vacuum systems to save the laser cost. One can obtain atomic-scale oxide thin-films and heterostructures by PLD, which are high quality and comparable to samples prepared by molecular beam epitaxy (MBE)[10]. PLD combined reflection high-energy electron diffraction (RHEED) allows one to characterize the film growth in real-time[11-13].

The basic principles of PLD are sketched in figure 3.1: A pulsed laser beam is focused down to a high energy density onto a single or polycrystalline target, placed

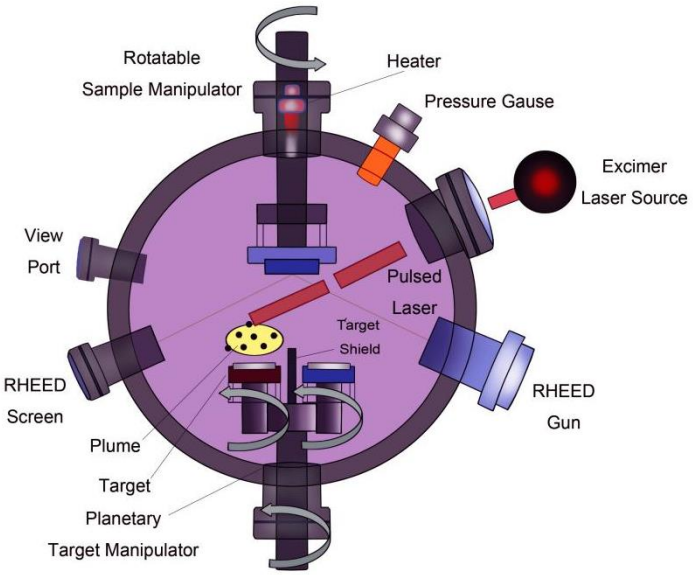

Figure 3.1: Principle of pulsed laser deposition (PLD): A laser is focused on a rotating target where it ablates material in the form of a plasma. A heated substrate is placed into the emerging plasma plume. On the substrate, the plasma condenses and a film grows.

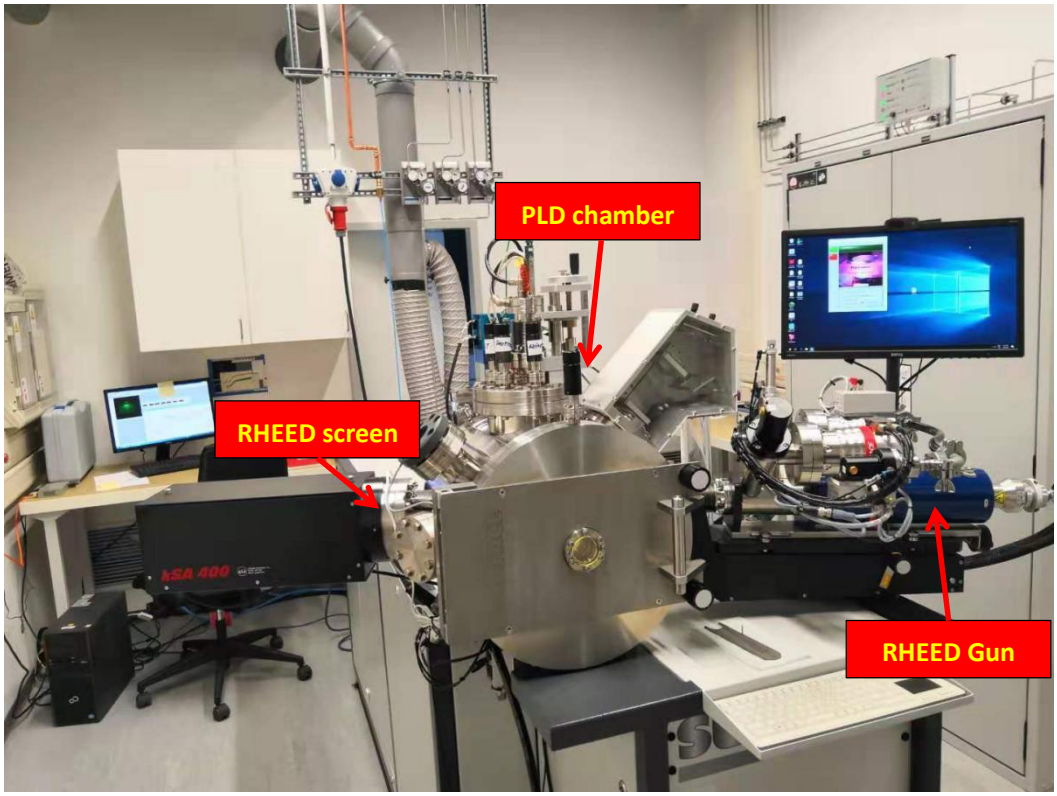

Figure 3.2: Photo of the PLD machine with which the samples were made.

in a vacuum chamber with a defined gas atmosphere. The laser-matter interaction leads to a rapid ablation of target material, which is ejected as a plasma plume, expanding in a flow perpendicular to the target surface. This plasma plume contains charged and neutral species of the target material. Repetition of laser shots leads to an accumulation of matter onto the substrate surface, resulting in forming a thin film.

In this work, the PLD fabricated the samples with the equipment shown in figure 3.2. The growth process can be conducted in different gas atmospheres. In my thesis, oxygen is used.

3.1.2 Reflection high-energy electron diffraction (RHEED)

Reflection high-energy electron diffraction (RHEED) is a common technique used to characterize the surface of crystalline materials. This *in situ* system has two advantages. First, the *in situ* measurements are non-destructive and are free from sample degradation due to adsorbates from the ambient atmosphere. Second, simultaneous measurements performed by the RHEED allow the entire thin-film growth process to be observed and characterized. The thickness of the grown layers. may be inferred if the layer growth model allows, and the crystalline structure or possible surface reconstruction can be observed.

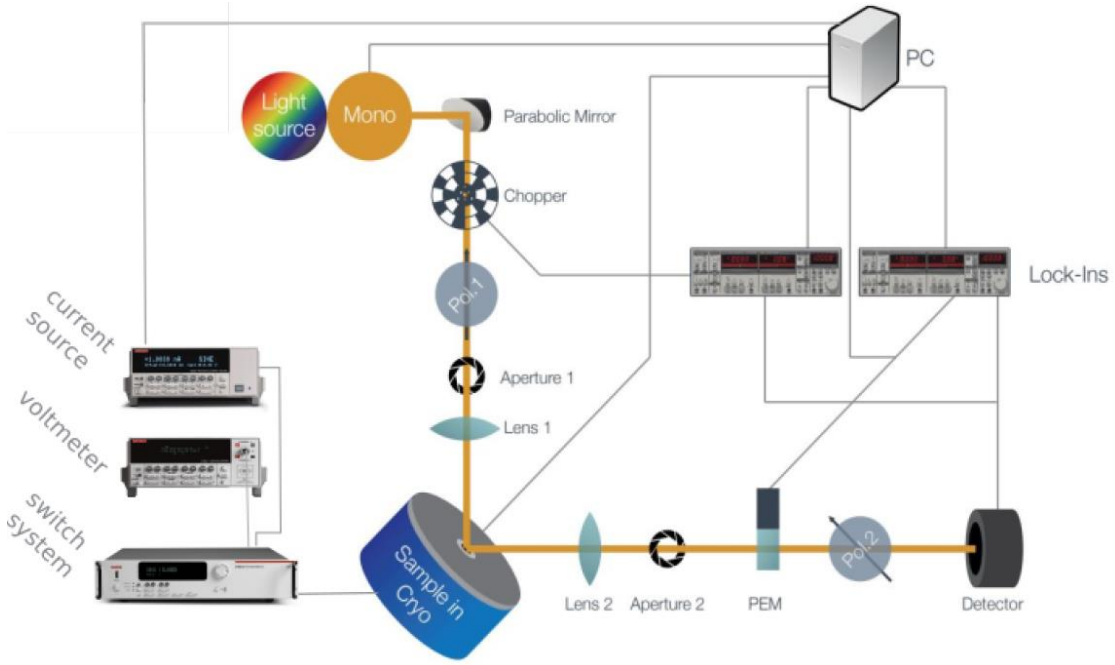

Figure 3.3: Schematic of the MOKE setup used for this thesis (the figure from S. Schäfer and J. Schoepf, Master's thesis[14,15]).

Figure 3.1 illustrates very schematically also the apparatus of RHEED. The electron beam, produced and accelerated in an electron gun, passes through a small aperture, and it is focused on a fluorescence screen by a (magnetic) focusing lens. The beam is deflected by deflection coils to irradiate the sample surface with a defined glancing angle of incidence. The RHEED pattern is observed on the fluorescence screen, which is placed inside the view port flange of the vacuum chamber and can be recorded by an external photo camera. The spot intensity and profile are analyzed later from the stored images or in real-time with a CCD-PC system. Alternately, the spot intensity can be measured directly as current by a Faraday cage, a small metal cage to collect the aimed diffracted beam, which is connected to a picoammeter.

3.2 Magnetooptical Kerr effect (MOKE) and magneto-transport measurements

3.2.1 MOKE measurements

A pivotal idea to increase the sensitivity of MOKE measurements and improve the signal-to-noise ratio is to use modulation techniques based on lock-in phase detection. A polarization spectroscopy setup based on the double-modulation (DM) technique (DMT) described in Refs[14-16] was constructed in this work. The light polarization rotation with an excellent signal-to-noise ratio can be measured by using the DM and

Table 3.1: Properties and specifications of the cryostat microstatMO, polarization spectrometer, and electrical transport setup (a: inferred from my measurements).

System properties	Specification
Sample temperature T range	8 K - 300 K[16]
Temperature stability ΔT at 10 K (During magnetic field sweep; rate: 0.3T/min)	0.05 K[a], 0.1 K[15], 0.2 K[16]
Magnetic field μH range	± 5 T[16]
Wavelength λ range	350 nm - 1500 nm[16]
Spectral resolution Δλ	5 - 10 nm[16]
Polarization rotation sensitivity (at 540nm ± 10nm)	0.005°[16]
Current source I range	0.1 pA to 105 mA[17]
Voltage V range (resolution)	10 mV(1nA) to 10V (1μV)[18]
Voltage accuracy ΔV 10mA range	±(60 ppm of reading + 40 nV)[18]

lock-in technique.

A schematic of the polarization spectroscopy setup is shown in figure 3.3. The devices used for Hall measurements are shown on the left of the cryostat. The devices and optical components are shown on the right. The light source with tunable wavelength is a Xe-lamp, a monochromator directly attached to it. A parabolic mirror collimates the delivering Light, subsequently sent through an optical chopper with a frequency of 680 Hz, modulating the signal into a square shape. The light becomes linear polarized by passing through a Glan-Taylor prism (Pol 1). Then the inhomogeneous light is cut by the aperture 1 and focused on the sample inside the cryostat by a biconvex lens (Lens 1). A second biconvex lens polarized the reflected light. A photoelastic modulator (PEM) modulates the polarization state of the light with a frequency of 50 kHz. A photodiode detector measures the light intensity. One can obtain the intensity components I_{DC}, I_{1f}, and I_{2f} from two Lock-Ins. A summary of the system specifications is given in table 3.1. The output of a 450 W Xe lamp is monochromatized with a JobinYvon MicroHR F = 140 mm monochromator. The light is subsequently collimated with a parabolic mirror, and s-polarized with a Glan-Taylor prism, and focused on the sample with a biconvex lens. When using an F = 15 cm lens, a spot size of ~1 mm^2 is obtained. A mechanical chopper modulates the incident light to determine the reflected or transmitted quasi-DC intensity I_{DC}. Samples can be placed in an Oxford MagnetoStatMO superconducting magnet. The transmitted or reflected light is refocused with a biconvex lens through a photoelastic modulator PEM-100 Hinds Instruments and a second Glan-Taylor polarizer onto a silicon photodiode. The PEM modulates the light polarization state with a 50 kHz frequency. The phase difference is generally set to $\delta_0 = 150.5^\circ$ to ensure a trade-off in modulation efficiency

for the ellipticity and rotation. The ellipticity is proportional to the f = 50 kHz signal, and the polarization plane rotation is proportional to the $2f$ = 100 kHz signal. The second Glan-Taylor prism acts as an analyzer for the polarization state. The intensity components I_{DC}, I_{1f}, and I_{2f} are read out by two lock-ins (Ametek Signal Recovery 7230), of which one measures I_{1f} and I_{2f} simultaneously. Rotation spectra can be taken over a wavelength range of 350 -1500 nm. The typical spectral resolution is $\Delta\lambda$ ~5 - 10 nm depending on the central wavelength and monochromator slit width. A magnetic field can be applied (and swept) between ± 5 T. The sample temperature can be set (and swept) between 8 - 300 K. For small rotation θ and ellipticity ϵ the relation between measured intensities, and θ, and ϵ is:

$$\varepsilon_m \approx C_2 \frac{I_{1f}}{I_{DC}} \qquad \theta \approx C_2 \frac{I_{2f}}{I_{DC}} \tag{3.1.}$$

The rotation calibration constant C_2 is determined by rotating the incident polarization for a known rotation. The details calibration of the rotation for the measurement is mentioned in Chapter 2.

The rotation sensitivity for λ = 540 nm (10 nm bandwidth) probe light is experimentally determined by measuring $\theta_K(H_a)$ on a sample with small magnetization. The slightest detectable polarization rotation is about ± 5 mdeg.

3.2.2 Magneto-transport measurement

In this work, the cryostat from Oxford Hall effect measurement systems was used to characterize electrical properties, such as, temperature dependent sheet resistance, magnetoresistance, and Hall resistance[15]. The van der Pauw method was used for the electrical measurements[19,20].

The van der Pauw method uses a four-point probe placed at the edges of the sample. However, the sample must be homogeneous flat with uniform thickness. The size of the contacts and their location on the sample can significantly affect the measurement accuracy. To improve measurement accuracy, the area of each contact should be at least an order of magnitude smaller than the area of the entire sample. The electrical properties of the contacts were checked by measuring current as a function of voltage. For ohmic contacts, the I - V curve should exhibit linear behavior.

A schematic diagram of the van der Pauw geometry is shown in figure 3.4. During the magnetoresistance measurement, current flows along one side of the sample (probes 1 and 2 in figure 3.4(a)) while the voltage is measured along the opposite side (probes 3 and 4 in figure 3.4(a)). According to Ohm's law, the resistance can be calculated as:

$$R_{xx} = \frac{V_{43}}{I_{21}} \tag{3.2.}$$

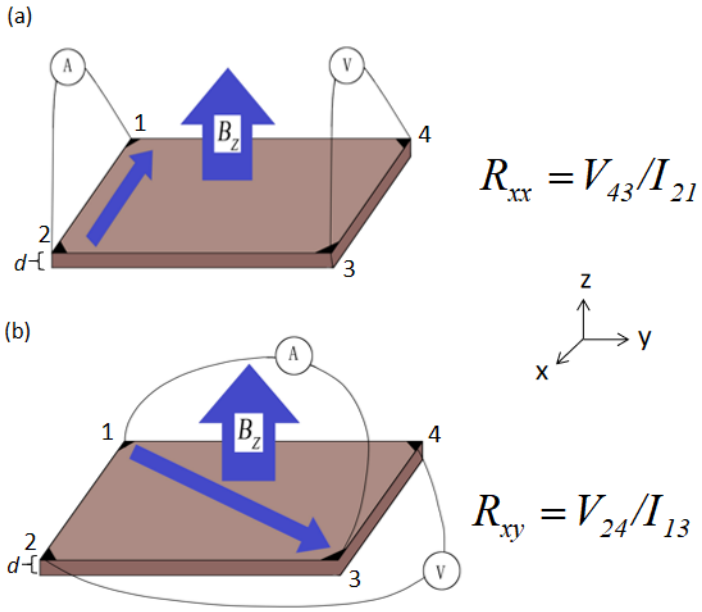

Figure 3.4: (a) and (b) Van der Pauw geometry for a square thin film sample. The black corners with numbers show electrical contacts. B_z is the magnetic field applied perpendicular to the sample surface for magnetoresistance and Hall resistance measurements.

The fundamental physical principle of Hall measurements is the Hall effect[21]. As displayed in figure 3.4(b), an electric current flows through a conductor (probes 1 and 3) in a magnetic field (B_z). The magnetic field exerts a transverse force on the moving charge carriers, pushing them to one side of the conductor. Here, the magnetic field B_z is perpendicular to the sample surface. The voltage is measured along the diagonal direction (probes 2 and 4). The Hall effect resistance is given by:

$$R_{xy} = \frac{V_{24}}{I_{13}} \qquad 3.3.$$

To calculate the magetoresistance and Hall resistance with the equations 3.2 and 3.3 in Van der Pauw geometry, symmetry considerations should be considered. More precisely, the longitudinal magnetoresistance is an even function of the applied field. In contrast, the ordinary and the anomalous Hall effect (AHE) are odd functions of the applied field and the sample magnetization, respectively.

In the experiment, there are two methods to perform the electrical resistivity and the Hall effect measurement with the van der Pauw geometry, i.e., the methods of reversing the magnetic field and without reversing its direction. The method of reversing the magnetic field is based on the Hall potential changing its sign (but not the absolute value) after reversing the magnetic field. In contrast, the longitudinal potential remains the same. The non-Hall potentials can be thus eliminated after two measurements in both field directions (H, –H). Here, we must keep in mind that the polarity of the injected current should be kept the same. So, the longitudinal and Hall voltages can be calculated by:

$$V_{xx} = \left(\frac{V_{24,13}(\mathrm{H}) - V_{24,13}(-\mathrm{H})}{2} \right) \quad 3.4$$

$$V_{xy} = \left(\frac{V_{24,13}(\mathrm{H}) + V_{24,13}(-\mathrm{H})}{2} \right) \quad 3.5$$

where the $V_{24,13}$ is defined as the voltage between points 2 and 4 when an applied current flows through contacts 1 and 3(see figure 3.4b). In the method without reversing the applied magnetic field, the voltage can be detected by permutation of voltage and current contacts (see figure 3.2). Any pair of contacts can be used as current or voltage contacts. From the reciprocity theorem, it follows that $V_{13,24}(-H) = V_{24,13}(H)$[22,23]. Thus, combining the equations 3.4 and 3.5, the Hall and longitudinal voltages can now be reformulated as:

$$V_{xx} = \left(\frac{V_{24,13}(\mathrm{H}) - V_{13,24}(\mathrm{H})}{2} \right) \quad 3.6$$

$$V_{xy} = \left(\frac{V_{24,13}(\mathrm{H}) + V_{13,24}(\mathrm{H})}{2} \right) \quad 3.7.$$

Here, we strength that we take the second method without reversing the applied magnetic field since only one resistance measurement configuration and only one quadruple of connections is necessary.

3.3 Atomic Force Microscopy (AFM)

The Atomic Force Microscope (AFM) is based on a scanning probe technique where the probe is a sharp tip that is rastered across the sample surface to map the topography[24]. In an atomic force microscope, the displacement of a cantilever is employed to probe the interaction with the surface of a sample. Typically, an atomically sharp scanning tip attached to an elastic cantilever serves as a spring. Forces acting between scanning tip and sample can be used as the imaging information upon scanning the tip over the sample surface.

The basic configuration for our AFM is shown in figure 3.5. This AFM is typically used to measure a wide variety of samples with relatively small roughness. The interaction force between the atoms at the sample's surface and those at the cantilever's tip can be detected by monitoring how much the cantilever deflects. This deflection of the cantilever can be quantified by the measurement of a beam reflected off the backside of the cantilever and onto the Position Sensitive Photo Detector (PSPD). The tube-shaped

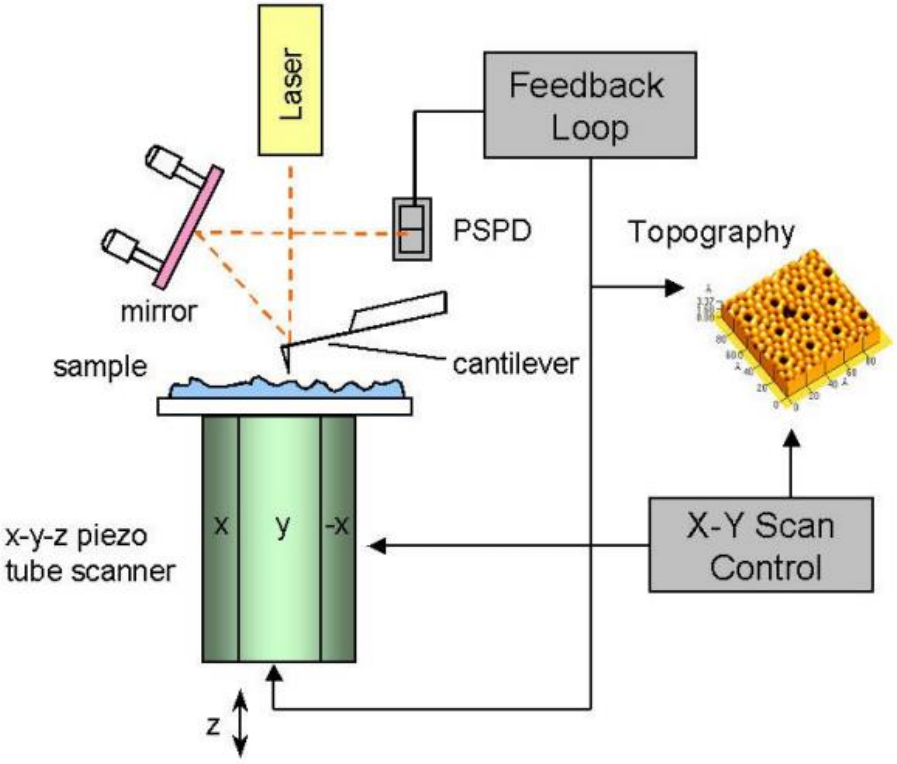

Figure 3.5: Scheme of work principles of conventional AFM microscope. (Reproduced from Park Systems NX10 User's Manual).

scanner under the sample moves a sample in the horizontal direction (X-Y) and the vertical direction (Z). It repetitively scans the sample line by line, while the PSPD signal is used to establish a feedback loop that controls the vertical movement of the scanner as the cantilever moves across the sample surface.

In this work, a Park NX10 (Park Systems Corp., Suwon, Korea) is used. The cantilever is excited to oscillate at a frequency of f ≈ 280 - 330 kHz with a free amplitude of A ≈ 14 nm (70% of free amplitude is used as setpoint amplitude). The freely available software Park Systems XEI (Copyright © January 2011 Park Systems Corp.) is employed to process and visualize the raw data acquired

3.4 Superconducting Quantum Interference Device (SQUID) magnetometer

A SQUID magnetometer is used to measure the magnetic moment of samples, in particular being sensitive to small magnetic signals. The core components of a SQUID magnetometer are ring-shaped superconductors with a pair of Josephson junctions and are shown in figure 3.6 (a). As a magnet sample passes through the ring, the change of magnetic flux in the ring causes voltages in the junctions.

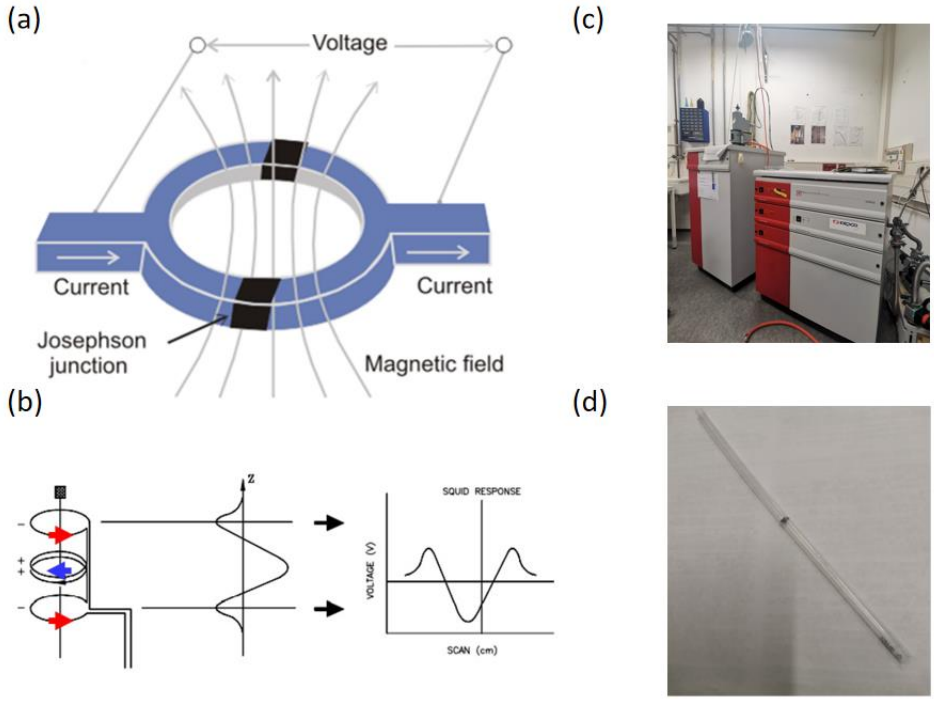

Figure 3.6: (a) Diagram of SQUID[25]: A superconducting ring with Josephson junctions. (b) Signal response from 4-ring geometry as a function of position, red and blue arrows indicating opposite ring voltage response (figure source: Quantum Design MPMS manual). (c) Superconducting Quantum Interference Device (d) Typical sample of a ferromagnetic heterostructure grown on a diamagnetic $SrTiO_3$ substrate, mounted inside a nonmagnetic plastic straw.

Quantum Design Magnetic Property Measurement System (MPMS) has a built-in SQUID setup with 4-rings geometry, as shown in figure 3.6 (c). The SQUID shows a different response against the scan length when a sample travels through a different location among the 4-ring geometry. The output indicates the sample is too high and must be lowered (see figure 3.6 (b)). The motion can be linear or linear with small oscillation, corresponding to the measurement mode of DC or RSO, respectively. The RSO provides better sensitivity and is therefore used for this dissertation on the ultra-thin films, which will be described in the experimental part of chapter 5. Thin films on a substrate are usually cut into a 4mm × 4mm piece and fixed in straw with a negligible diamagnetic response, as shown in figure 3.6(d).

3.5 X-Ray Magnetic Circular Dichroism (XMCD)

XMCD is one of the key methods for microscopic investigations of magnetic systems, which has been pioneered by professor Gisela Schütz[26]. The XMCD is based on the magnetization dependent on the variation of the x-ray absorption coefficient of circular polarized x-rays present in a vicinity of an absorption edge. XMCD enables one to determine spin and orbital magnetic moments.

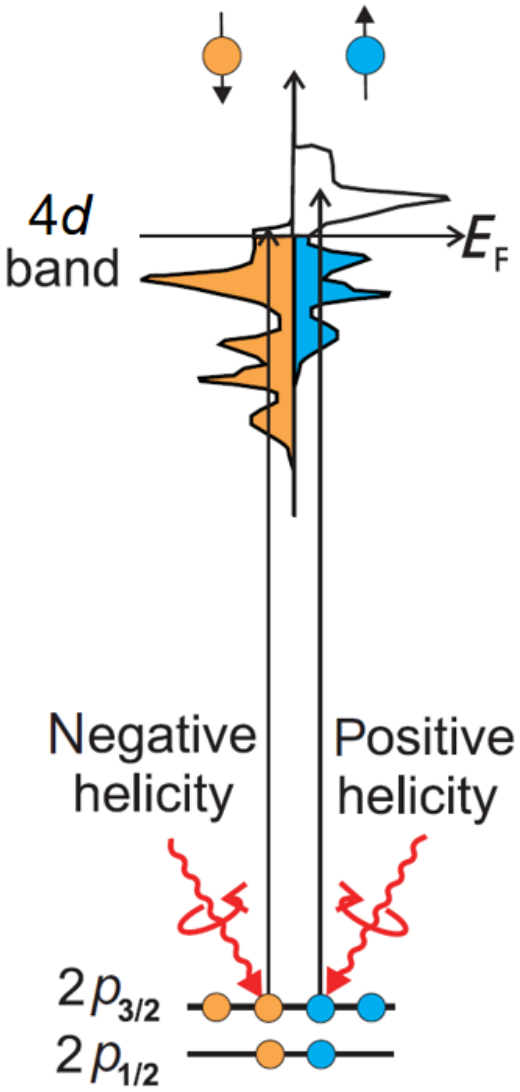

Figure 3.7: Illustration of the XMCD effect at the L-edge absorption for $SrRuO_3$ showing density of states for the spin-up and spin-down. The figure is adapted from Ref. [27].

To understand the XMCD principle, here we explain it with the vital material $SrRuO_3$. $SrRuO_3$ with Ru^{4+} nominally has four *d*-orbital electrons in a low-spin configuration, where three electrons occupy the majority spin channel, while the fourth electron resides in the minority spin channel with occupational degeneracy among the three Ru t_{2g} orbitals. In figure 3.7, we see a typical magnetic L-edge transition of $SrRuO_3$ in which the 2*p* band is split by spin-orbit coupling and the 4*d* band is exchanged split into spin-up and spin-down bands. The density of states of the 4*d* band is different for spin-up and spin-down electrons, resulting in a different transition probability for different spin states, as required by Fermi's Golden Rule. Thus, the 4*d* band may act as a detector of spin states. In addition, XMCD operates by additionally exploiting the selection rules for atomic transitions. The two 2*p* subbands have opposite spin-orbit coupling, and the state mixing which occurs in these core levels results in

one of the levels being more likely to excite a spin-up electron while the other is more likely to excite a spin-down electron. This polarization of the excitation combines with the spin sensitivity of the 4*d* band to yield magnetic information. By switching the magnetization direction, the majority and minority 4*d* spin bands will switch, causing the intensity of one L-edge to rise and the other to fall. In a nonmagnetic system, the intensity would remain constant, as there would be more majority or minority spin bands. Similarly, in a system without spin-orbit coupling (a K-edge, for example), the L_3 and L_2 edge would excite equal numbers of spin-up and spin-down electrons, and switching the magnetization would have no observable effect. Both factors are required, and when present, they result in significant dichroism of the x-ray absorption signal as the magnetization of the sample reverses direction.

To perform the XMCD experiment, samples are illuminated by a beam of circularly polarized x-rays while magnetized alternatively parallel and antiparallel to the axis of photon polarization by an alternating magnetic field. The energy of the incoming photons is swept through an elemental absorption edge, and an absorption spectrum is taken for both the parallel and antiparallel magnetization state. Then we extract element specific magnetic information such as which elements and energy levels are ordering magnetically, the relative magnitude of a ferromagnetic signal, and, through the application of the XMCD sum rules, the ratio of orbital magnetic moment and spin magnetic moment based on the difference between the circularly polarized light (c+ and c−). The XMCD intensity is proportional to the magnetization M of the sample projected to the photon propagation direction and the angular momentum L_{ph} of the photons:

$$\Delta I_{\mathrm{XMCD}} = I^{\delta+} - I^{\delta-} = I^{\uparrow Lph\uparrow M} - I^{\downarrow Lph\uparrow M} \qquad 3.8.$$

For maximum XMCD effect, the M and L_{ph} have to be parallel to each other.

3.6 References

1 J. Mannhart and D. G. Schlom, **327** (5973), 1607 (2010).

2 E.-M. Choi, A. Kursumovic, O. J. Lee, J. E. Kleibeuker, A. Chen, W. Zhang, H. Wang, and J. L. MacManus-Driscoll, ACS Applied Materials & Interfaces **6** (17), 14836 (2014).

3 H. Lowndes Douglas, D. B. Geohegan, A. A. Puretzky, D. P. Norton, and C. M. Rouleau, Science **273** (5277), 898 (1996).

4 S. Majumdar and S. van Dijken, JOURNAL OF PHYSICS D-APPLIED PHYSICS **47** (3) (2014).

5 K. Y. Yun, D. Ricinschi, T. Kanashima, M. Noda, and M. Okuyama, Japanese Journal of Applied Physics **43** (No. 5A), L647 (2004).

6 D. Dijkkamp, T. Venkatesan, X. D. Wu, S. A. Shaheen, N. Jisrawi, Y. H. Min-Lee, W. L. McLean, and M. Croft, Applied Physics Letters **51** (8), 619 (1987).

7 K. Matsumoto, T. Horide, A. Ichinose, S. Horii, Y.Yoshida, and M. Mukaida, Japanese Journal of Applied Physics **44** (No. 7), L246 (2005).

8 D. B Chrisey and G. K. Hubler., C., D. B., & Hubler, G. K. (Eds.). (1994).

9 T. Ohnishi, T. Yamamoto, S. Meguro, H. Koinuma, and M. Lippmaa, 2007 (unpublished).

10 H. N. Lee, H. M. Christen, M. F. Chisholm, C. M. Rouleau, and D. H. Lowndes, Nature **434** (7034), 792 (2005).

11 G. J. H. M. Rijnders, G. Koster, D. H. A. Blank, and H. Rogalla, Applied Physics Letters **70** (14), 1888 (1997).

12 J. Shen, Z. Gai, and J. Kirschner, Surface Science Reports **52** (5), 163 (2004).

13 L. Wysocki, J. Schöpf, M. Ziese, L. Yang, A. Kovács, L. Jin, R. B. Versteeg, A. Bliesener, F. Gunkel, L. Kornblum, R. Dittmann, P. H. M. van Loosdrecht, and I. Lindfors-Vrejoiu, ACS Omega **5** (11), 5824 (2020).

14 S. Schäfer, Master's thesis, University of Cologne. (2015).

15 J. Schoepf, Master's thesis, University of Cologne, (2019).

16 R. B. Versteeg, Ph.D. thesis, University of Cologne (2019).

17 Keithley Instruments, document Number:622x-900-01 Rev. B, Model 6220 DC Current Source, Model 6221 AC and DC Current Source, User's Manual, Keithley Instruments (2005).

18 Keithley Instruments, document Number: 2182-900-01 Rev. D, Model 2182 Nanovoltmeter, User's Manual, Keithley Instruments (2002)

19 L.J. van der Pauw, Philips Research Reports. **13**, 1 (1958).

20 L.J. van der Pauw, Philips Technical Review. **20**, 220 (1958).

21 “The Hall Effect”. NIST. Archived from the original on 2008-03-07. Retrieved 2008-02-28. (2008).

22 I. Janeček and P. Vašek, Physica C: Superconductivity **390** (4), 330 (2003).

23 I. Janeček and P. Vašek, Physica C: Superconductivity **402** (1), 199 (2004).

24 F.J. Giessibl, Reviews of Modern Physics **75** (3), 949 (2003).

25 S. R. A. Venkata, Ph.D. thesis, University_of_Basel, 2018.

[26] G. Schütz, W. Wagner, W. Wilhelm, P. Kienle, R. Zeller, R. Frahm, and G. Materlik, Physical Review Letters **58** (7), 737 (1987).

[27] J. Stöhr and H.C. Siegmann, *Magnetism: From Fundamentals to Nanoscale Dynamics*. (Springer Berlin Heidelberg, 2017).

Chapter 4 Origin of the hump anomalies in the Hall resistance loops of ultrathin $SrRuO_3/SrIrO_3$ multilayers

Contents

Lin Yang,[1] Lena Wysocki,[1] Jörg Schöpf,[1] Lei Jin,[2] András Kovács,[2] Felix Gunkel,[3] Regina Dittmann,[3] Paul H. M. van Loosdrecht,[1] and Ionela Lindfors-Vrejoiu[1]

[1]Institute of Physics II, University of Cologne, 50937 Cologne, Germany
[2]Ernst Ruska-Centre for Microscopy and Spectroscopy with Electrons, Forschungszentrum Jülich GmbH, 52425 Jülich, Germany
[3]PGI-7, Forschungszentrum Jülich GmbH, 52425 Jülich, Germany

PHYSICAL REVIEW MATERIALS **5**, 014403 (2021) ©2021 American Physical Society
Doi：https://doi.org/10.1103/PhysRevMaterials.5.014403

Author contributions to this publication:

The main contribution to the publication comes from Lin Yang**,** Ionela Lindfors-Vrejoiu, and Paul H. M. van Loosdrecht. The contributions from the other co-authors and for further investigations that were not published are as below:

1) Lei Jin carried out the scanning transmission electron microscopy measurement and provided me with the initial data analysis
2) Lena Wysocki performed the superconducting quantum interference device (SQUID) measurement and joined the data analysis.
3) Lena Wysocki grew the part of samples with PLD together with Ionela Lindfors-Vrejoiu.
4) The magneto-optical Kerr effect (MOKE) and Hall measurement was finished with the assistance of Jörg Schöpf and Lena Wysocki.
5) András Kovács, Felix Gunkel, Regina Dittmann contributed with STEM investigations and assistance with PLD sample fabrication at FZ Jülich.
6) Francoual, Sonia, Linares Mardegan, Jose Renato, and Lena Wysocki helped me with the x-ray magnetic circular dichroism (XMCD) measurement and data analysis.
7) Michael Ziese provided us with constant valuable advice on the physical properties of $SrRuO_3$ samples, and with the SQUID and Hall measurements
8) René Borowski etched the STO substrates at FZ Jülich, and Susanne Heijligen assisted me with the SQUID measurements.
9) All the participants joined in the discussion of data and reviewed the paper, and agreed to publish this work.

4.1 Abstract

The proposal that very small Néel skyrmions can form in $SrRuO_3/SrIrO_3$ epitaxial bilayers and that the electric field effect can be used to manipulate these skyrmions in gated devices strongly stimulated the recent research of $SrRuO_3$ heterostructures. A strong interfacial Dzyaloshinskii-Moriya interaction (DMI) was considered the driving force for the formation of skyrmions in $SrRuO_3/SrIrO_3$ bilayers. Here, we investigated nominally symmetric heterostructures in which an ultrathin ferromagnetic $SrRuO_3$ layer is sandwiched between large spin-orbit coupling $SrIrO_3$ layers, for which the conditions are not favorable for the emergence of a net interfacial DMI. Previously the formation of skyrmions in the asymmetric $SrRuO_3/SrIrO_3$ bilayers was inferred from anomalous Hall resistance loops showing hump-like features that resembled topological Hall effect (THE) contributions. Symmetric $SrIrO_3/SrRuO_3/SrIrO_3$ trilayers do not show hump anomalies in the Hall loops. However, the anomalous Hall resistance loops of symmetric multilayers, in which the trilayer is stacked several times, do exhibit the hump-like structures, similar to the asymmetric $SrRuO_3/SrIrO_3$ bilayers. The origin of the Hall effect loop anomalies likely resides in unavoidable differences in the electronic and magnetic properties of the individual $SrRuO_3$ layers rather than in the formation of skyrmions.

4.2 Introduction

Topologically protected magnetic whirls, dubbed as magnetic skyrmions, are considered to be ideal candidates for the potential application in future data storage[1]. This primarily derives from their small size and room temperature stability[2-4], low energy consumption[3-7], and topological protection[8-10]. Epitaxial perovskite oxide heterostructures, such as $SrRuO_3/SrIrO_3$, are considered to have strong interfacial DMI due to the broken spatial inversion symmetry and the strong spin-orbit coupling in $SrIrO_3$, and it was reported that Néel skyrmions form in these heterostructures[11,12]. The insulating nature of perovskite oxide heterostructures, such as ultrathin $SrRuO_3/SrIrO_3$, makes them promising systems in terms of electric field manipulation as well as the ability to engineer their magnetic properties. Magnetic skyrmions can in principle, be observed in real space by magnetic force microscopy (MFM)[13], Lorentz transmission electron microscopy (LTEM)[14], scanning transmission x-ray microscopy (STXM)[3], spin- polarized scanning tunneling microscopy (SP-STM)[15], x-ray magnetic circular dichroism based photoemission electron microscopy (XMCD-PEEM)[16], spin-polarized low energy electron microscopy (SPLEEM)[17], and in reciprocal space by small-angle neutron scattering (SANS)[18] and resonant small-angle x-ray scattering (SAXS)[19]. However, for epitaxial oxide heterostructures, by using these techniques, the direct observation of sub-100 nm size skyrmions and their characterization becomes extremely challenging. Therefore, the possibility of examining the formation of skyrmions by magnetotransport measurements is very attractive as Hall resistivity investigations are rather easy to perform in any solid state research laboratory. Recently,

there were many reports in which the formation of skyrmions was inferred from the observation of hump-like anomalies of Hall resistance loops that were attributed to the manifestation of the THE. This is the case of quite a few reports related to epitaxial $SrRuO_3$ heterostructures and to bare $SrRuO_3$ thin films[20-22]. J. Matsuno *et al.*[11] attributed the observation of such features of Hall loops measured for ultrathin ferromagnetic SrRuO3 [thinner than six pseudocubic unit cells (uc)] capped by two uc $SrIrO_3$ thick layers to the formation of skyrmions. Many similar publications followed shortly. There were reports of the hump-like features observed in Hall resistance loops of a variety of $SrRuO_3$ based samples: $SrRuO_3/SrIrO_3$ multilayers with relatively thick layers (10 uc thick $SrRuO_3$)[23], $BaTiO_3/SrRuO_3$ bilayers[24], $SrRuO_3$ (5 uc)/$SrIrO_3$ (2 uc) in which the iridate layer was the bottom layer on the $SrTiO_3$ substrate[25], $SrRuO_3$ (8 uc)/$BaTiO_3$ (2 uc) bilayers on $SrTiO_3$[26], $SrIrO_3$ (2 uc)/$SrRuO_3$ (10 uc) bilayers for which MFM experiments were also performed[12], or relatively thick $SrRuO_3$ (3–6 nm) films grown in low oxygen pressure[27]. Different mechanisms for the occurrence of the interfacial DMI were proposed in these papers, adapted to the particular interfaces and sample peculiarities. However, the interpretation of the observed humps in anomalous Hall effect (AHE) resistance loops as a fingerprint of the THE contribution due to skyrmions is currently under debate. Other reports addressed the possible role played by $SrRuO_3$ layer inhomogeneity, such as Ru/O vacancies[28], thickness variations[29-31], crystal structure distortions[26,32], and intermixing[33] in the occurrence of the THE-like features of the AHE loops. This division of opinions concerning the origin of the THE-like structures of the Hall resistance loops calls for a careful analysis and understanding of the electronic and magnetotransport properties of $SrRuO_3$-based heterostructures. We stress that there are no direct measurements of the magnitude of the interfacial DMI in such epitaxial $SrRuO_3$-based heterostructures, but only the theoretical proposal from Ref. [11], which does not however provide any quantitative microscopic description of how the DMI is generated at the $SrIrO_3/SrRuO_3$ interfaces. There exists very little insight into the interfacial DMI at epitaxial oxide interfaces[34], although hints for the existence of an interfacial DMI in $SrIrO_3$ (2 uc)/$SrRuO_3$ (10 uc) bilayers were inferred from the analyses of the magnetic domain wall chirality[12]. We previously studied asymmetric $SrZrO_3/SrRuO_3/SrIrO_3$ and $SrHfO_3/SrRuO_3/SrZrO_3$ multilayers in which we aimed to observe the possible effects of the net interfacial DMI on the magnetotransport properties and magnetic domain formation[35]. However, these $SrRuO_3$ multilayers, with insulating spacers, were magnetically only very weakly coupled[36] and did not permit a conclusive investigation of the magnetic domains by magnetic force microscopy.

Here we deliberately considered $SrIrO_3/SrRuO_3/SrIrO_3$ epitaxial trilayers and multilayers with several repeats of the trilayer, in order to have interfaces as symmetric as possible in this material system. We aimed to eliminate, or at least minimize, the role of interfacial DMI. In a perfectly symmetric ultrathin film heterostructure the interfacial DMI should cancel out. However, for epitaxial interfaces of perovskite oxides (ABO_3), the interfaces are likely to be asymmetric due to the AO/BO_2 stacking imposed by epitaxial growth, due to asymmetric intermixing or different oxygen octahedral

rotations (OOR) angles at the upper and lower interface. For example, the strong influence of the type of interface stacking on the physical properties of perovskite oxide heterostructures was recently demonstrated for $SrIrO_3$-$La_{0.7}Sr_{0.3}MnO_3$ bilayers[37]. For our trilayers and multilayers, because A = Sr for both $SrRuO_3$ and $SrIrO_3$, the interfaces are either of the type $SrO/IrO_2//SrO/RuO_2$ or $IrO_2/SrO//RuO_2/SrO$, and from this viewpoint the interfaces are equivalent.

Prior investigations demonstrated that $SrRuO_3$ layers separated by two uc thick $SrIrO_3$ nonmagnetic layers are magnetically decoupled[38]. Therefore, the overall conditions in these $SrIrO_3/SrRuO_3/SrIrO_3$ multilayers strongly disfavor the formation of Néel skyrmions. The trilayer $SrIrO_3/SrRuO_3/SrIrO_3$ samples did not exhibit any hump- like anomalies in the Hall effect loops. In contrast, anomalies were observed over a large temperature range in Hall effect loops of nominally symmetric multilayer samples, in which a $SrRuO_3/SrIrO_3$ bilayer was stacked three or six times. The Hall effect loops with hump anomalies can result from inhomogeneous magnetic and electronic properties of the $SrRuO_3$ layers in the multilayers. The inhomogeneous properties possibly arise from layer thickness variation, different degrees of intermixing of Ir on the Ru site, and oxygen octahedron deformations that can be different for the $SrRuO_3$ layers next to the substrate and foe layers at the top of the multilayer[39].

4.3 Method

4.3.1 Sample growth

The heterostructures studied here, $SrIrO_3/[SrRuO_3/SrIrO_3]_m$ (m = 1, 6), were grown on $SrTiO_3$(001) by pulsed-laser deposition (PLD) using a KrF excimer laser (λ = 248 nm). $SrTiO_3$(001) single-crystal substrate was used for the deposition after NH_4F-buffered HF etching for 2–2.5 min and annealing at 1000 ◦C for two hours in the air. The oxygen partial pressure and deposition temperature were optimized at 0.133 mbar and 650 ◦C for the growth of all the layers. The pulse repetition rate of the laser was 5 Hz and 2 Hz for the $SrRuO_3$ layers and $SrIrO_3$ layers, respectively. The growth of each layer was monitored by high oxygen pressure reflective high-energy electron diffraction (RHEED). The thickness of each $SrRuO_3$ layer is nominally six uc and the thickness of each $SrIrO_3$ layer is nominally 2 uc (1 uc layer is ~0.4 nm thick). The samples were cooled in 100–200 mbar oxygen atmosphere from 650 ◦C down to room temperature with a rate of 10 ◦C/minute. A multilayer with m = 3, $SrIrO_3/[SrRuO_3/SrIrO_3]_3$, was grown in a second RHEED-PLD system (made by SURFACE systems+technology GmbH und Co. KG), under similar growth conditions, except for a higher laser fluence and target-to-substrate distance. The sample with m = 3, along with a second trilayer (m = 1) are made in this PLD system as the reference sample to further figure out the origin of humps anomalies of ultrathin $SrRuO_3/SrIrO_3$ multilayers

4.3.2 Sample characterization

The surface morphology of our samples was characterized by atomic force microscopy (AFM). The microstructure of the multilayers, in terms of sharpness of the interfaces, layer thickness, and element distribution, was investigated by high-angle annular dark field scanning transmission electron microscopy (HAADF-STEM) of cross-section specimens. The distribution of the atomic elements was observed with high resolution energy dispersive x-ray spectroscopy (EDX). Both STEM and EDX were performed using an electron probe aberration corrected FEI Titan 80–200 ChemiSTEM microscope equipped with in-column EDX detectors. Hall effect measurements were carried out in the four-point geometry (van der Pauw), with permutating contacts for antisymmetrization. Hall resistance loops were recorded both with a physical property measurement system (PPMS, Quantum Design Inc.) and with a homemade setup. The home setup enables the simultaneous measurement of Hall resistance and magneto-optical Kerr effect (MOKE). The polar MOKE studies were performed with the magnetic field applied perpendicular to the thin film surface with incoherent light from a Xe lamp. The probe wavelength was chosen in- dividually for each sample to reduce the contributions of optical artifacts, such as interference effects that can be present in heterostructures with ultrathin films of dissimilar oxides. Light of 491–520 nm wavelength was used for the $SrIrO_3/[SrRuO_3/SrIrO_3]_1$ trilayer, 630 nm wavelength was used for the $SrIrO_3/[SrRuO_3/SrIrO_3]_3$, and 610 nm wavelength was used for the $SrIrO_3/[SrRuO_3/SrIrO_3]_6$ multilayer.

The magnetic moment of the samples was measured as a function of temperature and magnetic field using a superconducting quantum interference device (SQUID) magnetometer (MPMS XL-7 from Quantum Design). The magnetic background due to the diamagnetic $SrTiO_3$ substrates was subtracted from the total magnetic response, and often also corrections for a ferromagnetic impurity contribution had to be applied [35].

4.4 Results and discussion

4.4.1 Microstructure investigations

In figure 4.1, the growth mode and the thickness of the individual layers of the multilayers were monitored by employing *in situ* high oxygen pressure reflective high-energy diffraction (RHEED). The average intensity of the RHEED specular spot as a function of time is shown in figure 4.1(a) and figure 4.1(c) for $SrIrO_3/SrRuO_3/SrIrO_3$ and $SrIrO_3/[SrRuO_3/SrIrO_3]_6$, respectively, both grown in the same PLD chamber at FZ Jülich under the same PLD parameters. The oscillations in the RHEED intensity-time curves during the $SrIrO_3$ deposition show that the iridate layers grew in a layer-by-layer growth mode: see a first clear oscillation followed by a more damped second oscillation, marked by the small black arrows, corresponding to the growth of two monolayers of $SrIrO_3$. $SrRuO_3$ layers grew in step-flow growth regime[40]. The similar RHEED intensity behavior indicates the homogeneous thickness of sample layers. The surface morphology of both $SrIrO_3/[SrRuO_3/SrIrO_3]_1$ and $SrIrO_3/[SrRuO_3/SrIrO_3]_6$ samples was investigated by atomic force microscopy (AFM) and is shown in figure 4.1(b) and

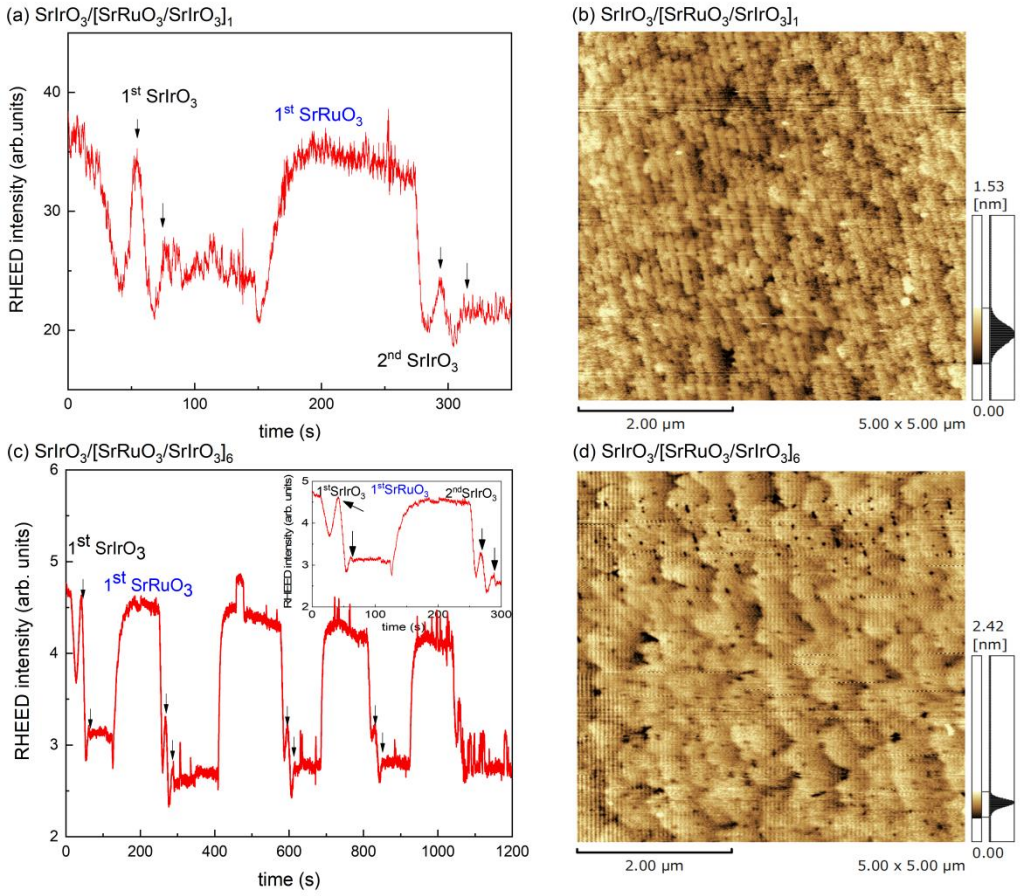

Figure 4.1: RHEED and AFM investigations of $SrIrO_3/[SrRuO_3/SrIrO_3]_1$ and $SrIrO_3/[SrRuO_3/SrIrO_3]_6$, which were grown under the same PLD conditions: (a) and (c) deposition time dependence of RHEED intensity; (b) and (d) AFM topography images (5 μm × 5 μm scans) of the top surface of the as grown samples. The small black arrows in (a) and (c) mark the top of the oscillations of the RHEED intensity signal during the growth of the $SrIrO_3$ layers. The inset in (c) shows the RHEED signal recorded during the growth of the first three layers of the multilayer $SrIrO_3/[SrRuO_3/SrIrO_3]$

figure 4.1(d), respectively. Non-continuous terrace-like structure is shown by the trilayer (see figure 1(b)) and the multilayer has a relatively large density of tiny holes, coming from probably incomplete coverage of the top most $SrIrO_3$ layer (see figure 4.1(d)).

The results of microstructure also investigations by HAADF-STEM and high-resolution EDX are summarized in figure 4.2. The overall structure of the heterostructures under study here, $SrIrO_3/[SrRuO_3/SrIrO_3]_m$ (m = 1, 3, 6) is shown in figure 4.2(a), whereas the symmetric unit cell structure of the repetitive trilayer building block is depicted in figure 4.2(c). Figures 4.2(b) and 2(d) show cross-sectional STEM images of the microstructure of the $SrIrO_3/[SrRuO_3/SrIrO_3]_6$ multilayer at low and high magnification, respectively. The stacking starts with a $SrIrO_3$ and individual $SrRuO_3$ and $SrIrO_3$ layers have thicknesses that match fairly well the expected thickness values

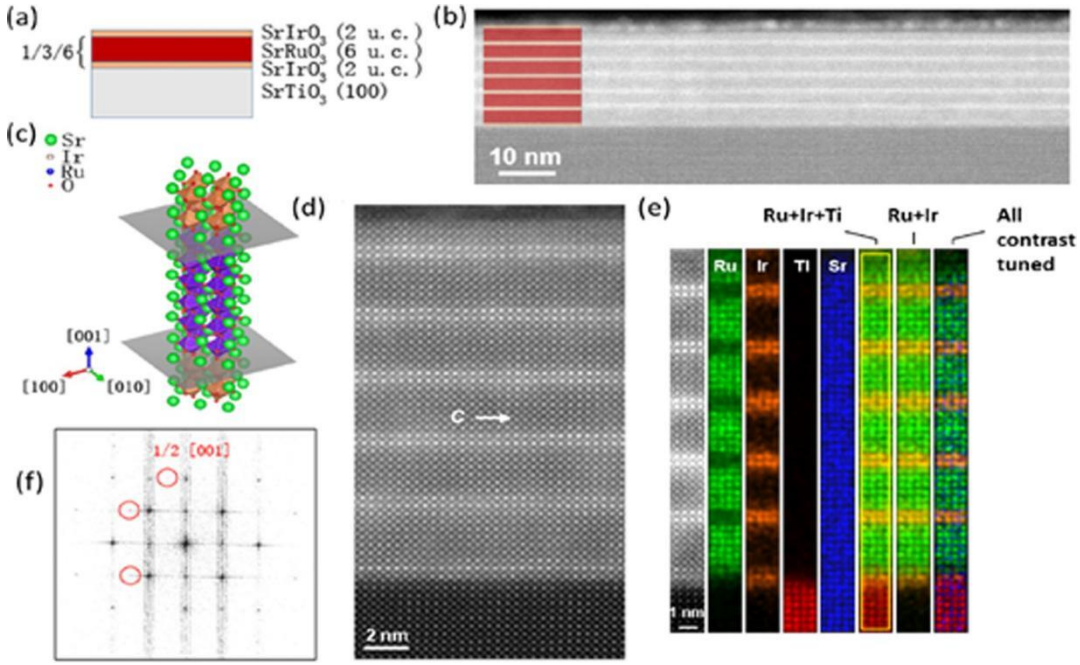

Figure 4.2: Microstructure investigations by scanning transmission electron microscopy. (a) Schematics of sample $SrIrO_3/[SrRuO_3/SrIrO_3]m$ (m = 1, 3, 6) grown on $SrTiO_3$(100) substrates. (b) An overview HAADF-STEM micrograph of sample $SrIrO_3/[SrRuO_3/SrIrO_3]_6$ indicates the layers are uniform (except for the top layer that was damaged during the FIB processing of the specimen). (c) Schematics of the structure of the trilayer $SrIrO_3/[SrRuO_3/SrIrO_3]_1$, for which a 6 uc $SrRuO_3$ layer is inserted between two $SrIrO_3$ layers (both 2 uc thick). Green, orange, blue, and red dots represent Sr, Ir, Ru, and O atomic column positions, respectively, in the crystal structure drawn using VESTA[41]. In (d) and (e) high magnification micrographs show the quality of the interfaces. EDX elemental mapping across the entire stacks shown in (e) probed the uniformity of chemical element distribution. (f) FFT pattern obtained from the image shown in (d), which shows the spots due to the reflections originating from the orthorhombic distortion (marked by red circles), and confirms the in-plane c-axis orientation of the layers [white arrow in (d)].

from the in situ RHEED monitoring of the layer deposition [see figure 4.2(c)]. The high-resolution image (see figure 4.2(d)) indicates coherent epitaxial growth of the layers, as no dislocations were detected across the entire stack in the investigated TEM specimen. The high resolution EDX mapping of the elements across the entire stacks [figure 4.2(e)] indicates that Ru and Ir are distributed as expected from the designed growth sequence, starting with a $SrIrO_3$ layer as the first layer on the substrate. We could not analyze quantitatively the exact stoichiometry of the individual layers. We show the Line profiles for each element in figure 4.3(b): they confirm that the $SrRuO_3$ layers are about 6-7 uc thick (as the number of individual Ru-O_2 planes varies between 6 and 7), while the $SrIrO_3$ layers are 2-3 uc thick (as the number of individual Ir-O_2 planes varies between 2 and 3), in agreement with our RHEED observations. In figure 4.3(b), we drew four lines, two in orange and the other two in green. The first orange (green) line marks the position of Ir (Ru), and the second orange (green) line marks the neighboring B-site positions. For both cases, the net count drops from 80 to 30. That

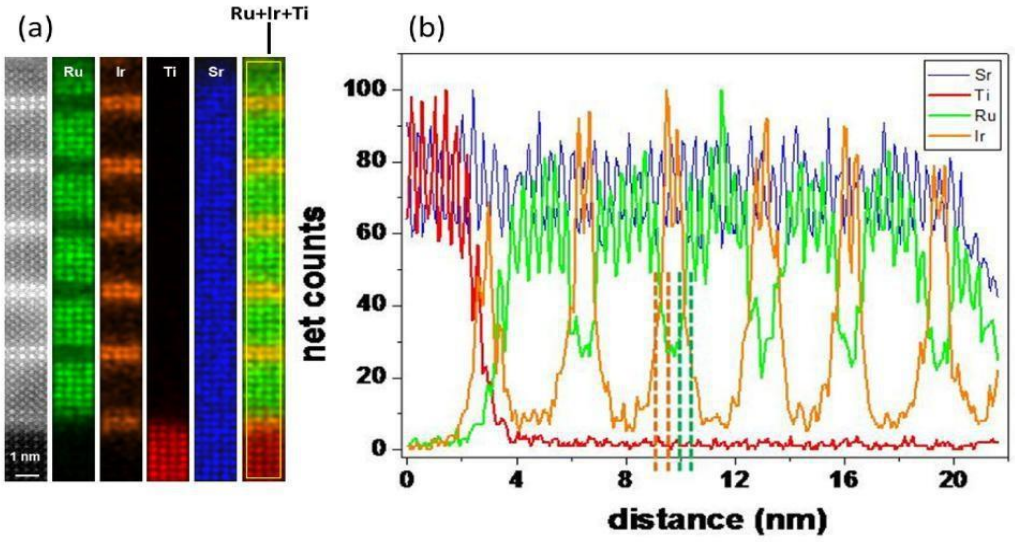

Figure 4.3: (a) HAADF-STEM and EDX analyses of a $SrIrO_3/[SrRuO_3/SrIrO_3]_6$ multilayer. The line profiles across the multilayer, starting from the substrate upwards in the growth direction, for the atomic column with the Sr, Ti, Ru, Ir ions are shown in (b).

means no matter what the element is, the decrease is the same. Only the thickness of the individual layers in the growth direction matters. The $SrIrO_3$ layers, being only 2-3 uc thick, are much too thin to allow quantitative analyses of the possible intermixing at the interfaces with the $SrRuO_3$ layers. To achieve atomic resolution in EDX investigations, due to the electron beam channeling, volume, and spectrum background effects, is very problematic. And the structure was analyzed by fast Fourier transform (FFT) images [see figure 4.2(f)] which confirm the in-plane c-axis orientation of the layers (see white arrow) and demonstrate the expected orthorhombic distortions (due to A-site atom displacements of the pseudocubic perovskite ABO_3) by the presence of extra reflections, marked by the red circles in figure 4.2(f).

For the sake of comparison with the symmetric trilayer samples, we fabricated a bilayer sample in our PLD system (at University of Cologne). The RHEED patterns and the analysis of the intensity variation of the RHEED specular spot acquired during the growth are shown in figure 4.4 (a) (d).). They demonstrate the high quality of the layers and that the 2 MLs thick $SrIrO_3$ bilayer grew in the layer-by-layer growth mode (as indicated by the two oscillations of the average intensity). The schematics of the bilayer are shown in figure 4.4 (e). The AFM topography images shown in the figure 4.4 (f) and figure 4.4 (g) confirm the smooth surface morphology.

4.4.2 Magnetic properties

We measured the dependence of the out-of-plane total magnetic moment as a function

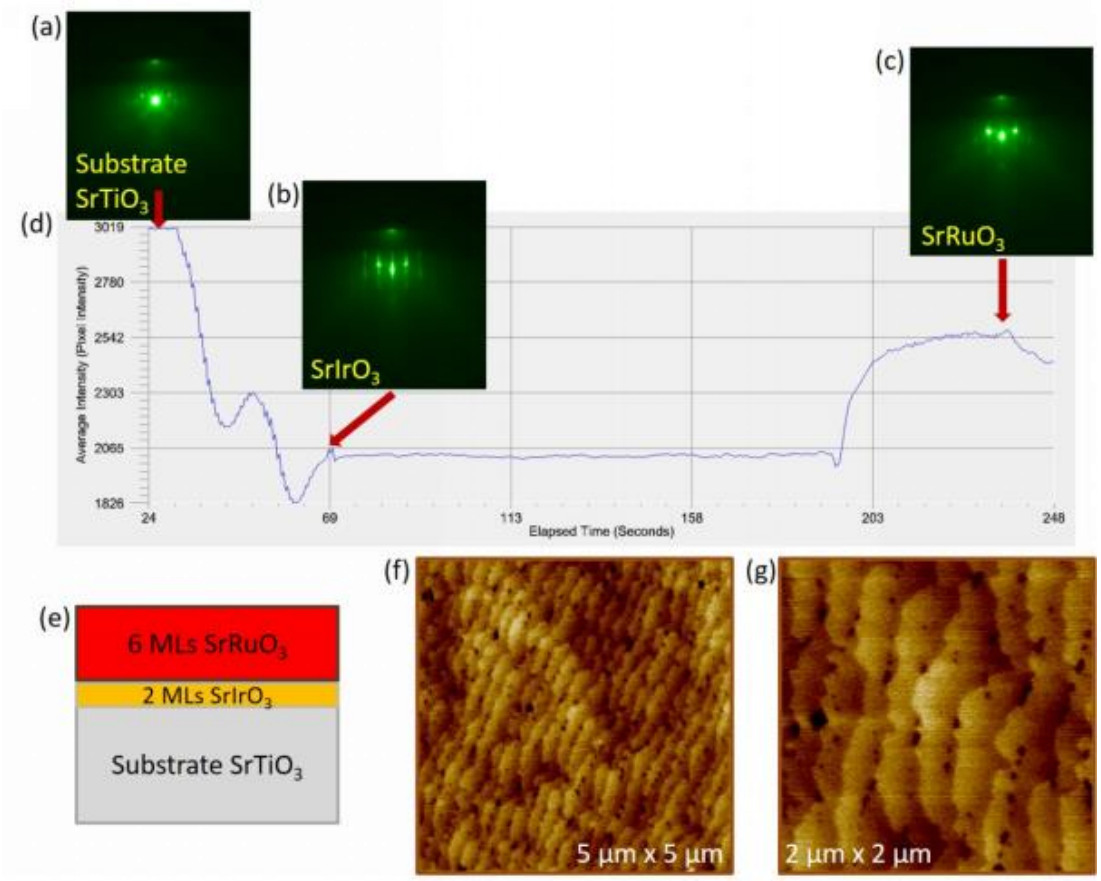

Figure 4.4: (a), (b) and (c) RHEED patterns of $SrRuO_3/SrIrO_3$ bilayer (with 2MLs thick $SrIrO_3$ bottom layer and 6 MLs thick $SrRuO_3$ top layer), which was grown under the same PLD conditions as the trilayer discussed in Section II. (d) RHEED intensity oscillation. (e) Schematics of the sample and (f) *ex situ* AFM topography images of the $SrRuO_3/SrIrO_3$ bilayer immediately after growth.

of temperature, under zero-field cooling [ZFC, measured while heating up in 0.1 Tesla (T) after cooling the sample with no applied field] and field cooled (FC) with a 0.1 T field applied perpendicular to the sample surface. The results for the $SrIrO_3/[SrRuO_3/SrIrO_3]_1$ trilayer and the $SrIrO_3/[SrRuO_3/SrIrO_3]_6$ multilayer are summarized in figure 4.5. For the trilayer sample, the Curie temperature (T_c) is 126 K, which was determined from the derivative of the FC magnetic moment curve as a function of temperature (see inset in figure 4.5(a)). The T_c of the 6 uc thick $SrRuO_3$ layer of this sample is lower than for the bulk $SrRuO_3$ single crystals (T_c = 160 K), which is typical for ultrathin films, due to epitaxial strain and disorder and stoichiometry effects, which are more pronounced the thinner the $SrRuO_3$ layers are[42]. The magnitude of the magnetic moment for $SrIrO_3/[SrRuO_3/SrIrO_3]_6$ is almost six times as large as $SrIrO_3/[SrRuO_3/SrIrO_3]_1$ (see the red dotted curve in figure 4.5(b)), corresponding to the magnetic volume relation of these two samples. Apparently two transitions at temperatures T_{c1} (120 K) and T_{c2} (140 K) occur for the $SrIrO_3/[SrRuO_3/SrIrO_3]_6$ epitaxial multilayers. We assume that the occurrence of two transition temperatures originates from the inhomogeneous magnetic properties of the

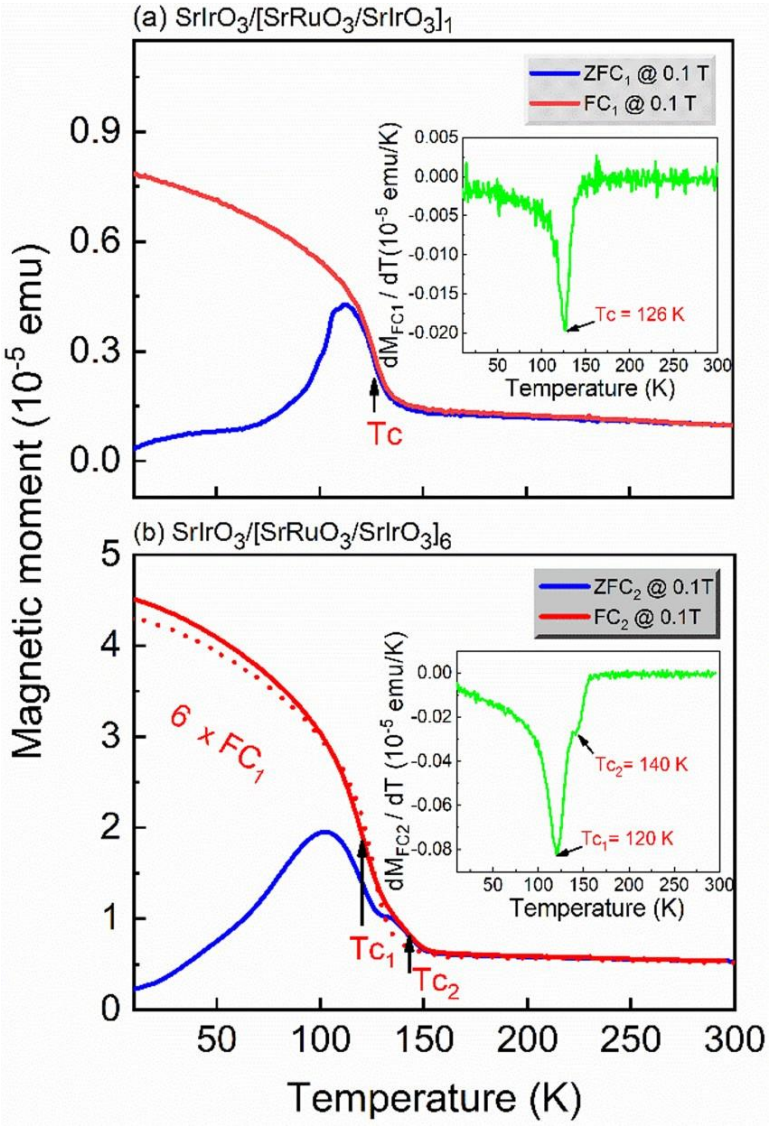

Figure 4.5: Temperature dependence of the magnetic moment of the samples (a) $SrIrO_3/[SrRuO_3/SrIrO_3]_1$ and (b) $SrIrO_3/[SrRuO_3/SrIrO_3]_6$ under zero field cooling (ZFC, blue plot) and field cooling (FC, red plot, 0.1 T applied perpendicular to the sample surface) conditions. The dotted red curve shown in (b) is the FC_1 curve of the trilayer sample from (a) multiplied by six and plotted for the sake of comparison. The insets in (a) and (b) show the first derivative of the magnetization with respect to temperature, used to determine the Curie transition temperatures of the $SrRuO_3$ layers.

$SrRuO_3$ layers. Most likely the six $SrRuO_3$ layers of the $SrIrO_3/[SrRuO_3/SrIrO_3]_6$ have all slightly different Curie temperatures distributed in the interval between T_{c1} and T_{c2}. Comparing with the transition temperature of the trilayer sample, which is 126 K, we are led to consider that the bottommost $SrRuO_3$ layer has the lowest Curie temperature, while the top $SrRuO_3$ layers have the largest Curie temperature. It is likely that the bottommost $SrRuO_3$ layers are most affected by the epitaxial strain and oxygen octahedral accommodation to the conditions of the $SrTiO_3$ substrate, resulting in suppressed Curie temperature. The topmost $SrRuO_3$ layers of the multilayer may have

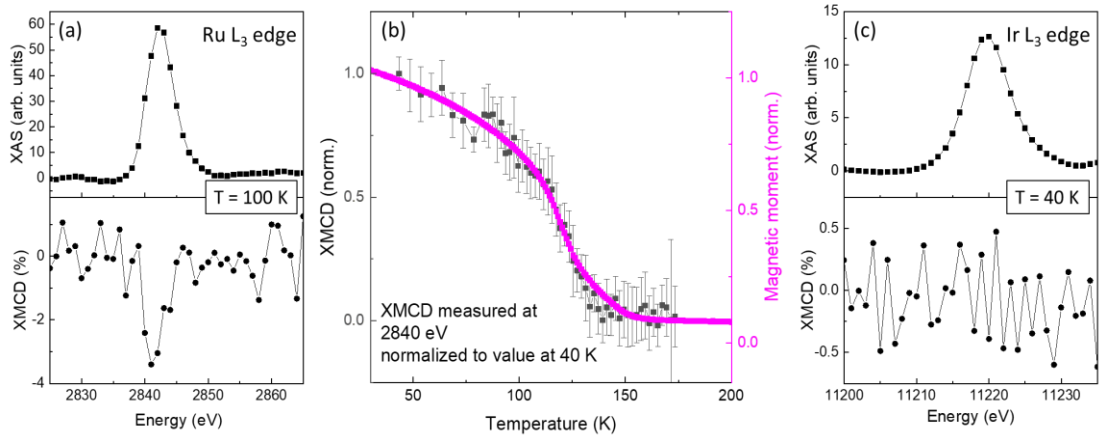

Figure 4.6: (a) X-ray absorption spectroscopy (XAS) and XMCD around the Ruthenium L_3 edge at 100 K. The XMCD was normalized to the XAS maximum. (b) Temperature dependence of the (normalized) Ru XMCD at 2840 eV after field cooling in 130 mT (black symbols). The XMCD was normalized to the max. value at 40 K for better comparison with the normalized m(T) curve determined by SQUID magnetometry. (c) XAS and XMCD around the Iridium L_3 edge at 40 K. The XMCD was normalized to the step edge of the XAS.

structures that are more relaxed towards the bulk $SrRuO_3$ structure, approaching the OOR values of the bulk, and thus have larger Curie temperature.

Two ferromagnetic transition temperatures were reported recently for $(SrRuO_3)n/(SrIrO_3)n$ superlattices with ultrathin individual layers ($n \leqslant 3$)[43]. The high temperature transition, also occurring at 140 K as for our samples, was attributed to the interesting possibility that the ultrathin $SrIrO_3$ layers undergo a canting antiferromagnetic transition. This transition vanished for the superlattices with thicker layers, $n \geqslant 4$. As stressed in this reference, no x-ray circular magnetic dichroism spectroscopy (XCMD) measurements at the Ru and Ir edges have been performed yet to test this proposal. There are however XMCD studies of $LaMnO_3/SrIrO_3$ superlattices, which demonstrate the formation of interfacial Ir-Mn molecular orbitals and ferromagnetic order of the Ir magnetic moments[44].

To figure out whether the ultrathin $SrIrO_3$ layers of our multilayer show the mentioned canting antiferromagnetic transition, the XMCD measurement was performed first. The energy scans at the Ruthenium L_3 edge, shown in figure 4.6(a), were performed. The (normalized) XMCD signal at the energy as a function of temperature was shown in see figure 4.6(b), which is very similar to the (normalized) m(T) curve measured by SQUID magnetometry (drawn in violet). Thus, we checked that the structure observed in the dm/dT curve is most likely related to the $SrRuO_3$ layers. Then, energy scans around the Iridium L_3 edge were performed to investigate whether the Ir ions become magnetically ordered due to the interfacing with ferromagnetic $SrRuO_3$ within the heterostructure. The absorption edge of the Iridium was clearly observed in the XAS scan (see figure 4.6(c), while no XMCD signal could be measured (above a signal strength of 0.5 %, cp. lower plot in figure 4.6(c)). Error bars are nevertheless important, and more statistics would be required. Based on the

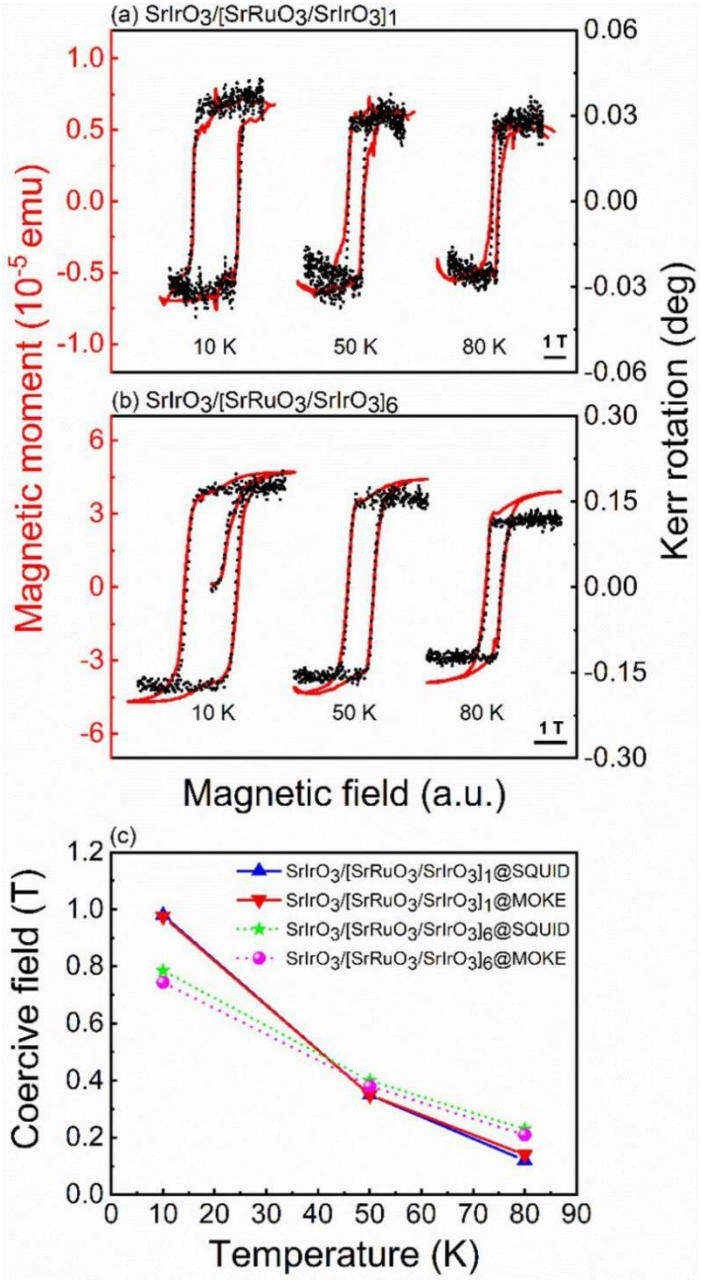

Figure 4.7: Magnetic moment hysteresis loops (measured by SQUID magnetometry, red loops) and MOKE rotation angle loops for samples (a) $SrIrO_3/[SrRuO_3/SrIrO_3]_1$ and (b) $SrIrO_3/[SrRuO_3/SrIrO_3]_6$, measured in perpendicular magnetic field. (c) Comparison of the coercive fields of these two samples at different temperatures, as obtained from the SQUID and MOKE hysteresis loops. The lines are guides for the eye.

current XMCD results, no conclusive statements can be made regarding the magnetic order of the Ir ions.

The comparison of the out-of-plane total magnetic moment hysteresis loops, measured with the SQUID magnetometer, and the MOKE rotation angle loops of the samples with m = 1 and m = 6 is shown in figure 4.7(a) and figure 4.7(b), respectively. We plotted the SQUID and MOKE hysteresis loops of the same sample at several

temperatures (10 K, 50 K, 80 K). The coercive fields determined by SQUID and MOKE measurements are almost identical. The SQUID and MOKE loops of both samples are in very good agreement except for the regions of saturated magnetization, for relatively high fields. This discrepancy stems from the corrections that had to be applied to both type of loops: the loops are affected by different contributions either from the diamagnetic substrate and ferromagnetic impurities for SQUID loops or from the cryostat window in the case of the MOKE loops. The temperature dependence of the coercive field, extracted from loops measured by SQUID and MOKE, is compared for the two samples in figure 4.7(c). The magnitude of coercive fields and their temperature dependence is in good agreement with the results of previous work[36].

4.4.3 Anomalous Hall resistance and MOKE hysteresis loops

For the particular samples under study, the measured total Hall voltage has a contribution from the ordinary Hall effect and a contribution from the AHE, at temperatures below the Curie temperature of the $SrRuO_3$ layers. The total Hall voltage V_{yx} was measured in van der Pauw configuration (as shown in the schematic inset of figure 4.8(a)).

We define the transverse Hall resistance R_{yx} as the ratio of the Hall voltage and the excitation current I: $R_{yx} = V_{yx}/I$. For the $SrIrO_3/[SrRuO_3/SrIrO_3]_m$ multilayers, the metallic $SrRuO_3$ layers are magnetically decoupled[36] and are electrically connected in parallel. The $SrRuO_3$ layers have very similar resistances, because they have nominally the same thickness and similar interfaces[45]. The contribution of the ordinary Hall effect to the measured Hall voltage V_{yx} was subtracted from all the Hall loops shown in the paper: We assumed that in the high magnetic field range, when the magnetization of the sample gets saturated, the only field dependence comes from the linear contribution of the ordinary Hall effect. Therefore, in the following R_{yx} reflects the AHE of the samples and we refer to it as the anomalous Hall resistance in discussing the data presented in figures 4.8-4.12.

The hysteresis loops of R_{yx} at fixed temperature in the range 10–110 K/120 K of the $SrIrO_3/[SrRuO_3/SrIrO_3]_1$ and $SrIrO_3/[SrRuO_3/SrIrO_3]_6$ samples are plotted in figure 4.8(a) and figure 4.8(b), respectively. We note that the anomalous Hall resistance of these two samples exhibits a sign change from negative (at low temperatures) to positive around 86 K. This change of sign is typical for $SrRuO_3$ epitaxial films as well as single crystals[46], consistent with previous experimental data and theoretical predictions[11,47-52]. This peculiar sign change, from negative to positive as the temperature increases, comes from the change of the sign of the intrinsic anomalous Hall conductivity. The latter is the result of the presence of Weyl-like nodes, acting as magnetic monopoles, in the electronic band structure of $SrRuO_3$, combined with changes in the band structure as a function of the magnetization (and thus of the temperature). Although the existence of magnetic monopoles in $SrRuO_3$ is not experimentally unambiguously proved yet, the three-dimensional bulk $SrRuO_3$ has been considered as a system for which a large intrinsic AHE driven by topological band

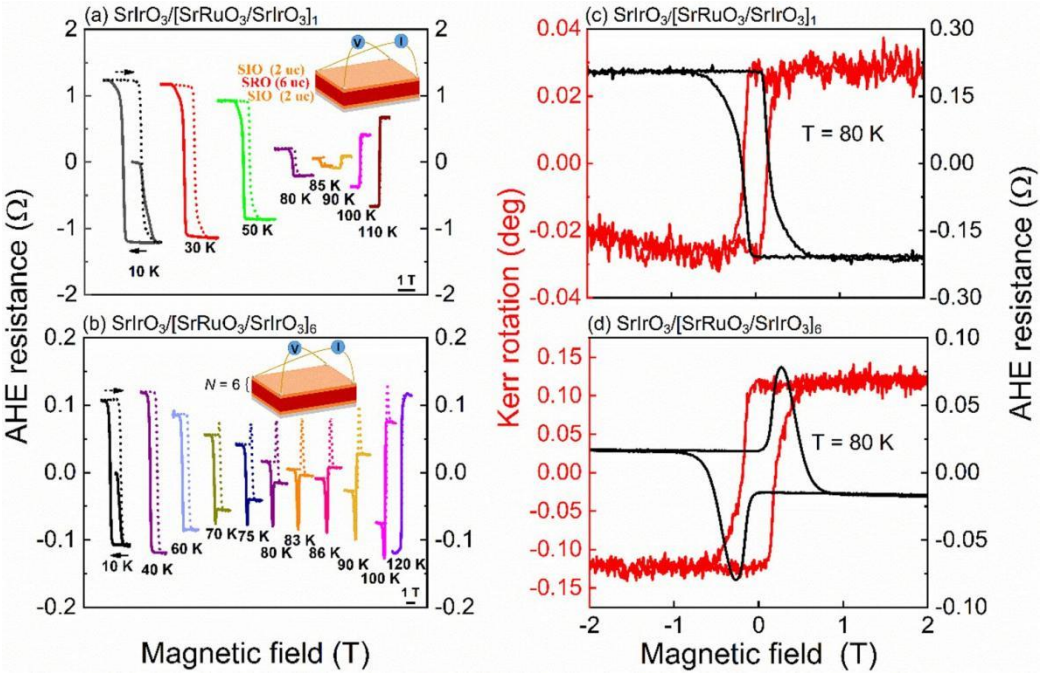

Figure 4.8: Summary of the anomalous Hall effect (AHE) resistance *Ryx* loops of the $SrIrO_3/[SrRuO_3/SrIrO_3]_m$ (m = 1, 6) samples, as a function of temperature: (a) for $SrIrO_3/[SrRuO_3/SrIrO_3]_1$ and (b) for $SrIrO_3/[SrRuO_3/SrIrO_3]_6$. In (c) and (d) the anomalous Hall resistance loops (black) and the MOKE rotation angle loops (red) measured at 80 K for sample $SrIrO_3/[SrRuO_3/SrIrO_3]_1$ and $SrIrO_3/[SrRuO_3/SrIrO_3]_6$, respectively, are compared.

structure can be observed[46]. As the energies of nodal points and lines are different, when the Berry curvatures from them have opposite signs, the magnitude, and the sign of intrinsic AHE conductivity can be tuned by changing the position of the Fermi level[50,51,53].

The most important observation is that the trilayer samples do not exhibit any hump-like anomalies in the as measured Hall effect loops, as this is expected for symmetric interfaces. In contrast, our asymmetric bilayers with only one $SrRuO_3/SrIrO_3$ interface of the same structural quality as for the trilayers, as studied in our previous work[35,49] (see also comparative AHE loops data for a bilayer in figure 4.12), do show hump-like features in the vicinity of the temperature at which AHE constant changes sign. Besides, the AHE resistance loops of the multilayer sample (m = 6) do show hump-like features within a broad temperature range from 70–110 K [see figure 4.4(b)]. These features of Hall resistance loops are peculiar, if compared with the corresponding magnetization/Kerr rotation angle loops measured at the same temperature. For the multilayer, the AHE and MOKE loops at the temperatures where the hump features occur are strikingly different, as obvious in the selected plots in figure 4.4(d). This indicates that the AHE resistance loops of the multilayer do not directly scale with the magnetization loops, as conventionally expected if the AHE constant was the same, in terms of magnitude and temperature dependence, for all six $SrRuO_3$ layers of the multilayer.

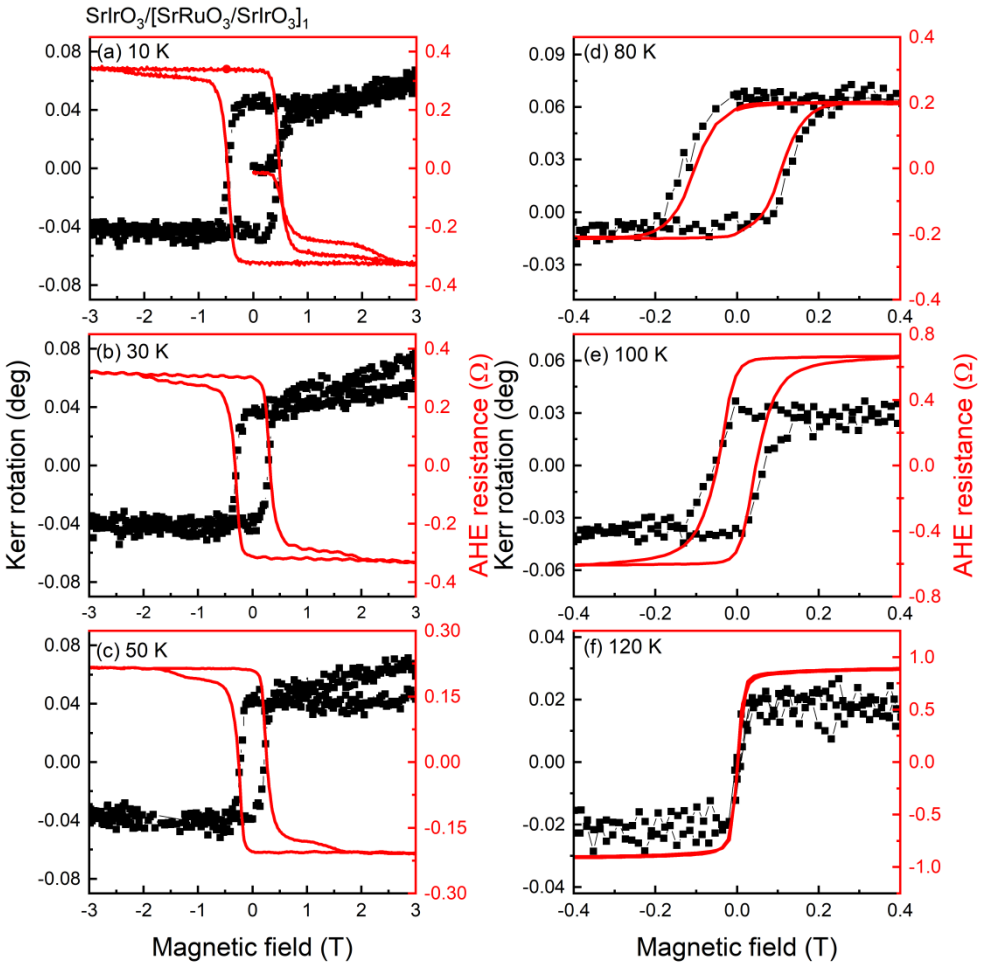

Figure 4.9: Anomalous Hall effect (AHE) resistance loops and Kerr rotation angle loops for the second $SrIrO_3/[SrRuO_3/SrIrO_3]_1$ trilayer, at different temperatures from 10 K to 120 K: AHE resistance loops (red line) and the MOKE loops (black line with solid square dots). The AHE changes sign to positive above 60-70 K.

To cross check the AHE and MOKE loops data of $SrIrO_3/[SrRuO_3/SrIrO_3]_1$, we grew a second trilayer sample $SrIrO_3/[SrRuO_3/SrIrO_3]_1$ and a multilayer sample with m = 3 $SrIrO_3/[SrRuO_3/SrIrO_3]_3$, in our PLD system at University of Cologne. The MOKE and Hall effect loops of the samples are summarized in figure 4.9 and in figure 4.10, respectively. The Kerr rotation angle and AHE resistance measurements were performed simultaneously and both type of loops shows similar coercive fields at all temperatures. In the ferromagnetic phase of the $SrRuO_3$ layer, as the temperature increases, the AHE resistance changes sign, from negative to positive, somewhat below 80 K. There are no hump-like features in the AHE resistance loops also for this second $SrIrO_3/[SrRuO_3/SrIrO_3]_1$.

The data of AHE resistance and MOKE loop measurement at different temperatures for the trilayer made in our PLD system and its reference trilayer sample

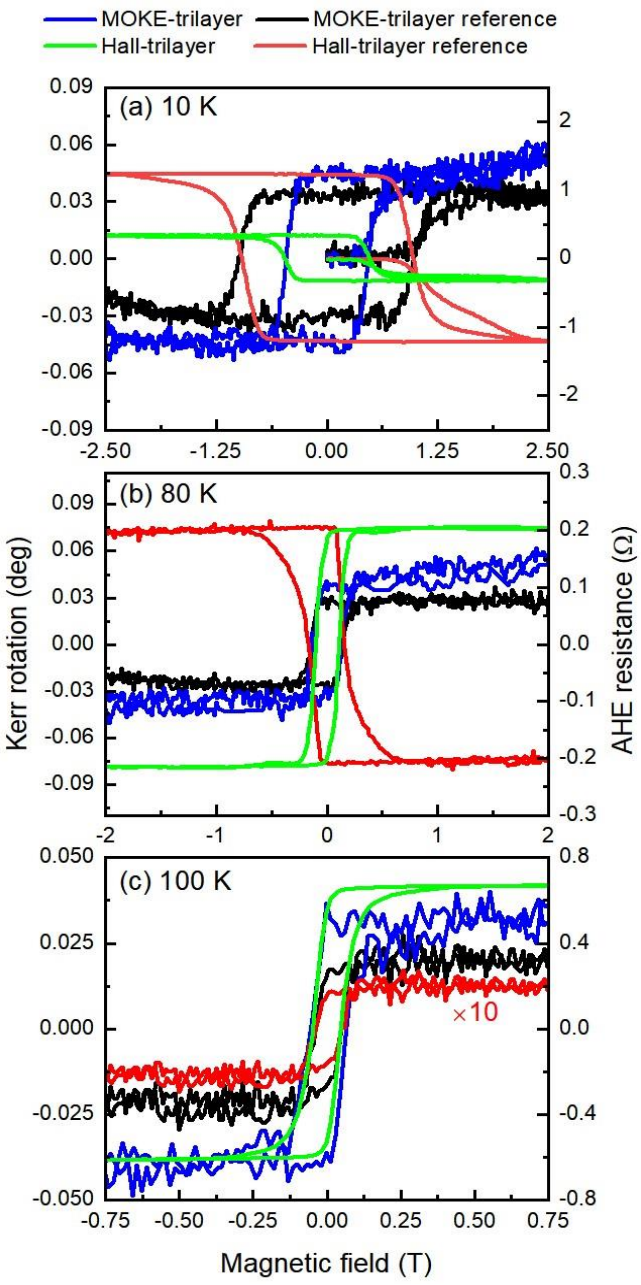

Figure 4.10: Comparison of AHE and MOKE loops for the two $SrIrO_3/[SrRuO_3/SrIrO_3]_1$ trilayers, made in different PLD chambers, with differing PLD conditions. We compare the loops at different temperatures, capturing the change of sign of AHE for both samples: (a) 10 K, (b) 80 K, (c) 100 K. AHE resistance loops are plotted in red and green and the Kerr rotation angle black and blue. The magnitude of Hall loop for $SrIrO_3/[SrRuO_3/SrIrO_3]_1$ at 100 K was increased tenfold for better comparison.

are summarized in figure 4.10. It should be noted that we obtained these data by simultaneous measurement of MOKE and Hall effect resistance loops in our combined MOKE-Hall setup, with the sample in the same cryostat. In general, for each sample, the AHE loops scale with the MOKE loops fairly well. The most striking differences between the two samples are the magnitude of the coercive fields and the temperature dependence of the AHE resistance. The second trilayer has a much smaller coercive

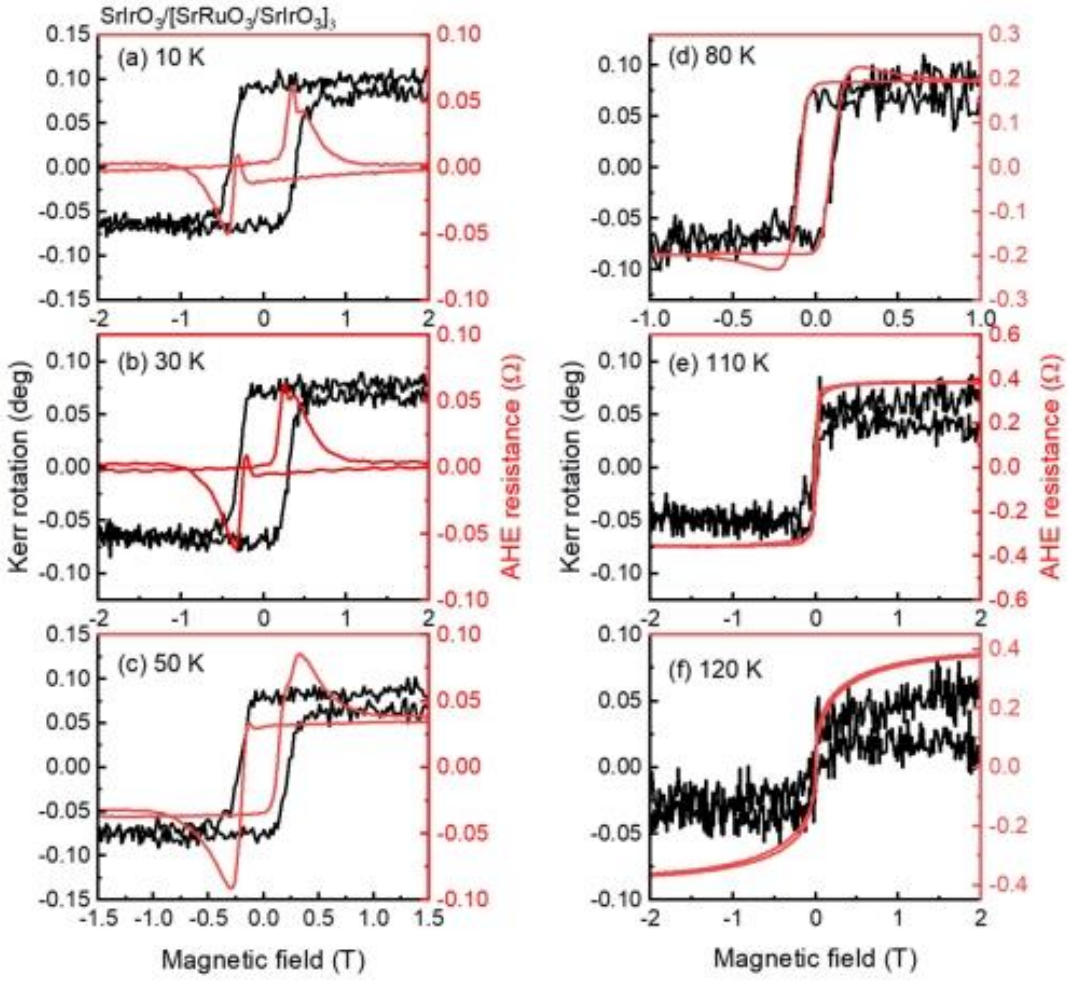

Figure 4.11: AHE resistance loops and Kerr rotation angle loops for the multilayer $SrIrO_3/[SrRuO_3/SrIrO_3]_3$ (m = 3), at different temperatures from 10 K to 120 K: AHE resistance loops (red line) and the MOKE loops (black line).

field at low temperatures, see for instance the loops measured at 10 K: the coercive field of the reference layer is almost twice as large. The AHE changes sign well below 80 K for the second trilayer, while the reference trilayer changes the sign of the AHE from negative to positive at 86 K. We grew the second trilayer with the intention to obtain a comparable sample, i.e., with 2 uc thick $SrIrO_3$ and 6 uc thick $SrRuO_3$ layers. However, the second PLD chamber has major differences (such as target-to-substrate distance, perpendicular geometry, laser fluence measurement), which made it not possible to have the same PLD parameters for the growth. Thus, we stress how important the growth conditions are for the magnetic and electronic properties of $SrRuO_3/SrIrO_3$ oxide thin films. However, the most important similarity between the two trilayer samples is that both do not show any hump-like anomalies of the AHE resistance loops, demonstrating a consistent behavior for the expected symmetric trilayers.

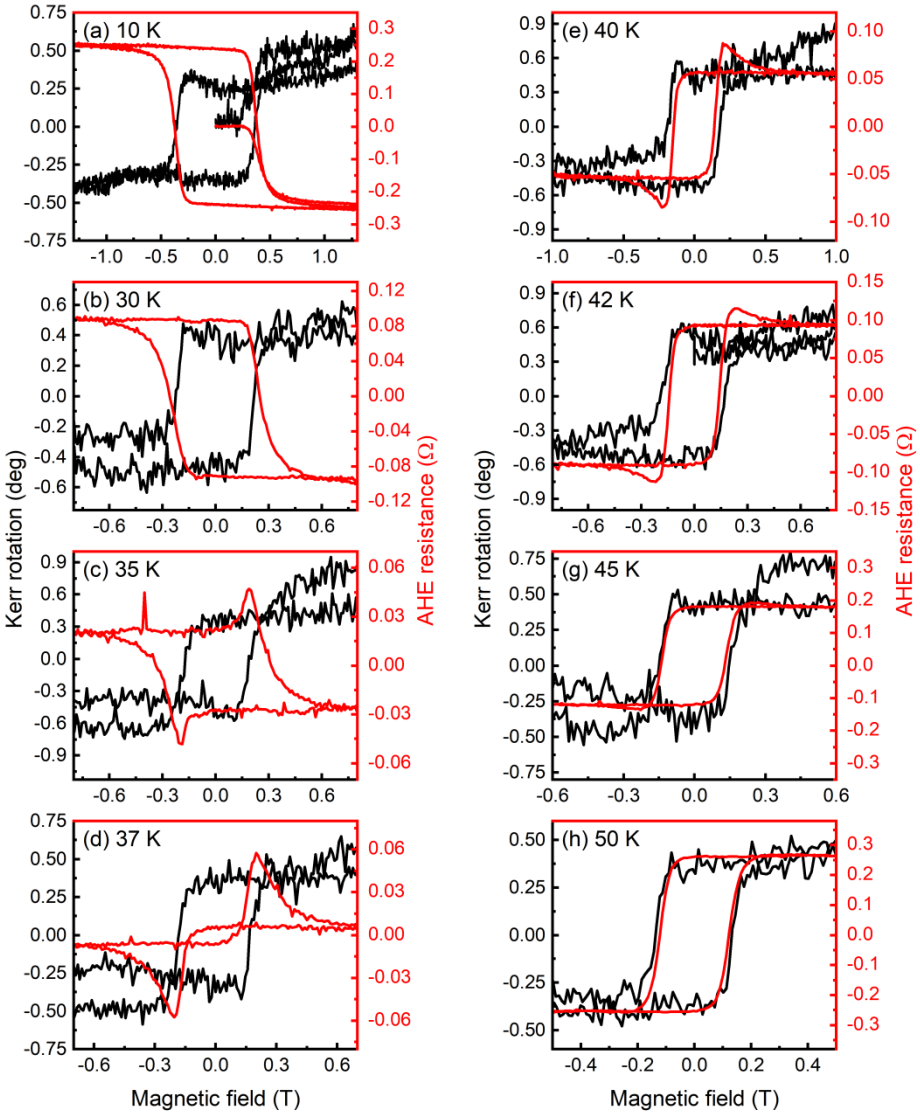

Figure 4.12: AHE resistance loops and Kerr rotation angle loops for the of $SrRuO_3/SrIrO_3$ bilayer, acquired simultaneously at different temperatures from 10 K to 50 K (around the change of sign of the AHE constant): AHE resistance loops (red line) and the MOKE loops (black line).

Besides, we grew another reference sample $SrIrO_3/[SrRuO_3/SrIrO_3]_3$, with the same PLD parameters as for the second trilayer $SrIrO_3/[SrRuO_3/SrIrO_3]_1$. For the multilayer $SrIrO_3/[SrRuO_3/SrIrO_3]_3$ (see figure 4.11), the MOKE and Hall loops show striking differences in the temperature range 10 K - 80 K. For the MOKE measurement, the open MOKE loops are obtained up to about 110 K, indicating that the Curie temperature is at least 110 K. For the AHE resistance measurement, the clear humps exist from the lowest temperature we can measure at, 10 K, to about 80 K. The evolution of the sign of anomalous Hall constant is quite different from the previous sample $SrIrO_3/[SrRuO_3/SrIrO_3]_6$ and bilayer sample in J. Matsuno *et al.* paper[11]. The sign of the total anomalous Hall resistance (voltage) of the sample $SrIrO_3/[SrRuO_3/SrIrO_3]_3$ is positive down to about 10 K. The multiple peaks of the AHE loops at 10 K and 30 K

may be explained, if the global loop is decomposed in three independent loops generated by the three $SrRuO_3$ layers. The three separated magnetic layers possess slightly different magnetic and AHE properties[38].

In figure 4.12, we summarize the temperature dependence of the AHE resistance loops of the $SrRuO_3/SrIrO_3$ bilayer sample, from 10 K to 50 K. At a temperature around 37 K, the AHE resistance loops change the sign from negative to positive on increasing the temperature. The AHE loops from 35 K to 45 K do show hump-like anomalies, as we also observed for other bilayer samples and reported in our previous publication[35] and, for example, in Ref. [11], and as observed here for the symmetric multilayers (m= 3 and m= 6).

Our symmetric multilayers, $SrIrO_3/[SrRuO_3/SrIrO_3]_6$ and $SrIrO_3/[SrRuO_3/SrIrO_3]_3$, had a geometry that minimizes a net interfacial DMI. The lack of net DMI is a strong indication that other mechanisms than skyrmions and their THE have to be considered for the hump anomalies of the AHE hysteresis loops. A more plausible explanation is that the individual $SrRuO_3$ layers of the multilayer $SrIrO_3/[SrRuO_3/SrIrO_3]_6$ have slightly different magnetic properties (i.e., saturation magnetization, coercive field, T_c), as a result of chemical and structural differences among each other (originating from slight layer thickness variation, different degree of intermixing of Ir on the Ru site, and oxygen octahedron deformations). These differences, though probably minute, are of great importance for the temperature dependence and the magnitude of the intrinsic anomalous Hall resistivity of each layer. Hence, the individual ferromagnetic $SrRuO_3$ layers generate several independent magnetotransport channels leading to the observed hump anomalies of the AHE loops. As proposed in several papers[28,33,53-55] and our previous reports[32,35,38], the hump-like anomalies of the AHE hysteresis loops in $SrRuO_3$-based heterostructure can be well explained by a model of several independent magnetic channels, with distinct coercive fields and different temperatures at which the intrinsic AHE conductivity changes sign.

4.5 Summary

In epitaxial asymmetric $SrRuO_3/SrIrO_3$ bilayers a strong interfacial DMI was proposed to emerge and be the driving force for the formation of skyrmions. These skyrmions would result in a THE, whose manifestation was considered to be spotted as hump-like features, developing while the magnetization of the $SrRuO_3$ layer reversed between saturated states. We studied here heterostructures in which an ultrathin ferromagnetic $SrRuO_3$ layer was sandwiched between $SrIrO_3$ layers. Principally, this geometry disfavors the occurrence of a net interfacial DMI, and thus the formation of skyrmions would be exceptional. $SrIrO_3/SrRuO_3/SrIrO_3$ trilayers did not have hump anomalies of the Hall resistance loops. However, the Hall resistance loops of multilayers, in which the trilayer was stacked several times, did exhibit the hump-like structures, similar to the asymmetric $SrRuO_3/SrIrO_3$ bilayers. The magnetization as a function of temperature indicated that the multilayers had a spread of the Curie temperatures, hinting to

differences in the magnetic properties of the individual $SrRuO_3$ layers. The origin of the Hall effect anomalies likely stems from unavoidable structural differences between the individual $SrRuO_3$ layers stacked in epitaxial multilayers. The minute structural differences (oxygen octahedra rotation angles, bond lengths) of the individual ruthenate layers result in inhomogeneous magnetic and electrical properties across the multilayer. It is possible that the individual $SrRuO_3$ layers generate several independent magnetotransport channels leading to the observed anomalous features of the Hall effect loops. The possibility that the hump anomalies relate to the skyrmion formation cannot be ruled out. However, our data strongly support the interpretation in terms of multiple magnetotransport channels present in multilayers. We stress that to the best of our knowledge, there is no experimental evidence of the existence of DMI at the epitaxial interface of the ferromagnetic $SrRuO_3$ and the large spin-orbit coupling $SrIrO_3$ and the interfacial DMI is still only at the level of speculative assumption. Experiments of Brillouin light scattering (BLS)[56,57], which are routinely employed for determining the strength and sign of interfacial DMI, but chiefly for systems that are magnetically ordered at room temperature, are rarely performed at low temperatures, such as needed for $SrRuO_3/SrIrO_3$. No BLS investigations have been reported so far on epitaxial all-oxide heterostructures. Focused studies must be dedicated to the essential aspect of DMI determination, from both theoretical and experimental viewpoints, starting with understanding the microscopic mechanism of DMI at epitaxial all-oxide interfaces.

4.6 References

[1] N. S. Kiselev, A. N. Bogdanov, R. Schäfer, and U. K. Rößler, Journal of Physics D: Applied Physics **44** (39), 392001 (2011).

[2] A. Soumyanarayanan, M. Raju, A. L. G. Oyarce, A. K. C. Tan, Mi-Young Im, A. P Petrović, P. Ho, K. H. Khoo, M. Tran, C. K. Gan, F. Ernult, and C. Panagopoulos, Nature Materials **16** (9), 898 (2017).

[3] S. Woo, K. Litzius, B. Krüger, M.-Y. Im, L. Caretta, K. Richter, M. Mann, A. Krone, R. M. Reeve, M. Weigand, P. Agrawal, I. Lemesh, M.-A. Mawass, P. Fischer, M. Kläui, and G. S. D. Beach, Nature Materials **15** (5), 501 (2016).

[4] S. Das, Y. L. Tang, Z. Hong, M. A. P. Gonçalves, M. R. McCarter, C. Klewe, K. X. Nguyen, F. Gómez-Ortiz, P. Shafer, E. Arenholz, V. A. Stoica, S. L. Hsu, B. Wang, C. Ophus, J. F. Liu, C. T. Nelson, S. Saremi, B. Prasad, A. B. Mei, D. G. Schlom, J. Íñiguez, P. García-Fernández, D. A. Muller, L. Q. Chen, J. Junquera, L. W. Martin, and R. Ramesh, Nature **568** (7752), 368 (2019).

[5] X. Z. Yu, N. Kanazawa, W. Z. Zhang, T. Nagai, T. Hara, K. Kimoto, Y. Matsui, Y. Onose, and Y. Tokura, Nature Communications **3** (1), 988 (2012).

[6] A. Fert, V. Cros, and J. Sampaio, Nat Nanotechnol **8** (3), 152 (2013).

[7] J. Iwasaki, M. Mochizuki, and N. Nagaosa, Nature Communications **4** (1), 1463 (2013).

[8] C. Reichhardt, D. Ray, and C. J Olson Reichhardt, Physical Review Letters **114** (21), 217202 (2015).

[9] W. Jiang, P. Upadhyaya, W. Zhang, G. Yu, M. B. Jungfleisch, Y. F. Frank, E. P. John, Y. Tserkovnyak, L. W. Kang, O. Heinonen, G. E. te V. Suzanne, and A. Hoffmann, Science **349** (6245), 283 (2015).

[10] W. Jiang, G.Chen, K. Liu, J. Zang, S. G. E. te Velthuis, and A. Hoffmann, Physics Reports **704**, 1 (2017).

[11] J. Matsuno, N. Ogawa, K. Yasuda, F. Kagawa, W. Koshibae, N. Nagaosa, Y. Tokura, and M. Kawasaki, Science Advances **2** (7), e1600304.

[12] K.-Y. Meng, A. S. Ahmed, M. Baćani, A.-O. Mandru, X. Zhao, N. Bagués, B. D. Esser, J. Flores, D. W. McComb, H. J. Hug, and F. Yang, Nano Letters **19** (5), 3169 (2019).

[13] A. Fert, N. Reyren, and V. Cros, Nature Reviews Materials **2** (7), 17031 (2017).

[14] X. Z. Yu, J. P. DeGrave, Y. Hara, T.Hara, S. Jin, and Y. Tokura, Nano Letters **13** (8), 3755 (2013).

[15] S. Heinze, K. von Bergmann, M. Menzel, J. Brede, A. Kubetzka, R. Wiesendanger, G. Bihlmayer, and S. Blügel, Nature Physics **7** (9), 713 (2011).

[16] O. Boulle, J. Vogel, H. Yang, S. Pizzini, D. de S. Chaves, A. Locatelli, T. O. Menteş, A. Sala, L. D. Buda-Prejbeanu, O. Klein, M. Belmeguenai, Y. Roussigné, A. Stashkevich, S. Mourad Chérif, L. Aballe, M. Foerster, M. Chshiev, S. Auffret, I. M. Miron, and G. Gaudin, Nat Nanotechnol **11** (5), 449 (2016).

[17] G. Chen, A. Mascaraque, A. T. N'Diaye, and A. K. Schmid, Applied Physics Letters **106** (24), 242404 (2015).

[18] S. Mühlbauer, B. Binz, F. Jonietz, C. Pfleiderer, A. Rosch, A. Neubauer, R. Georgii, and P. Böni, Science **323** (5916), 915 (2009).

[19] Y. Yamasaki, D. Morikawa, T. Honda, H. Nakao, Y. Murakami, N. Kanazawa, M. Kawasaki, T. Arima, and Y. Tokura, Phys Rev B **92** (22), 220421 (2015).

[20] H. Huang, S.-J. Lee, B. Kim, B. Sohn, C. Kim, C.-C. Kao, and J.-S. Lee, ACS Applied Materials & Interfaces **12** (33), 37757 (2020).

[21] P. Zhang, A. Das, E. Barts, M. Azhar, L. Si, K. Held, M. Mostovoy, and T. Banerjee, Physical Review Research **2** (3), 032026 (2020).

[22] C.-A. Wang, C.-H. Chang, A. Herklotz, C. Chen, F. Ganss, U. Kentsch, D. Chen, X. Gao, Y.-J. Zeng, O. Hellwig, M. Helm, S. Gemming, Y.-H. Chu, and S. Zhou, Advanced Electronic Materials **6** (6), 2000184 (2020).

[23] B. Pang, L. Zhang, Y. B. Chen, J. Zhou, S. Yao, S. Zhang, and Y. Chen, ACS Applied Materials & Interfaces **9** (3), 3201 (2017).

[24] L. Wang, Q. Feng, Y. Kim, R. Kim, K. H. Lee, S. D. Pollard, Y. J. Shin, H. Zhou, W. Peng, D. Lee, W. Meng, H. Yang, J. H.. Han, M. Kim, Q. Lu, and T. W. Noh, Nature Materials **17** (12), 1087 (2018).

[25] Y. Ohuchi, J. Matsuno, N. Ogawa, Y. Kozuka, M. Uchida, Y. Tokura, and M. Kawasaki, Nature Communications **9** (1), 213 (2018).

[26] Y. Gu, Y.-W. Wei, K. Xu, H. Zhang, F.Wang, F. Li, M. Shahrukh Saleem, C.-Z. Chang, J. Sun, C. Song, J. Feng, X. Zhong, W. Liu, Z. Zhang, J. Zhu, and F.Pan, Journal of Physics D: Applied Physics **52** (40), 404001 (2019).

[27] Q. Qin, L. Liu, W. Lin, X. Shu, Q. Xie, Z. Lim, C. Li, S. He, G. M. Chow, and J. Chen, Advanced Materials **31** (8), 1807008 (2019).

[28] D. Kan and Y.Shimakawa, physica status solidi (b) **255** (9), 1800175 (2018).

[29] L. Wang, Q. Feng, H. G. Lee, E. K. Ko, Q. Lu, and T. W. Noh, Nano Letters **20** (4), 2468 (2020).

[30] P.-C. Wu, H. Song, Y. Yuan, B. Feng, Y. Ikuhara, R. Huang, P. Yu, C.-G. Duan, and Y.-H. Chu, Physical Review Materials **4** (1), 014401 (2020).

[31] G. Kimbell, P. M. Sass, B. Woltjes, E. K. Ko, T. W. Noh, W. Wu, and J. W. A. Robinson, Physical Review Materials **4** (5), 054414 (2020).

[32] M. Ziese, L. Jin, and I. Lindfors-Vrejoiu, Journal of Physics: Materials **2** (3), 034008 (2019).

[33] D. J. Groenendijk, C. Autieri, T. C. van Thiel, W. Brzezicki, J. R. Hortensius, D. Afanasiev, N. Gauquelin, P. Barone, K. H. W. van den Bos, S. van Aert, J. Verbeeck, A. Filippetti, S. Picozzi, M. Cuoco, and A. D. Caviglia, Physical Review Research **2** (2), 023404 (2020).

[34] N. Mohanta, E. Dagotto, and S. Okamoto, Phys Rev B **100** (6), 064429 (2019).

[35] L. Wysocki, J.Schöpf, M. Ziese, L. Yang, A. Kovács, L.Jin, R. B. Versteeg, A. Bliesener, F. Gunkel, L. Kornblum, R. Dittmann, P. H. M. van Loosdrecht, and I. Lindfors-Vrejoiu, ACS Omega **5** (11), 5824 (2020).

[36] L. Wysocki, R. Mirzaaghayev, M. Ziese, L. Yang, J. Schöpf, R. B. Versteeg, A. Bliesener, J. Engelmayer, A. Kovács, L. Jin, F. Gunkel, R. Dittmann, P. H. M.

van Loosdrecht, and I. Lindfors-Vrejoiu, Applied Physics Letters **113** (19), 192402 (2018).

37 L. Bergmann, P. Düring, S. Agrestini, A. Efimenko, S. C. Liao, Z. Hu, P. Gargiani, C. J. Choi, H. Baik, D. S. Park, K. Dörr, and A. D. Rata, AIP Advances **10** (3), 035132 (2020).

38 L. Wysocki, L. Yang, F. Gunkel, R. Dittmann, P. H. M. van Loosdrecht, and I. Lindfors-Vrejoiu, Physical Review Materials **4** (5), 054402 (2020).

39 K. Samanta, M. Ležaić, M.n Merte, F. Freimuth, S. Blügel, and Y. Mokrousov, Journal of Applied Physics **127** (21), 213904 (2020).

40 J. Choi, C. B. Eom, G. Rijnders, H. Rogalla, and D. H. A. Blank, Applied Physics Letters **79** (10), 1447 (2001).

41 K. Momma and F. Izumi, J Appl Crystallogr **44** (6), 1272 (2011).

42 Y. J. Chang, C. H. Kim, S. H. Phark, Y. S. Kim, J. Yu, and T. W. Noh, Physical Review Letters **103** (5), 057201 (2009).

43 Z. Zeng, J. Feng, X. Zheng, C. Wang, J. Liu, Z. Lu, F.-X. Jiang, X.-H. Xu, Z. Wang, and R.-W. Li, Applied Physics Letters **116** (14), 142401 (2020).

44 Y. Zhang, Y. Z. Luo, L. Wu, M. Suzuki, Q. Zhang, Y. Hirata, K. Yamagami, K. Takubo, K. Ikeda, K. Yamamoto, A. Yasui, N. Kawamura, C. Lin, K. Koshiishi, X. Liu, J. Zhang, Y. Hotta, X. R. Wang, A. Fujimori, Y. Lin, C. Nan, L. Shen, and H. Wadati, Physical Review Research **2** (3), 033496 (2020).

45 S. L. Zhang, Y. Liu, L. J. Collins-McIntyre, T. Hesjedal, J. Y. Zhang, S. G. Wang, and G. H. Yu, Scientific Reports **3** (1), 2087 (2013).

46 Z. Fang, N. Nagaosa, S. T. Kei, A. Asamitsu, R. Mathieu, T. Ogasawara, H. Yamada, M. Kawasaki, Y. Tokura, and K. Terakura, Science **302** (5642), 92 (2003).

47 N. Haham, Y. Shperber, M. Schultz, N. Naftalis, E. Shimshoni, J. W. Reiner, and L. Klein, Phys Rev B **84** (17), 174439 (2011).

48 I. Lindfors-Vrejoiu and M.l Ziese, physica status solidi (b) **254** (5), 1600556 (2017).

49 G. Malsch, D. Ivaneyko, P. Milde, L. Wysocki, L. Yang, P. H. M. van Loosdrecht, I. Lindfors-Vrejoiu, and Lukas M. Eng, ACS Applied Nano Materials **3** (2), 1182 (2020).

50 X. Wang, D.Vanderbilt, J. R. Yates, and I. Souza, Phys Rev B **76** (19), 195109 (2007).

51 Y. Chen, D. L. Bergman, and A. A. Burkov, Phys Rev B **88** (12), 125110 (2013).

52 D.Vanderbilt, I. Souza, and F. D. M. Haldane, Phys Rev B **89** (11), 117101 (2014).

53 B. Sohn, E. Lee, S. Y. Park, W. Kyung, J. Hwang, J. D. Denlinger, M.o Kim, D. Kim, B. Kim, H. Ryu, S. Huh, J. S. Oh, J. K.Jung, D. Oh, Y. Kim, M. Han, T.W. Noh, B.-J. Yang, and C. Kim, Nature Materials **20** (12), 1643 (2021).

54 A. Gerber, Phys Rev B **98** (21), 214440 (2018).

55 D. Kan, T. Moriyama, K. Kobayashi, and Y. Shimakawa, Phys Rev B **98** (18), 180408 (2018).

[56] X. Ma, G. Yu, C.Tang, X.Li, C. He, J. Shi, K. L. Wang, and X. Li, Physical Review Letters **120** (15), 157204 (2018).

[57] M. Belmeguenai, M. S. Gabor, Y. Roussigné, T. Petrisor, R. B. Mos, A. Stashkevich, S. M. Chérif, and C. Tiusan, Phys Rev B **97** (5), 054425 (2018).

Chapter 5 Enhancing the ferromagnetic interlayer coupling between epitaxial $SrRuO_3$ layers

Contents

Lin Yang,[1] Lei Jin,[2] Lena Wysocki,[1] Jörg Schöpf,[1] Daniel Jansen,[1] Brajagopal Das,[3] Lior Kornblum,[3] Paul H. M. van Loosdrecht,[1] and Ionela Lindfors-Vrejoiu[1]

[1]University of Cologne, Institute of Physics II, 50937 Cologne, Germany
[2]Ernst Ruska-Centre for Microscopy and Spectroscopy with Electrons, Forschungszentrum Jülich GmbH, 52425 Jülich, Germany
[3]Andrew & Erna Viterbi Department of Electrical Engineering, Technion Israel Institute of Technology, 3200003 Haifa, Israel

PHYSICAL REVIEW B 104, 064444 (2021) ©2021 American Physical Society
Doi：https://doi.org/10.1103/PhysRevB.104.064444

Contributions to this publication:

The main contribution to the publication comes from Lin Yang, Ionela Lindfors-Vrejoiu, and Paul H. M. van Loosdrecht. The contributions from the co-authors and other contributors are as below:

1) Lei Jin carried out the scanning transmission electron microscopy measurement and provided me with the initial data analysis
2) Ionela Lindfors-vrejoiu made all the samples under study.
3) Lena Wysocki assisted me with the superconducting quantum interference device (SQUID) measurement and analyzed the data.
4) The magneto-optical Kerr effect (MOKE) and Hall measurements were made with the assistance of Jörg Schöpf.
5) Daniel Jansen performed part of the atomic force microscopy (AFM) measurement for me.
6) Brajagopal Das and Lior Kornblum recorded and analyzed the x-ray diffraction (XRD) data.
7) Yongjian Wang made the resistivity measurements of the $LaNiO_3$ bare films.
8) René Borowski and Sylvia de Waal etched the STO substrates at FZ Jülich, and Susanne Heijligen performed SQUID measurements.
9) All the participants joined in the discussion of data and reviewed the paper, and agreed to publish this work.

5.1 Abstract

Magnetic interlayer coupling is a critical ingredient in designing magnetic multilayers with functionalities that reach out to the realm of applications. In epitaxial ferromagnetic (FM) oxide multilayers, the magnetic interlayer coupling is, however, less studied, and its prediction is often a challenging task. Ultrathin FM $SrRuO_3$ epitaxial films with perpendicular magnetic anisotropy, interfaced with suitable oxides, may be susceptible to forming skyrmions. Hence, a strong FM interlayer coupling would be beneficial to achieve the uniform switching behavior of a $SrRuO_3$-based multilayer. Previous studies reported that the coupling of two $SrRuO_3$ layers separated by a non-FM oxide spacer is at best weakly FM, and the two FM layers switch at markedly different fields. We study the magnetic interlayer coupling between two FM $SrRuO_3$ layers separated by ultrathin $LaNiO_3$ in epitaxial heterostructures grown on $SrTiO_3$(100) single crystals. We found that FM $SrRuO_3$ layers separated by 2 monolayers (MLs) thick $LaNiO_3$ show weak FM interlayer coupling of about 106 $\mu J/m^2$ at 10 K. The coupling becomes strongly FM for four MLs thick (about 1.6 nm) $LaNiO_3$ spacers and the two $SrRuO_3$ layers reverse their magnetization at a common value of the perpendicular magnetic field. This is likely due to a transition of the $LaNiO_3$ spacer from insulating to metallic as its thickness increases.

5.2 Introduction

Ferromagnetic (FM) oxide thin films and multilayers, in contrast to the bare metallic FM multilayers based on Fe, Co, or Ni, have multiple tuning knobs to modify and control their physical properties. To name a few, these knobs can be the epitaxial strain imposed by the single crystalline substrate, the interactions at the coherent interfaces with dissimilar oxides, the structural modifications undergone to accommodate the mismatch of symmetry, all being often in conjunction with strong layer thickness dependence[1]. Often minute turns of the tuning knobs massively impact on the magnetic properties, such as the Curie temperature, the saturation magnetization, on the effective magnetic anisotropy and on the magneto- transport properties of the epitaxial layer. On one hand, this high sensitivity results in fascinating phenomena, such as magnetic frustration, 2D electron gases, and superconductivity[2]. On the other hand, it makes it difficult to predict their occurrence, and the development of the theoretical treatment is often not keeping up with their complexity. For instance, an exciting proposal was made in 2016 that at the epitaxial interface between FM ultrathin $SrRuO_3$ layers and the large spin-orbit coupling (SOC) semimetallic $SrIrO_3$, a large interfacial Dzyaloshinskii-Moriya interaction (DMI) would exist. An attractive consequence put forward was that Néel skyrmions so small as about 10 nm could form in the ultrathin $SrRuO_3$ layers[3]. Moreover, it was proposed that by applying a gate voltage across the $SrRuO_3$/$SrIrO_3$ bilayer, an electric field effect could be a convenient way to act on the skyrmions[4]. Stimulated by these proposals, we studied the magnetic and mangneto-transport properties of symmetric and asymmetric $SrRuO_3$/$SrIrO_3$

multilayers[5,6] and one aspect we addressed was the magnetic interlayer coupling[7,8]. We found that the FM $SrRuO_3$ layers are only very weakly coupled across the nonmagnetic ultrathin $SrIrO_3$ layers. The weak coupling is disadvantageous if the control of the magnetic domains is targeted. Here we report on a possible solution of how to make the magnetic interlayer coupling between two $SrRuO_3$ layers separated by a non-FM spacer strongly FM. For this purpose, we considered $LaNiO_3$, an oxide that usually does not exhibit FM ordering. The coupling between two $SrRuO_3$ layers is weakly FM for the 2 monolayers (MLs) thick $LaNiO_3$ spacer and strongly FM when the thickness of the $LaNiO_3$ spacer was increased to 4 MLs. For the latter case, the two $SrRuO_3$ layers reverse their magnetization at the same mag- netic field, independent of temperature. The change of the coupling from weak to strong has to do chiefly with changes in the transport properties of the $LaNiO_3$ spacer. Bulk $LaNiO_3$ is metallic, but ultrathin $LaNiO_3$ epitaxial layers exhibit a metal-insulator transition, which typically occurs when the layers become thinner than about 4 MLs[9]. The temperature at which the transition to insulating takes place depends on the particular details such as on what substrate the layers are grown (i.e., epitaxial and symmetry conditions) and on the type and amount of defects (off-stoichiometry, oxygen content, extended structural defects)[9,10]. Moreover, a possible transition to antiferromagnetic (AFM) order was reported for ultrathin $LaNiO_3$ layers. Recently it was found that bulk $LaNiO_3$ also has a transition to AFM order at about 157 K, similar to the other $RNiO_3$ (R = rare earth, Y) compounds[11], after being long considered a paramagnetic material down to low temperatures. No FM order has been reported, though, for $LaNiO_3$ layers grown on $SrTiO_3$(100)-oriented substrates, such as we employ here.

5.3 Experiment details

The heterostructures studied here were grown on $SrTiO_3$(100) by pulsed-laser deposition (PLD) using a KrF excimer laser (λ = 248 nm), using the same fabrication parameters for all samples. Prior to use, all $SrTiO_3$(100) single-crystal substrates were etched in NH_4F-buffered HF for 2.5 min and annealed at 950 ˚C for 1 h in air in order to obtain uniform TiO_2-surface termination and terraces with uniform width and one unit cell step height. The deposition temperature was 700 ˚C and laser fluence was 3 J/cm^2 for both types of layers. The pulse repetition rate of the laser was 5 Hz for the $SrRuO_3$ layers and 1 Hz for the $LaNiO_3$ layers. For the growth of $SrRuO_3$ and $LaNiO_3$, the oxygen partial pressure was optimized at 0.133 and 0.3 mbar, respectively. The heterostructures were cooled in 100 mbar oxygen atmosphere from 700 ˚C down to room temperature, with a rate of 10 ˚C/min. The growth of each layer was monitored by high oxygen pressure reflective high-energy electron diffraction (RHEED). In order to study the magnetic interlayer coupling we made heterostructures in which the two $SrRuO_3$ layers had different coercive fields. We applied the same heterostructure design as we used for the study of the magnetic coupling of two layers separated by ultrathin $SrIrO_3$[7,8]. The thickness of the top and bottom $SrRuO_3$ layers was nominally 6 and 18 MLs, respectively, and the thickness of each $LaNiO_3$ layer is nominally 2 or 4

Table 5.1. Heterostructures used for the study of magnetic interlayer coupling, with the thickness of the individual $LaNiO_3$ spacer and of the two FM $SrRuO_3$ layers given in MLs (1 ML is about 0.4 nm thick). Two reference samples with a single $SrRuO_3$ layer were investigated for comparison with the heterostructure for which the strong FM coupling was observed.

Sample name	[MLs $LaNiO_3$/MLs $SrRuO_3$/MLs $LaNiO_3$/MLs $SrRuO_3$] grown on $SrTiO_3$(100)	Comment
4LNO/6SRO/4LNO/18SRO	[4/6/4/18]	Strong FM coupling
2LNO/6SRO/2LNO/18SRO	[2/6/2/18]	Weak FM coupling
[4LNO/6SRO/4LNO/18SRO]R	[4/6/4/18]	Strong FM coupling, reference sample for reproducibility of the strong
4LNO/6SRO/4LNO	[4/6/4/0]	Reference sample to simulate the upper part of the 4LNO/6SRO/4LNO/18SRO heterostructure
4LNO/18SRO	[0/0/4/18]	Reference sample to simulate the lower part of the 4LNO/6SRO/4LNO/18SRO heterostructure

MLs (1 ML layer is ≈ 0.4 nm thick). The two $SrRuO_3$ layers have different thicknesses, because here we need two layers that have different coercive fields. We make use of the fact that epitaxial $SrRuO_3$ layers have a pronounced thickness dependence of the coercive field[12-14]. A schematic of the samples is shown in figure 5.1(a). Table 5.1 summarizes the details of the main samples employed here.

The microstructure of the multilayers, such as the sharpness and the coherence of the interfaces and the uniformity of the layer thickness, was investigated by high-angle annular dark field scanning transmission electron microscopy (HAADF-STEM) on cross-section specimens. The elements distribution of the samples was characterized with energy dispersive x-ray spectroscopy (EDS) mapping. These were performed using an FEI Titan 80-200 ChemiSTEM microscope equipped with a super-X EDS system running at 200 kV. X-ray diffraction was carried out in a Rigaku Smart-Lab using a rotating anode source and a 2-bounce Ge (220) monochromator. Simulation of the data was done using the GlobalFit 2.0 software. The magnetization was measured with a superconducting quantum interference device (SQUID) magnetometer (MPMS XL7

from Quantum Design, magnetic field up to 7 Tesla). The surface morphology of our samples was characterized by atomic force microscopy (NX10, Park Systems). A homemade setup that enables the simultaneous measurement of linear resistance or transverse Hall resistance in van der Pauw configuration and the polar magneto-optical Kerr effect (MOKE) was used. We used copper wires glued with silver paint to the corner of the samples for the electrical measurements. We acquired simultaneously Hall resistance and Kerr rotation hysteresis loops under the same field sweeping rates of 0.3 Tesla/min. The polar MOKE studies were performed with the magnetic field applied perpendicular to the thin film surface with incoherent light from a Xe lamp. The spectrum of the polar Kerr rotation angle and its magnitude for $SrRuO_3$ crystals and epitaxial layers[15,16] are influenced by several parameters of the heterostructures, such as the layer thickness-dependent optical properties, the number of interfaces and their sharpness, and the surface morphology and its roughness[17]. Therefore, after finding the optimal measurement conditions for the Kerr rotation angle signal of each sample, we performed the MOKE investigations at slightly different wavelengths: 550 nm wavelength was used for the sample 4LNO/6SRO/4LNO/18SRO, 570 nm was used for 2LNO/6SRO/2LNO/18SRO and 4LNO/18SRO, and 520 nm was used for 4LNO/6SRO/4LNO.

5.4 Results and discussion

5.4.1 Microstructure investigations

We investigated the microstructure of the heterostructures with the focus on the quality of the interfaces and the integrity of the ultrathin $LaNiO_3$ spacer layer. A main concern was to ascertain that no pinholes formed in the heterostructures. Pinholes would lead to the direct connection of the two FM $SrRuO_3$ layers and result in a trivial FM coupling, which hinders the study of the intrinsic interlayer coupling through the particular type of spacer[18]. The sample that has strong FM coupling and is thus the central piece of the work, 4LNO/6SRO/4LNO/18SRO, was studied in detail by HAADF-STEM and EDS. A cross-section specimen was produced by conventional techniques, which is beneficial for $SrRuO_3$ layers that are sensitive to ion irradiation; however, slight damage of the top layer occurred and thus the top $LaNiO_3$ layer appears to be thinner than 4 MLs (see figures 5.1(b) and 5.1(e)). A high magnification HAADF-STEM micrograph is shown in figure 5.1(b) and highlights the four layers of the 4LNO/6SRO/4LNO/18SRO heterostructure, with clearly separated layers of the expected thickness. Lower magnification HAADF-STEM micrographs, showing larger areas of the cross-section, are shown in figure 5.2. The spacer $LaNiO_3$ layers appear to have a one ML thickness variation at the top interface with the 6 MLs $SrRuO_3$; the presence of a step is marked by the red lines drawn on the micrograph in figure 5.1(b) and figure 5.2. The chemical element distribution across the entire stack was investigated by EDS and enabled us to check the uniform distribution of the cations and the sharpness of the interfaces. Figure 5.1(e) shows a high magnification HAADF-STEM micrograph of the 4LNO/6SRO/4LNO/18SRO sample, marking the

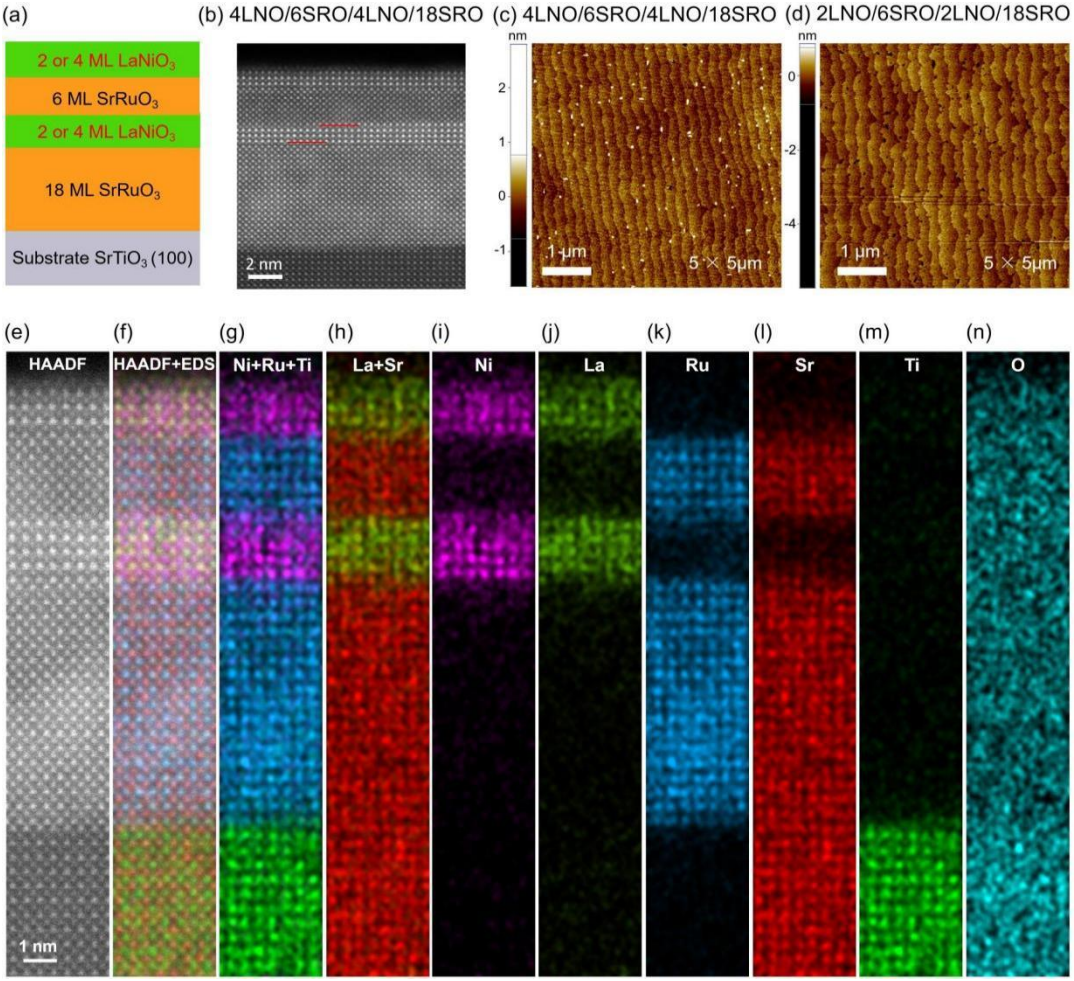

Figure 5.1: The design of the heterostructures employed for the interlayer coupling study and their microstructure: (a) Schematics of samples; (b) HAADF-STEM cross-sectional image of the 4LNO/6SRO/4LNO/18SRO sample, with 4 ML $LaNiO_3$ spacer and capping layers; (c) and (d) AFM topography images (5 μm–5 μm areas) of the two main samples (as mentioned at the top of the images); (e–n) high-resolution HAADF-STEM cross-sectional image combined with EDS mapping of the distribution of the chemical elements (noted at the top of the images) across the 4LNO/6SRO/4LNO/18SRO heterostructure, including part of the $SrTiO_3$ substrate, yielding Ti signal.

region where atomic resolution EDS was performed. The HAADF image overlaid with the overall EDS mapping shows an overview of the layer sequences and distribution of all the *A*-site and *B*-site perovskite-type cations (see figure 5.1(f)). The meaning of the colors is the same as in the elemental EDS maps shown in further detail in figure 5.1; each color corresponds to a particular ion. Taken separately, the EDS maps of the *B*-site (Ni, Ru, and Ti) and *A*-site (Sr and La) cations across the multilayer are shown in figures 5.1(g) and 5.1(h), respectively. Images displaying the distribution of all the individual ions (i.e., Ni, La, Ru, Sr, Ti, and O), across all the layers and at the top of the substrate, are shown in figures 5.1(i)–(n), respectively. In conclusion, the EDS

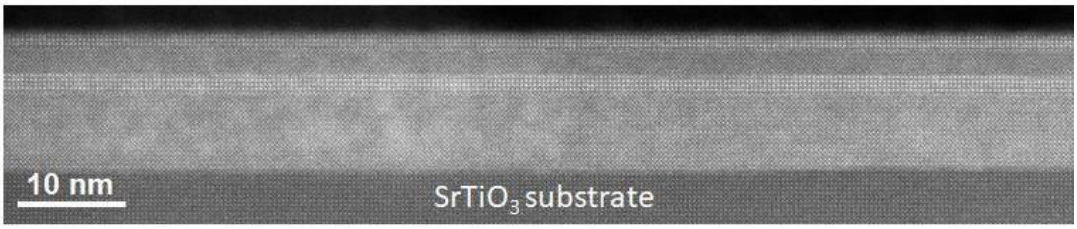

Figure 5.2: lower magnification HAADF-STEM micrographs of the 4LNO/6SRO/4LNO/18SRO heterostructure studied for the strong FM interlayer coupling.

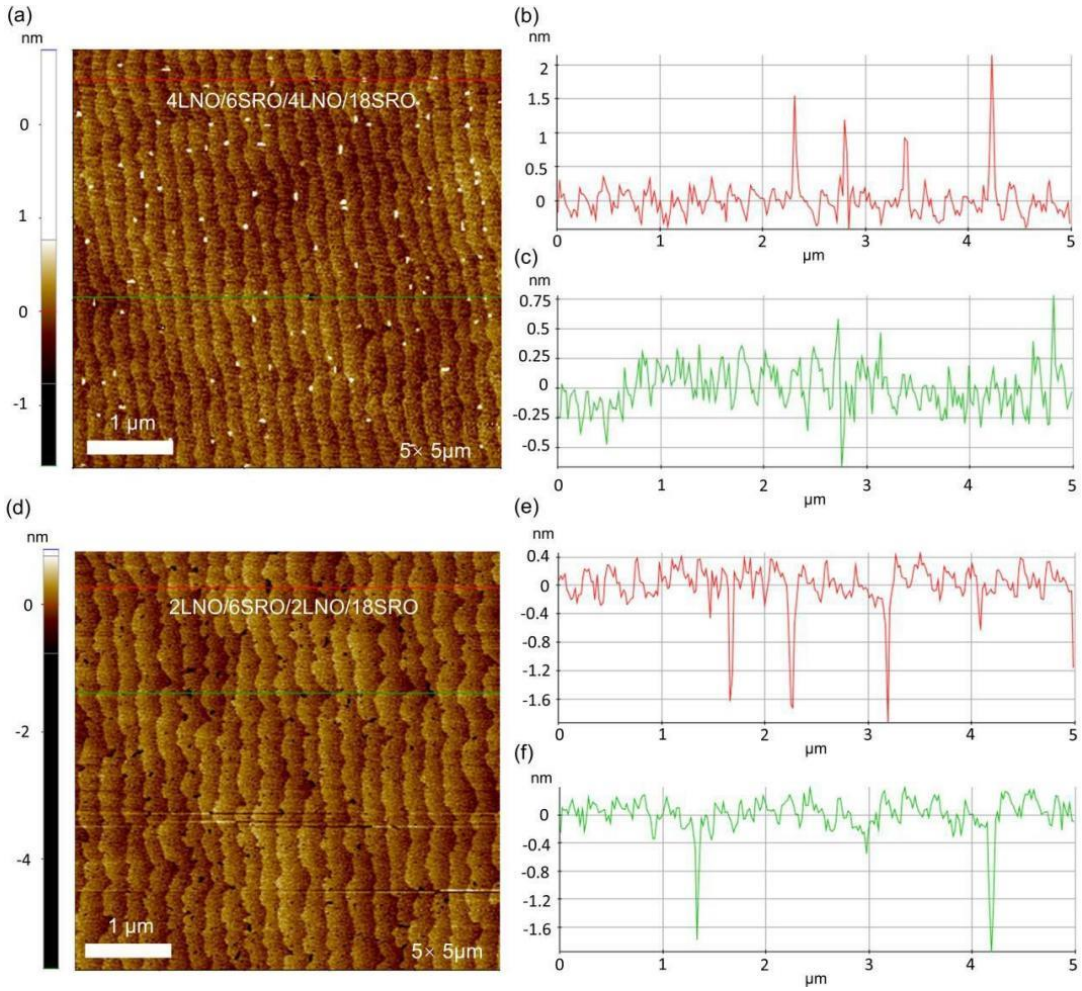

Figure 5.3: AFM topography images and analyses of the topography of the two heterostructures used for the interlayer coupling study: (a)-(c) for the 4LNO/6SRO/4LNO/18SRO and (d)-(f) for the 2LNO/6SRO/2LNO/18SRO heterostructure.

investigation strongly indicates that the spatial extent of all the cations matches the expected layer thickness, in agreement with the RHEED monitoring of the individual layer growth and fulfilling our sample design. Besides, we performed atomic force microscopy (AFM) of all the samples under study, having as a prime objective to determine whether pinholes formed in the heterostructures. The morphology of the

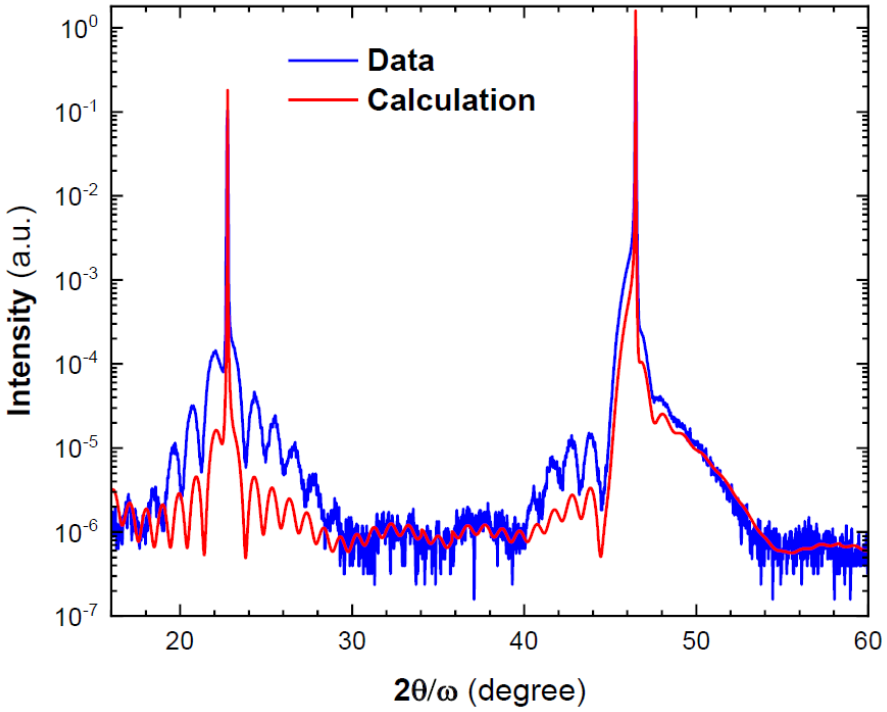

Figure 5.4: XRD scan of the 4LNO/18SRO reference, confirming the high crystalline quality of the heterostructure. The data is compared to a simulation (see Table 5.2 for details).

top surface of the heterostructures showed the step-and-terrace pattern inherent to the vicinal $SrTiO_3$ substrate surface, with uniform terraces, used for the growth. This is also a consequence of the growth mode of the $SrRuO_3$ layers (step-flow growth) and of the
$LaNiO_3$ layers (layer-by-layer growth), under the used PLD growth conditions[19,20]. The 4LNO/6SRO/4LNO/18SRO heterostructure does not exhibit holes, but tiny particles seen as white spots and analyzed by the section profiles shown in figures 5.1(c) and 5.3(a)-(c). The 2LNO/6SRO/2LNO/18SRO heterostructure has some apparent pinholes of 100–200 nm lateral size, which are about 1.9 nm deep (see figures 5.1(d) and figure 5.3(d)-(f)). These pinholes are thus less than 10 MLs deep (about 4 nm) and cannot lead to the direct coupling between the top and bottom $SrRuO_3$ layers[21].

In addition, x-ray diffraction of the reference sample 4LNO/18SRO is shown in figure 5.4. The parameters summarized in table 5.2 indicate a possible deviation of up to 1.75 MLs in the estimation of the SRO layer thickness (19.75 MLs instead of 18 MLs). As we kept the number of laser pulses constant (and the other relevant PLD parameters) for all the samples, we are confident that the thickness of the bottom SRO layer is the same for all the heterostructures, and thus none of the conclusions of the paper are affected by this possible deviation from the nominal 18 MLs thickness.

5.4.2 Magnetic interlayer coupling

Table 5.2: Calculation of thickness of 4LNO/18SRO heterostructure.

Material	Number of layers (nominal)	Out-of-plane lattice parameter (Å)	Thickness (nm)
SRO	19.75	3.95 ± 0.005	7.8 ± 0.05
LNO	4	3.76 ± 0.005	1.4 ± 0.01
STO	-	3.905	-

The double-layer $SrRuO_3$ heterostructures with layers of two different thicknesses were subjected to the measurement of full and minor hysteresis loops by means of MOKE and Hall effect measurements and by SQUID magnetometry. To characterize the type and strength of coupling, we measured the major and minor hysteresis loops at different temperatures below the Curie temperatures of two different thickness of $SrRuO_3$ layers (below 140 K). The major and minor loops of the Kerr rotation angle measured for the 2LNO/6SRO/2LNO/18SRO heterostructure are shown in figures 5.5(a), 5.5(c) and 5.5(e). We show the results at three representative temperatures: 10, 90, and 100 K (around 100 K the anomalous Hall effect (AHE) shows a change of behavior, as seen later).

For comparison, we measured *M*(H) major and minor loops by SQUID magnetometry (see figure 5.6(d)). The MOKE major loops present two sharp magnetization reversal steps and tails at high magnetic field. The tail originates from the multiple magnetizations switching steps in multi-twin-domain or domain pinning in the thicker $SrRuO_3$ layer[22,23]. Additionally, the rotation of the magnetization to align with the large perpendicular magnetic field may also contribute to the tail features. Inspecting closely the loop at 10 K, we see that the two steps occur at ~0.27 T corresponding to the magnetization switching of the bottom 18 MLs $SrRuO_3$ and at ~0.34 T due to magnetization reversal of the top 6 MLs $SrRuO_3$. From our past investigations, we know that the two $SrRuO_3$ layers of these thicknesses have different temperature dependence of the coercive field[7]. At 10 K the 18 MLs $SrRuO_3$ has a lower coercive field, but at 90 and 100 K the thinner 6 MLs layer has a lower coercive field (as is approaching its Curie temperature of about 113 K). Similarly, two steps were observed for the Kerr loops acquired at 90 and 100 K, corresponding to two magnetization reversal processes, with the bottom $SrRuO_3$ having a larger reversal field than the top $SrRuO_3$, which is in agreement with our former work[7]. The shift of the minor Kerr rotation loops with respect to the major loops at 10, 90, and 100 K was negative and evaluated to about -100, -64, and -46 mT, respectively. The decrease of the loop shift with increasing temperature indicates a decrease of the coupling strength. For the quantitative evaluation of the coupling strength, we made use of the

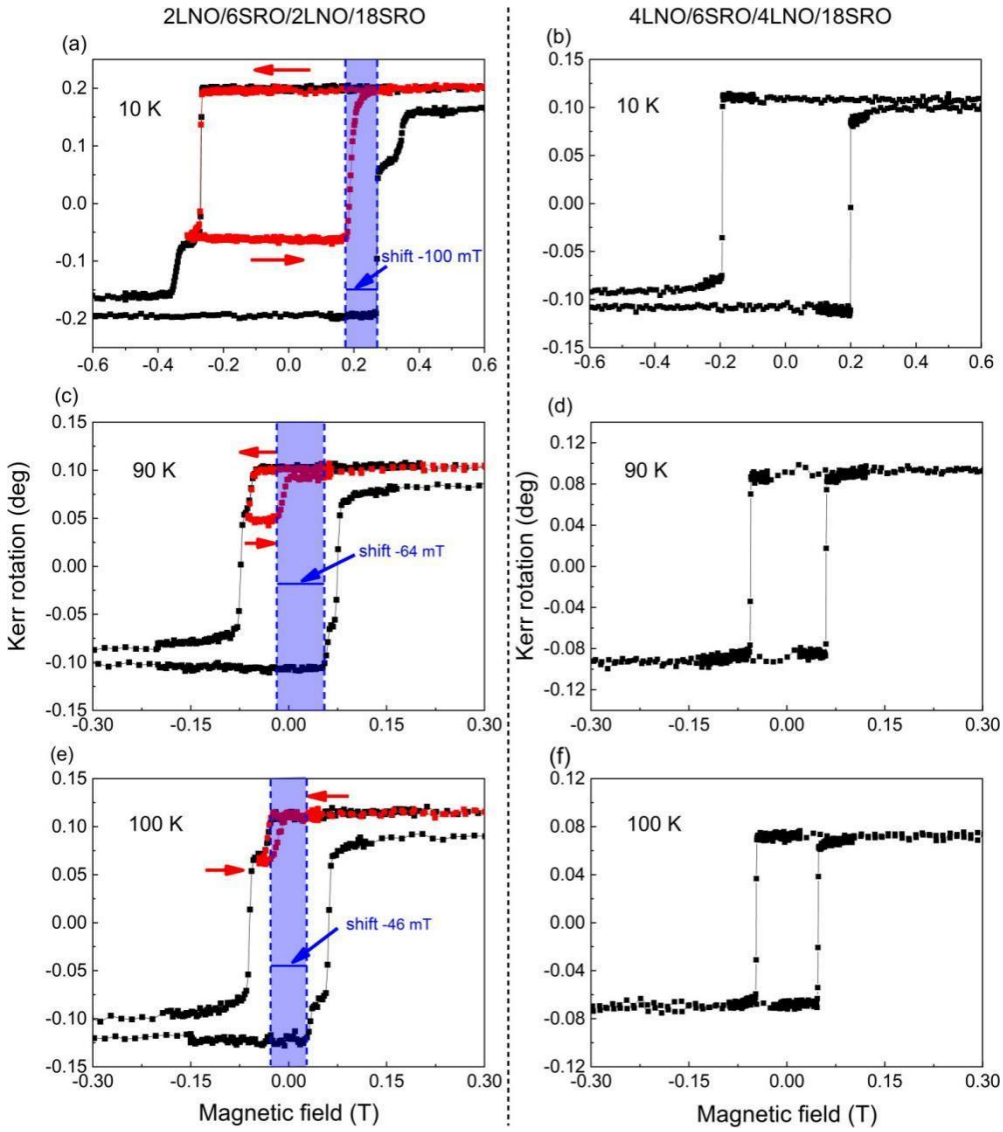

Figure 5.5: MOKE (Kerr rotation) loops of the heterostructures with 2 or 4 ML thick spacer or capping $LaNiO_3$ layers: (a), (c), (e) Major loop and minor loops at 10, 90, and 100 K, respectively, for the heterostructure 2LNO/6SRO/2LNO/18SRO with weak coupling; (b), (d), and (f) only major loops for the 4LNO/6SRO/4LNO/18SRO heterostructure with strong coupling. The minor loops (marked in red) were measured between saturation in positive fields and reversal field of −0.271 T, −0.058 T, and −0.027 T. The magnetic field was applied perpendicular to the heterostructure surface for all measurements.

M(H) loop measurements by SQUID (see figure 5.6(d))). M(H) loop measurements enabled us to determine the saturation magnetization for the two $SrRuO_3$ layers as these values are needed for the estimation of the interlayer coupling strength[7]. We estimated the interlayer coupling strength J_{IC} as 106 μJ/m^2 at 10 K[24]. For the heterostructures with $SrIrO_3$/$SrZrO_3$ spacer, we obtained the largest FM coupling strength of about 35 μJ/m^2 at 10 K[7]. Thus, the coupling of the $SrRuO_3$ layers through the 2 MLs $LaNiO_3$ spacer is FM, larger than for the $SrIrO_3$/$SrZrO_3$ spacer of the same thickness, however still rather weak.

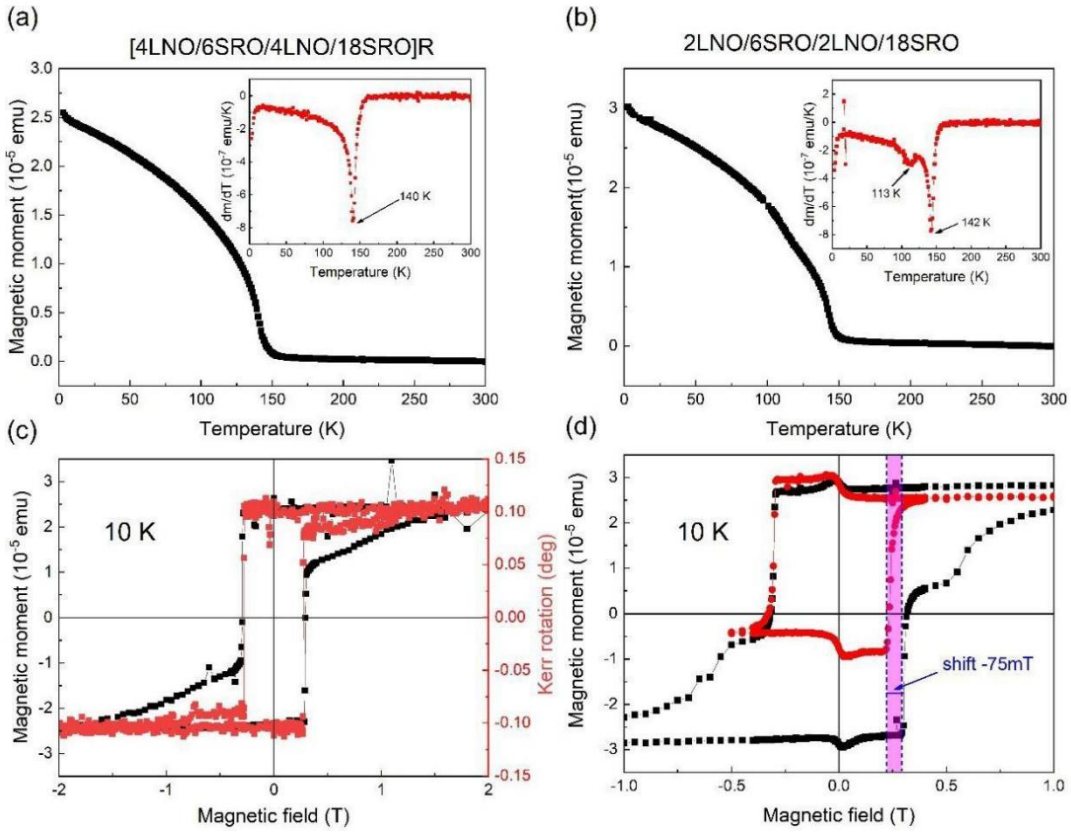

Figure 5.6: SQUID magnetometry investigations of the [4LNO/6SRO/4LNO/18SRO]R and 2LNO/6SRO/2LNO/18SRO heterostructures with magnetic field applied perpendicular to the sample surface：(a) and (b) Temperature dependence of magnetic moment under field-cooled (FC) mode with applied magnetic field of 0.1 T for [4LNO/6SRO/4LNO/18SRO]R and 2LNO/6SRO/2LNO/18SRO, respectively; (c) comparison of m(H) hysteresis loop and Kerr rotation loop of the [4LNO/6SRO/4LNO/18SRO]R, both measured at 10 K; (d) major m(H) loop at 10 K and minor loop between saturated state (+ 3 T) and a reversal field of -0.3 T, for the weakly coupled heterostructure, 2LNO/6SRO/2LNO/18SRO. The inset in (a) and (b) shows the first derivative of the magnetic moment with respect to temperature, to determine the Curie temperatures for the two $SrRuO_3$ layers of the heterostructures.

To determine the Curie temperatures of the two ferromagnetic $SrRuO_3$ layers of the heterostructures used for the interlayer coupling study, we measured the magnetic moment as a function of temperature by SQUID magnetometry using the SQUID with field cooled (FC) method. The samples were cooled from room temperature to 3 K with a magnetic field of 0.1 T applied perpendicular to the sample surface, and the magnetic moment was recorded during the warming process under 0.1 T. The magnetic moment as a function of temperature (m(T) curves) are shown in figure 5.6(b) for 2LNO/6SRO/2LNO/18SRO. We saw the fingerprint of two ordering transition occurring at about 142 K and 113 K, and we attribute them to the thick bottom $SrRuO_3$ layer and the thin top $SrRuO_3$ layer, respectively (see inset of figure 5.6(b)). These two

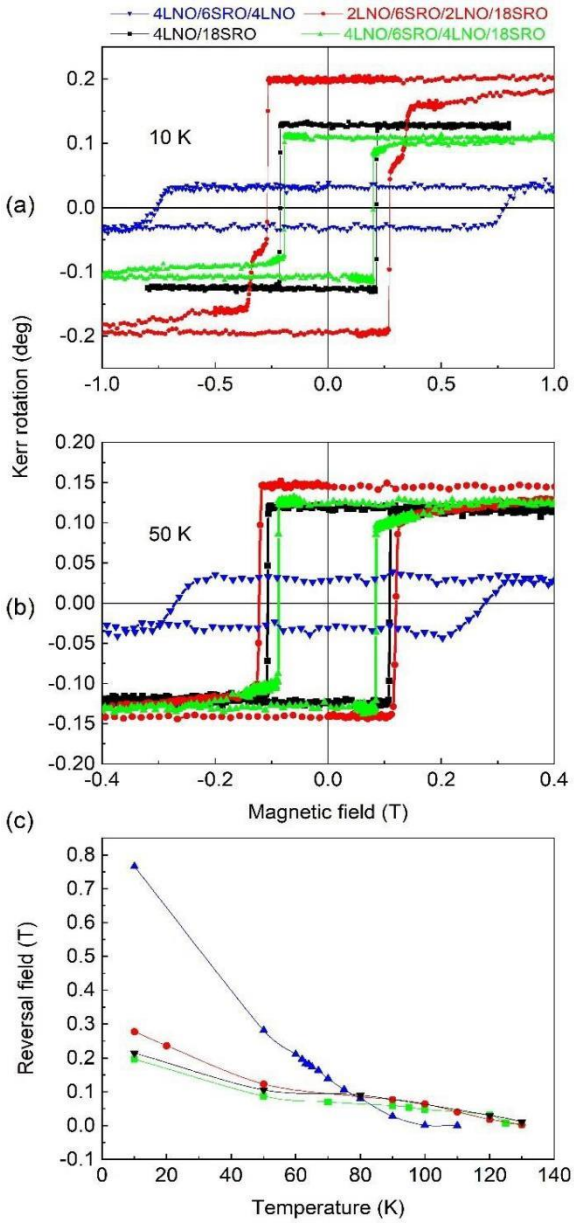

Figure 5.7: (a) and (b) Kerr rotation loops for the 4LNO/6SRO/4LNO/18SRO (green), 2LNO/6SRO/2LNO/18SRO (red), 4LNO/6SRO/4LNO (blue) and 4LNO/18SRO (black) heterostructure at 10 K and 50K, respectively. (c) Temperature dependence of the reversal fields for the $SrRuO_3$ layers of the four samples (colors as for the loops above), with the values obtained from MOKE loop measurements. For the 2LNO/6SRO/2LNO/18SRO heterostructure, only the reversal field of the bottom layer are shown in (c).

transitions strongly indicate that for the 2LNO/6SRO/2LNO/18SRO heterostructure the two $SrRuO_3$ layers are not strongly magnetically coupled.

For the weakly coupled heterostructure, 2LNO/6SRO/2LNO/18SRO, we found that the major magnetic moment m(H) loop shows two marked steps corresponding to the magnetic moment reversal of the two $SrRuO_3$ layers at different fields (see figure

5.6(d)). The small humps around zero field are artifacts as a result of the correction we had to perform because of an impurity contribution (introduced by the cutting of the sample to make it fit in the straw holder for the SQUID magnetometer). To cross check our conclusions provided by the Kerr loops (full and minor) (see figure 5.5) concerning the type and the strength of the magnetic coupling, we also measured a minor m(H) loop by SQUID at 10 K. The minor loop shows negative shift of -75 mT with respect to the major loop, and confirms the ferromagnetic interlayer coupling between the two $SrRuO_3$ layers. We compared the loop shift from the SQUID magnetometry m(H) results with polar magneto-optic Kerr effect (MOKE) measurements (see figure 5.5(a)). The different shift values (-100 mT vs. -75 mT) may originate from the different measurement conditions between the SQUID and the MOKE loops, as they are performed with different instruments. For the value of the shift of -75 mT measured with the SQUID, we estimated the interlayer coupling strength J_{IC} as 79.2 $\mu J/m^2$ at 10 K by using the Eqs. (1a) and (1b) mentioned by van der Heijden *et al.*,[24] which is more than double of that of our $SrRuO_3$ layers separated by 2 MLs $SrZrO_3/SrIrO_3$ [7]. However, in figure 5.5, we calculated the J_{IC} using the shift values obtained from running minor and full Kerr loops, as we could measure such loops at more temperatures than with the SQUID.

When we increased the thickness of the $LaNiO_3$ spacer and capping layer to 4 MLs, a single magnetization reversal occurred at a common value of the magnetic field at all temperatures down to 10 K (see the Kerr rotation loops in figures 5.5(b), 5(d) and 5(f)). This indicates that the 4LNO/6SRO/4LNO/18SRO heterostructure has a strong intrinsic magnetic interlayer coupling and meets our goal of finding the conditions for which the two FM layers reverse their magnetization simultaneously at the same value of the applied field. In addition, we also performed the SQUID measurements of the heterostructures as a crosscheck of the Kerr rotation measurements and to measure the saturation magnetization of the $SrRuO_3$ layers, which we used in the calculation of the interlayer coupling. In addition, to check the reproducibility and further confirm the strong FM coupling, we presented the comparison of SQUID M(H) hysteresis loop and Kerr rotation loop of reference sample [4LNO/6SRO/4LNO/18SRO]R, measured at 10 K as shown in figure 5.8(c), which show very similar coercive fields and a single reversal of the magnetization. This confirms that the Kerr rotation angle loops (see figure 5.5) correctly follow the magnetization reversal process of the heterostructures. It further confirms the strong magnetic coupling of the heterostructures with 4 MLs thick $LaNiO_3$ spacer.

We investigated also two reference samples (see table 5.1) in order to get information of the properties of the single bottom 18 MLs $SrRuO_3$ layer and single top 6 MLs $SrRuO_3$ layer, when the other FM layer is not present to influence its magnetic properties. We kept the interfaces to be similar to the heterostructures, as for one reference layer we capped the 18 MLs layer with a 4 MLs $LaNiO_3$ layer (sample 4LNO/18SRO), and for the other reference we sandwiched the 6 MLs layer between two 4 MLs $LaNiO_3$ layers (sample 4LNO/6SRO/4LNO). The Kerr rotation loops of

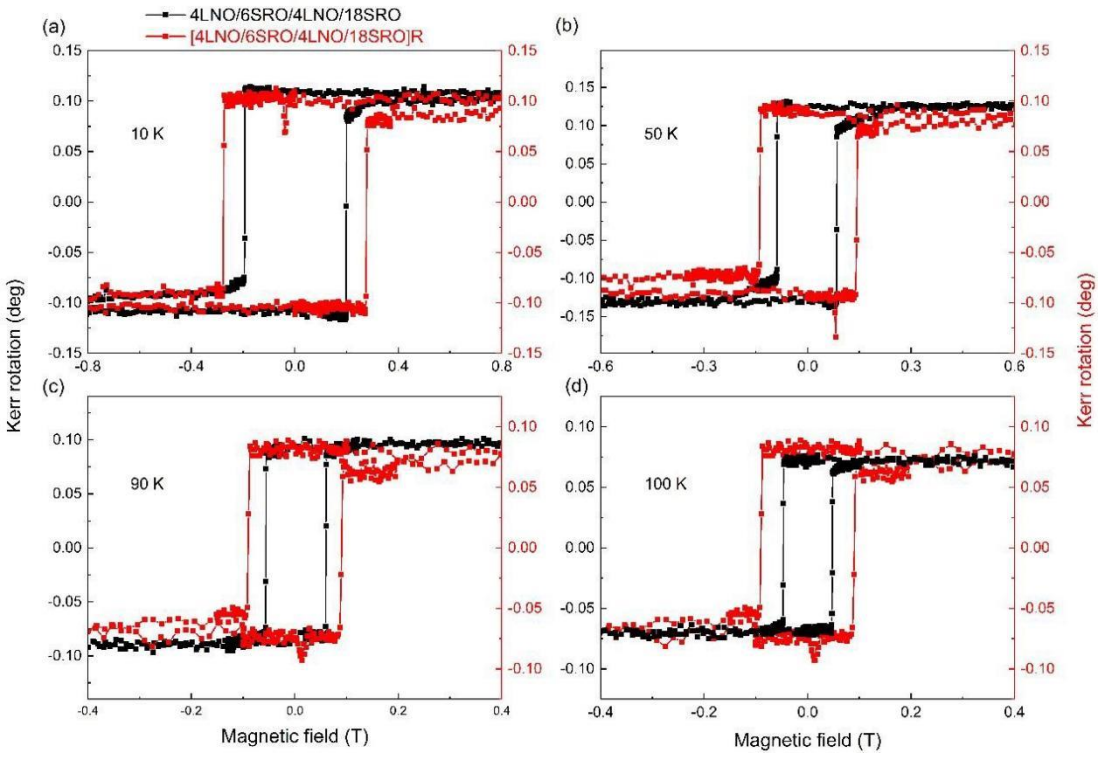

Figure 5.8: Comparison of Kerr rotation loops for 4LNO/6SRO/4LNO/18SRO and its reference sample [4LNO/6SRO/4LNO/18SRO]R at 10 K, 50 K, 90 K and 100 K. The red loops are for the reference sample [4LNO/6SRO/4LNO/18SRO]R.

these three reference samples (4LNO/6SRO/4LNO (blue), 4LNO/18SRO and [4LNO/6SRO/4LNO/18SRO]R) are shown in figure 5.7 and figure5.8. In figure 5.7(a), (b), we present a summary of the results of the MOKE loop measurements of 4LNO/6SRO/4LNO/18SRO, 2LNO/6SRO/2LNO/18SRO, and the two reference samples 4LNO/6SRO/4LNO and 4LNO/18SRO (see table 5.1). As stated in the the above, we investigated these two reference samples to obtain information on the properties of the single bottom 18 MLs $SrRuO_3$ layer and single top 6 MLs $SrRuO_3$ layer, when the other ferromagnetic layer is not present to influence its magnetic properties. We kept the interfaces to be similar to the heterostructures, as for one reference sample we capped the 18 MLs layer with a 4 MLs $LaNiO_3$ layer (sample 4LNO/18SRO), and for the other reference sample we sandwiched the 6 MLs layer between two 4 MLs $LaNiO_3$ layers (sample 4LNO/6SRO/4LNO). From the measurements of the 4LNO/6SRO/4LNO sample, we see that the single 6MLs $SrRuO_3$ layer sandwiched between $LaNiO_3$ layers has a much larger coercive field than when it is coupled to the bottom layer even weakly, as it is in the case of the 2LNO/6SRO/2LNO/18SRO sample. The coercive field of 6MLs $SrRuO_3$ is about 4 times larger than for the top $SrRuO_3$ layer in 4LNO/6SRO/4LNO/18SRO and about three times larger than for the top $SrRuO_3$ layer in 2LNO/6SRO/2LNO/18SRO. If we compare the coercive field of the single 18MLs $SrRuO_3$ layer in the reference 4LNO/18SRO with the coercive field of other samples, we see that its values are

matching closely the ones of the strongly coupled 4LNO/6SRO/4LNO/18SRO heterostructure, and they are slightly smaller than the coercive field values of the bottom 18 MLs $SrRuO_3$ in the 2LNO/6SRO/2LNO/18SRO heterostructure. The latter is consistent with the weak coupling of the 2LNO/6SRO/2LNO/18SRO, which makes the coercive field of the bottom $SrRuO_3$ layer increase slightly and the coercive field of the top $SrRuO_3$ layer decrease considerably.

In order to confirm the reproducibility of the strong interlayer coupling for the heterostructures with 4 MLs thick $LaNiO_3$ spacer, which is the key result of our study, we made a second sample, [4LNO/6SRO/4LNO/18SRO]R, trying to preserve the growth PLD parameters. We point out that some unavoidable differences are induced by the quality of the $SrTiO_3$ substrate used for the growth. It is known that the details of the vicinal surface of the substrate influence the growth of the $SrRuO_3$ layers and may result in the formation of the crystallographic domains. These domains then influence the coercive field and the magnetization reversal process of the $SrRuO_3$ layer[23]. We think this is what happens for the [4LNO/6SRO/4LNO/18SRO]R reference sample, that has increased coercive field with respect to the 4LNO/6SRO/4LNO/18SRO. Nevertheless, as we can see from the comparison presented in figure 5.8, the Kerr rotation loops of the two samples are very similar in their behavior at all temperatures, apart from the coercive field difference. The loops of both samples show a single reversal of the magnetization at all the temperatures, confirming the strong ferromagnetic coupling of the layers when the $LaNiO_3$ spacer layer is 4 MLs thick. We point out that it is impossible to probe the transport properties of the $LaNiO_3$ spacer layer, as it is buried between the two metallic $SrRuO_3$ layers. Direct measurements of the resistivity of the 2 or 4 MLs thick $LaNiO_3$ spacers, to monitor the metal-insulator transition, are impossible in our heterostructures with metallic $SrRuO_3$ layers.

Based on the above discussion, now we can explain the different strength of interlayer coupling for the heterostructures with 4MLs spacers and 2MLs spacers. The difference in the strength of the FM coupling between the two heterostructures must be the consequence of the difference in the thickness of the $LaNiO_3$ spacer. We ascribe this to the abrupt change of the electronic properties of the $LaNiO_3$ as the thickness increases from 2 to 4 MLs[10]. The interlayer coupling is only weakly FM through the insulating 2 MLs $LaNiO_3$. For this heterostructure, the mechanism of the weak coupling can be a combination of tunneling through the insulating layer plus the effect of pinholes[7]. The coupling through the metallic 4 MLs thick $LaNiO_3$ thus becomes strongly FM, possibly via a Ruderman-Kittel-Kasuya-Yosida (RKKY) type of exchange coupling of the itinerant FM $SrRuO_3$ layers via the conduction electrons[25-29].

5.4.3 Resistivity measurements of bare $LaNiO_3$ thin films deposited on $SrTiO_3$(100)

As we discussed, the 4LNO layers thin films have been reported to show metallic conductivity, and the 4LNO/6SRO/4LNO/18SRO and 2LNO/6SRO/2LNO/18SRO

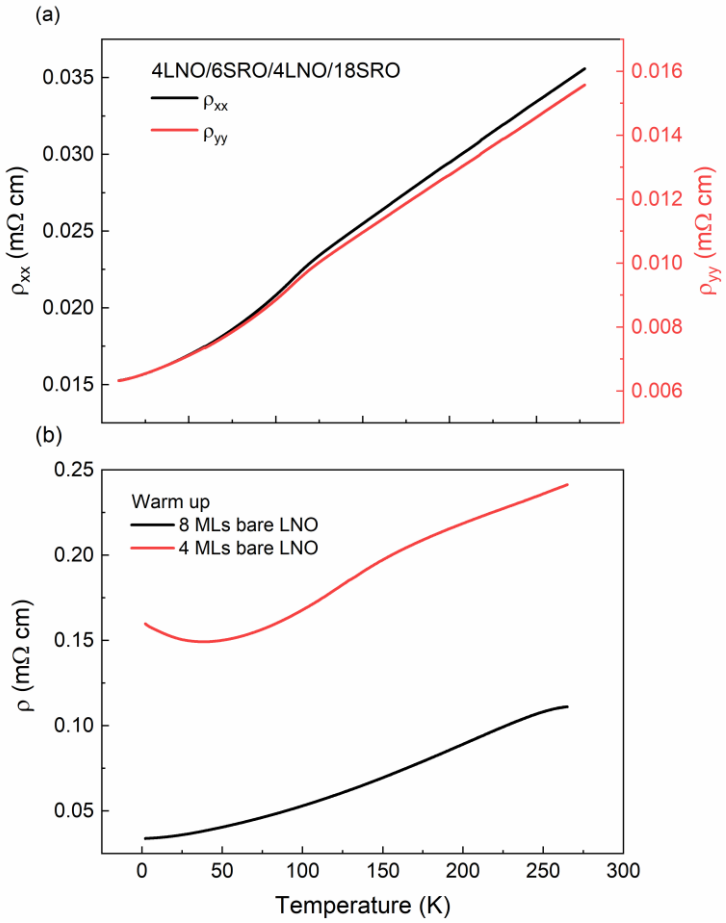

Figure 5.9: (a) temperature dependence of resistivity during the warm up process when 100uA and 60uA were applied for 8MLs and 4MLs bare LNO, respectively, by the 4-point probes method. The ρ_{xx} and ρ_{yy} were obtained when measuring the sample along two vertical edges. (b) The bare 4 (red) and 8(black) MLs $LaNiO_3$ thin films were deposited on $SrTiO_3$ (100).

show a stronger interlayer coupling than the heterostructures with $SrIrO_3$ spacers probably due to the different interlayer coupling mechanisms.

For the 4LNO/6SRO/4LNO/18SRO and 2LNO/6SRO/2LNO/18SRO heterostructures, their resistivity can be obtained by resistance measurements of whole samples. However, the LNO spacer layers cannot be probed easily inside the heterostructures, as their conductivity is worse than for the thicker $SrRuO_3$ metallic layers. The resistivity of the 4LNO/6SRO/4LNO/18SRO is one order of magnitudes smaller than that of 4 or 8 MLs bare LNO layers, as shown in the figure 5.9. The resistivity of the 4 MLS LNO bare thin film is larger than the 8 MLs LNO bare thin film (see figure 5.9(b)). Furthermore, the 4 MLs LNO thin film shows an increase in resistivity, indicating a tendency of metal-insulator transition (MIT) for the thinner thin films and a good agreement with the literature[9,30]., M. Golalikhani *et al.*[9] found that room-temperature metallic behavior persists until the film thickness is reduced to an unprecedentedly small 1.5 unit cells (NiO_2 termination) for the few unit cells in thickness

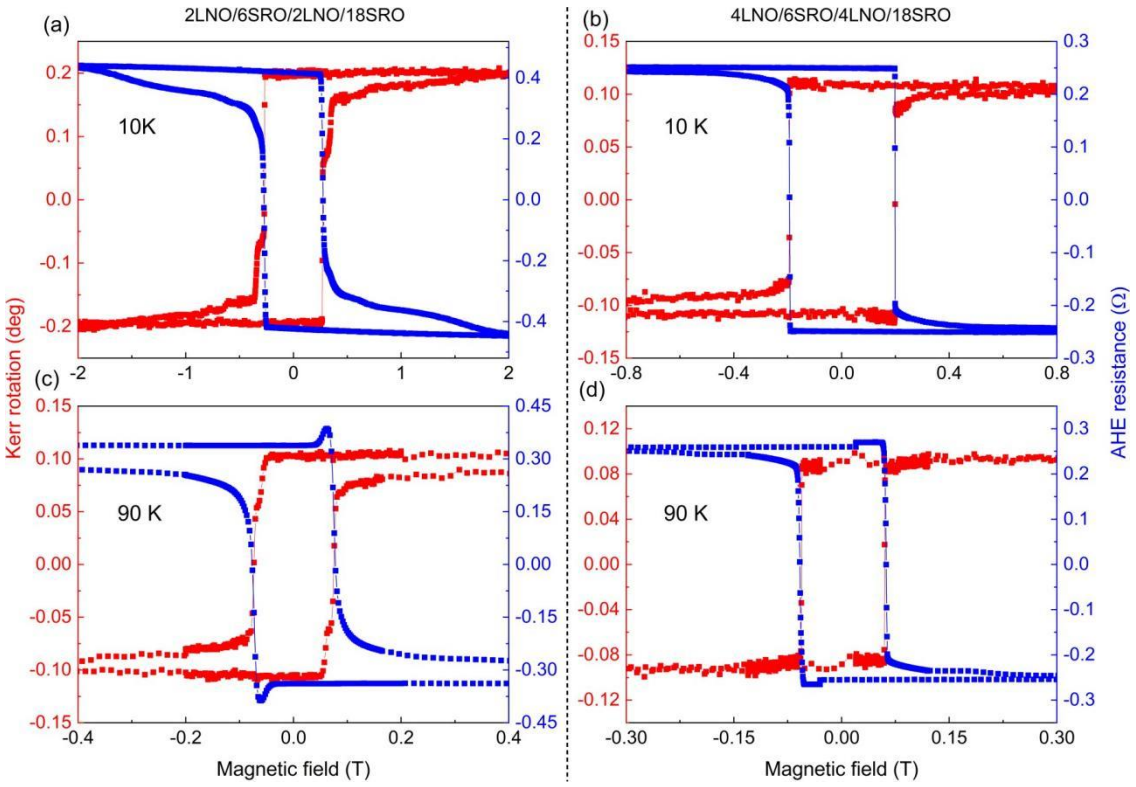

Figure 5.10: Anomalous Hall resistance loops (blue) and the Kerr rotation angle loops (red) measured simultaneously at 10 and 90 K for the 2LNO/6SRO/2LNO/18SRO ((a) and (c)) and for the 4LNO/6SRO/2LNO/18SRO ((b) and (d)) heterostructures.

LNO thin films deposited on $LaAlO_3$. They stated that the metallic states are fragile for the $LaNiO_3$ ultrathin films, and the oxygen vacancies due to the absence of the apical oxygen ions play an important role in the fundamental understanding of the MIT in ultrathin $LaNiO_3$ films. Besides, E. Cappelli *et al.*[30] reported that $LaNiO_3$ thin films deposited on $LaAlO_3$ (LAO) undergo a metal-insulator transition when their thickness is reduced to a few unit cells. The MIT can be attributed to the structural relaxation at LNO/LAO interface or LNO surface.

For our sample system of LNO grown on STO substrates with large tensile epitaxial strain, when the thickness of LNO decreases, the heterostructures tend to show MIT, which probably originates from the lattice disorder or defect based on the microstructure investigation

5.4.4 Hall effect resistance loops

Transverse resistance loops resulting from the Hall effect are a complementary way to probe the behavior of the magnetization reversal in FM thin films. Besides this, the Hall resistance loops may unravel additional features inherent to magneto-transport effects, which are not present in the M(H) loops measured by SQUID or in the Kerr rotation loopsdiscussed above. Here we define the total transverse Hall resistance R_{XY} as the ratio of the Hall voltage and the excitation current I: $R_{xy} = V_{xy}/I = (V_{AHE,xy}$

$+ V_{OHE,\,xy}$)/*I*. The measured Hall voltage, V_{xy}, has two contributions: One from the AHE, $V_{AHE,xy}$, and the other from the ordinary Hall effect, $V_{OHE,xy}$. The contribution of the ordinary Hall effect was subtracted from all the Hall loops shown in the paper[5,8]. We measured the Hall resistance R_{XY} of the two heterostructures in van der Pauw geometry. The MOKE and AHE measurements were performed simultaneously with our homebuilt setup. In figure 5.10, we show the MOKE and Hall loops measured at 10 and 90 K for the two heterostructures. Both types of loops show consistent values of the coercive field for both samples at all temperatures. The Kerr and Hall loops of both samples exhibit remarkably similar behavior at 10 K, as both the Kerr rotation angle and the Hall resistance are expected to be directly proportional to the out-of-plane magnetization. The Hall loops measured at 90 K (and at other temperatures around 90 K) have some peculiar additional features, with which we are familiar from our investigations of $SrRuO_3$/$SrIrO_3$ heterostructures and other recent reports[5,8,31]. Closer inspection of the Hall loop of the 2LNO/6SRO/2LNO/18SRO heterostructure in comparison to the corresponding MOKE loop (see figure 5.10(c)) shows that the Hall loop develops a hump-like feature in the field range in which the top $SrRuO_3$ layer reverses its magnetization. We demonstrated in the past that the origin of such a hump is in the change of sign from negative to positive that the AHE constant undergoes as one approaches the Curie temperature, T_C, of the $SrRuO_3$[8]. The thin top $SrRuO_3$ layer has lower T_C and thus changes its sign before the thick bottom $SrRuO_3$ layer does. The temperature dependence of the anomalous Hall constant of $SrRuO_3$ is known to be complex and it is a result of its electronic band structure[32]. In the temperature range where the two SRO layers have different signs of the anomalous Hall constant, the Hall loops have such hump-like features. This is visible also for the Hall loop of the second 4LNO/6SRO/4LNO/18SRO heterostructure, though the hump is less pronounced (see figure 5.10(d)). In conclusion, the Hall effect loop measurements further support our Kerr and SQUID magnetometry loop measurements that demonstrate a strong FM interlayer coupling in the heterostructure with 4 MLs thick $LaNiO_3$ and a much weaker coupling in the heterostructure with 2 MLs $LaNiO_3$ spacer.

5.5 Summary

To summarize, prompted by our previous investigations of magnetic interlayer coupling for various $SrRuO_3$-based epitaxial heterostructures, we have searched for an oxide material structurally compatible with $SrRuO_3$ that can make the magnetic interlayer coupling strongly FM. Past studies with $SrTiO_3$, $SrZrO_3$, or $SrIrO_3$ used as spacers between $SrRuO_3$ layers showed that the coupling was at most weakly FM and the two FM layers reversed the magnetization at different field values[7,8]. $LaNiO_3$ turned out to be a suitable candidate and the interlayer coupling between the two $SrRuO_3$ layers changed from weakly FM to strongly FM as the thickness of the spacer increased from 2 to 4 MLs. We think that the change of the coupling strength is related to changes in the electronic properties of the $LaNiO_3$ spacer with thickness, as it most likely becomes metallic and enables a FM coupling via a RKKY type of exchange

coupling[25-29]. Finding solutions for how to couple the $SrRuO_3$ layers in a ferromagnetic manner is highly relevant for designing heterostructures in which control over the formation of the magnetic domains should be achieved.

5.6 References

[1] P. Zubko, S. Gariglio, M. Gabay, P. Ghosez, and J.-M. Triscone, Annual Review of Condensed Matter Physics **2** (1), 141 (2011).

[2] H. Y. Hwang, Y. Iwasa, M. Kawasaki, B. Keimer, N. Nagaosa, and Y. Tokura, Nature Materials **11** (2), 103 (2012).

[3] J. Matsuno, N. Ogawa, K. Yasuda, F. Kagawa, W. Koshibae, N. Nagaosa, Y. Tokura, and M. Kawasaki, Science Advances **2** (7), e1600304.

[4] Y. Ohuchi, J. Matsuno, N. Ogawa, Y. Kozuka, M. Uchida, Y. Tokura, and M. Kawasaki, Nature Communications **9** (1), 213 (2018).

[5] L. Yang, L. Wysocki, J. Schöpf, L. Jin, A. Kovács, F. Gunkel, R.Dittmann, P. H. M. van Loosdrecht, and I. Lindfors-Vrejoiu, Physical Review Materials **5** (1), 014403 (2021).

[6] L. Wysocki, J. Schöpf, M. Ziese, L. Yang, A. Kovács, L. Jin, R. B. Versteeg, A. Bliesener, F. Gunkel, L. Kornblum, R. Dittmann, P. H. M. van Loosdrecht, and I. Lindfors-Vrejoiu, ACS Omega **5** (11), 5824 (2020).

[7] L. Wysocki, R. Mirzaaghayev, M. Ziese, L. Yang, J. Schöpf, R. B. Versteeg, A. Bliesener, J. Engelmayer, A. Kovács, L. Jin, F. Gunkel, R. Dittmann, P. H. M. van Loosdrecht, and I. Lindfors-Vrejoiu, Applied Physics Letters **113** (19), 192402 (2018).

[8] L. Wysocki, L. Yang, F. Gunkel, R. Dittmann, P. H. M. van Loosdrecht, and I. Lindfors-Vrejoiu, Physical Review Materials **4** (5), 054402 (2020).

[9] M. Golalikhani, Q. Lei, R. U. Chandrasena, L. Kasaei, H. Park, J. Bai, P. Orgiani, J. Ciston, G. E. Sterbinsky, D. A. Arena, P. Shafer, E. Arenholz, B. A. Davidson, A. J. Millis, A. X. Gray, and X. X. Xi, Nature Communications **9** (1), 2206 (2018).

[10] S. Catalano, M. Gibert, J. Fowlie, J. Íñiguez, J. M. Triscone, and J. Kreisel, Reports on Progress in Physics **81** (4), 046501 (2018).

[11] H. Guo, Z. W. Li, L. Zhao, Z. Hu, C. F. Chang, C. Y. Kuo, W. Schmidt, A. Piovano, T. W. Pi, O. Sobolev, D. I. Khomskii, L. H. Tjeng, and A. C. Komarek, Nature Communications **9** (1), 43 (2018).

[12] J. Xia, W. Siemons, G. Koster, M. R. Beasley, and A. Kapitulnik, Phys Rev B **79** (14), 140407 (2009).

[13] G. Koster, L. Klein, W. Siemons, G. Rijnders, J. S. Dodge, C.-B. Eom, D. H. A. Blank, and M. R. Beasley, Reviews of Modern Physics **84** (1), 253 (2012).

[14] G. Malsch, D. Ivaneyko, P. Milde, L. Wysocki, L. Yang, P. H. M. van Loosdrecht, I. Lindfors-Vrejoiu, and L. M. Eng, ACS Applied Nano Materials **3** (2), 1182 (2020).

[15] H. Ohta, E. Kulatov, J. S. Dodge, Yu Uspenskii, and S. Halilov, Journal of the Magnetics Society of Japan **22** (S_2_MORIS_97), S2_185 (1998).

[16] R. B. Versteeg, Universität zu Köln, 2019.

[17] M. Veis, M. Zahradnik, R. Antos, S. Visnovsky, Ph Lecoeur, D. Esteve, S. Autier-Laurent, j-p Renard, and P. Beauvillain, Science and Technology of

Advanced Materials **15** (1), 015001 (2014).

[18] J. F. Bobo, H. Kikuchi, O. Redon, E. Snoeck, M. Piecuch, and R. L. White, Phys Rev B **60** (6), 4131 (1999).

[19] J. Choi, C. B. Eom, G. Rijnders, H. Rogalla, and D. H. A. Blank, Applied Physics Letters **79** (10), 1447 (2001).

[20] K. Tsubouchi, I. Ohkubo, H. Kumigashira, Y. Matsumoto, T. Ohnishi, M. Lippmaa, H. Koinuma, and M. Oshima, Applied Physics Letters **92** (26), 262109 (2008).

[21] C. L. Platt, M. R. McCartney, F. T. Parker, and A. E. Berkowitz, Phys Rev B **61** (14), 9633 (2000).

[22] V. Jeudy, R. Díaz Pardo, W. Savero Torres, S. Bustingorry, and A. B. Kolton, Phys Rev B **98** (5), 054406 (2018).

[23] W. Wang, L. Li, J. Liu, B. Chen, Y. Ji, J. Wang, G. Cheng, Y. Lu, G.Rijnders, G. Koster, W. Wu, and Z. Liao, npj Quantum Materials **5** (1), 73 (2020).

[24] P. A. A. van der Heijden, P. J. H. Bloemen, J. M. Metselaar, R. M. Wolf, J. M. Gaines, J. T. W. M. van Eemeren, P. J. van der Zaag, and W. J. M. de Jonge, Phys Rev B **55** (17), 11569 (1997).

[25] P. Bruno and C. Chappert, Physical Review Letters **67** (12), 1602 (1991).

[26] J. Unguris, R. J. Celotta, and D. T. Pierce, Physical Review Letters **67** (1), 140 (1991).

[27] Q. Leng, Vincent Cros, R. Schäfer, A. Fuss, P. Grünberg, W. Zinn, Journal of Magnetism and Magnetic Materials, **126**, 367 (1993).

[28] M. D. Stiles, Journal of Magnetism and Magnetic Materials **200** (1), 322 (1999).

[29] N. M. Kreines, Low Temperature Physics **28** (8), 581 (2002).

[30] E. Cappelli, W. O. Tromp, S. M. Walker, A.Tamai, M. Gibert, F. Baumberger, and F. Y. Bruno, APL Materials **8** (5), 051102 (2020).

[31] T. C. van Thiel, D. J. Groenendijk, and A. D. Caviglia, Journal of Physics: Materials **3** (2), 025005 (2020).

[32] L. Klein, J. R. Reiner, T. H. Geballe, M. R. Beasley, and A. Kapitulnik, Phys Rev B **61** (12), R7842 (2000).

Chapter 6 Tailoring the magnetic anisotropy of $SrRuO_3$ layers by epitaxial interfacing with $LaNiO_3$ multilayers

Contents

Contributions to this chapter:

The main contribution to the publication comes from Lin Yang, Ionela Lindfors-Vrejoiu, and Paul H. M. van Loosdrecht. The contributions from the co-authors and others are as below:
1) Lei Jin carried out the scanning transmission electron microscopy measurement and provided me with the initial data analysis.
2) Ionela Lindfors-Vrejoiu fabricated all the samples by PLD.
3) Lena Wysocki and Jörg Schöpf assisted me with the superconducting quantum interference device (SQUID) measurement and analyzed the data.
4) The magneto-optical Kerr effect (MOKE) and Hall measurement were performed with the assistance of Jörg Schöpf.
5) Daniel Jansen performed part of the atomic force microscopy (AFM) measurement for me.

6.1 Abstract

Ferromagnetic thin films with tunable magnetic anisotropy are essential for applications, including spin valves, magnetic tunnel junctions, and magnetic storage devices. Effective magnetic anisotropy in ferromagnetic oxide multilayers is mainly the result of epitaxial growth-induced structural changes affecting magnetocrystalline anisotropy, substrate-induced strain tuning the magnetoelastic anisotropy, interlayer coupling, and dipolar interactions. However, few researchers focus on the tunability of magnetic anisotropy of $SrRuO_3$-based multilayers, due to the complex interaction between different degrees of freedom, e.g., lattice, charge orbit, and spin. In the present work, we investigate the tunability of magnetic anisotropy of $SrRuO_3$-based films by epitaxial interfacing with $LaNiO_3$. We find the magnetic anisotropy of the $LaNiO_3/SrRuO_3$ multilayers changes from more in-plane to out-of-plane when the $LaNiO_3$ layers decrease from 4 MLs to 2 MLs, probably due to oxygen octahedral connectivity at the $SrRuO_3/LaNiO_3$ interfaces, resulting in changes of the octahedral tilt angles and bond lengths, which, in conjunction with the interlayer coupling, dictate the effective magnetocrystalline anisotropy.

6.2 Introduction

Transition metal oxide $SrRuO_3$ (SRO) provides an ideal platform to investigate magnetism and transport in epitaxial oxide heterostructures[1-7]. Since the SRO show surprising itinerant ferromagnetism[8] and tunable magnetic anisotropy[3,7,9]. Moreover, the transport, e.g., magneto and electrical transport, relate to its large magnetocrystalline anisotropy[9-11]and metal-insulator transition (MIT)[12,13], respectively. In addition, the SRO has a close lattice match[7] ($SrRuO_3$ has a pseudocubic lattice parameter of 3.93 Å) with many functional perovskite oxides, such as $SrIrO_3$ with strong orbit-spin coupling[5], $LaNiO_3$ with metal-insulator transition (MIT)[14] and ferroelectrics $BaTiO_3$[15], raise the possibility for the application study in $SrRuO_3$-based heterostructures. More precisely, $SrRuO_3$ epitaxial oxide heterostructures are frequently predicted to be employed in magnetoelectric devices[16-19] and spintronic, such as magnetoresistive random-access memory[20,21] and racetrack memory[5,22,23] due to the tunable magnetic properties, especially the magnetic anisotropy.

As we have already introduced in the chapter two, magnetic anisotropy describes how an object's magnetic properties can depend on direction. The microscopic origin of magnetic anisotropy can be attributed to dipolar interaction, which contributes to shape anisotropy, and the spin-orbit coupling, which contributes to many other types of magnetic anisotropies, i.e., magnetoelastic anisotropy and magnetocrystalline anisotropy[24,25]. Most magnetic films show in-plane magnetic anisotropy, for the shape anisotropy dominates over magnetoelastic anisotropy[20,26]. However, the $SrRuO_3$ with orthorhombic structure grown on STO (001) substrate always shows out-of-plane magnetic anisotropy[3,7,9].

For the past two decades, it has been reported that the magnetic anisotropy of $SrRuO_3$ can be mainly tailored by following two methods: 1) tuning magnetoelastic anisotropy by substrate-induced strain with different substrates materials (e.g., STO, LSAT and $LaAlO_3$(LAO))[27], or controlling the thickness films to induces misfit dislocations and tunes the strain, then the magnetoelastic affects the magnetic anisotropy; 2) tailoring the magnetocrystalline anisotropy via rotating oxygen octahedral lead to the change the length of the Ru-O-Ru bond and angle manipulating the hybridization between Ru *d* orbitals and O *p* orbitals resulting in the change of strain[24,25,28]; or tunning the orientation of lattice distortion with different orientation of substrates[27], or tailoring the interfacial oxygen octahedral coupling in metastable $SrRuO_3$ phases[29], or modifying the doping level by applying a gate voltage or chemical doping to manipulate the magnetocrystalline anisotropy energy (MCAE)[30], or changing the growth mechanism (e.g., step flow or layer by layer growth) resulting in inducing different domain textures[31]. Currently, it is widely shared that the easy axis of SRO shows an angle of approximately 30°- 45°to the normal of the film below the Curie temperature with applied field from zero teslas to several teslas (□10 T). Since the easy axis can be rotated for the changes in intrinsic magnetocrystalline anisotropy due to the strong spin-orbit coupling of heavy Ru ions[7].

Recently, the $SrRuO_3$(SRO)-based heterostructures grown on $SrTiO_3$(STO) (100) substrates with perpendicular magnetic anisotropy and symmetry breaking at the interfaces interfaced with strong spin-orbit coupling (SOC) $SrIrO_3$ layer enable the formation of magnetic skyrmions due to the presence of interfacial Dzyaloshinskii-Moriya interactions (DMI)[5,32]. The magnetic skyrmions with particle-like topological states and nontrivial spin structures can be treated as an excellent candidate for high-density, low-power, and multi-functional memory and logic applications[33]. Considering the critical DMI energy for skyrmions generation $D_C = 4\sqrt{JK}/\pi$ can be defined to evaluate the stability of the skyrmions where *J* and *K* are the exchange stiffness and magnetic anisotropy[34], respectively, manipulating the magnetic anisotropy in multilayers is a reasonable approach to stabilize the skyrmions for the practical applications. In addition, it has been reported that the asymmetric interfaces in Pt/Co/Ir multilayers host additive DMI, which can stabilize the small individual skyrmions at room temperature[35,36]. Moreover, the magnetic anisotropy of $SrRuO_3$-based films can be tuned by capping a nonmagnetic $LaNiO_3$(LNO) layer on top, inducing oxygen octahedral distortion or inserting $Sr_3Al_2O_6$ or $Ba_{1-x}Sr_xTiO_3/BaTiO_3$ bilayer buffer layers as a result of triggering the change of the strain[20,37,38]. Furthermore, the enhancing ferromagnetic interlayer coupling has been confirmed in ferromagnetic SRO multilayers separated by four monolayers (MLs) thick $LaNiO_3$[39]. However, most of these works focus on investigating single layer or bilayer but few on multilayers. Last but not least, motivated by the above review of the strategies to tailor the magnetic anisotropy of SRO, further investigation about tuning the magnetic anisotropy of $SrRuO_3$-based multilayer by growing different capping layers or buffer layers and changing the thickness of spacers should be promising.

This work focuses on investigating the tailoring of the magnetic anisotropy and magnetotransport for LaNO/SRO multilayers. The samples were deposited by Pulsed Laser Deposition (PLD). The microstructure investigated was performed by atomic force microscopy (AFM) and scanning transmission electron microscope (STEM). The magnetic anisotropy was detected by a superconducting quantum interference device (SQUID). The magnetotransport was revealed by a homemade setup that can perform the transverse resistance and MOKE measurement simultaneously. We demonstrate that the easy axis of the multilayers can be changed from more in-plane to out-of-plane by controlling the thickness of LNO layers. The anomalous Hall resistance loops of symmetric and asymmetric multilayer show hump-like features. The results are discussed based on microstructure, magnetic properties, and transport analysis, with details presented below.

6.3 Experimental details

The multilayers studied here, 4LNO/(10SRO/4LNO)*6, 2LNO/(10SRO/2LNO)*6, and the reference sample 4LNO/6SRO/4LNO) were grown on $SrTiO_3$(STO) (100) by pulsed-laser deposition (PLD) technique. The STO single-crystal substrate was prepared by NH_4F-buffered HF etching for 2-2.5 min and annealing at 1000 °C for 2 hours in the air. Epitaxial SRO and LNO were deposited with partial pressure of 0.133 mbar and 0.3 mbar at 700 °C, respectively. A KrF excimer laser (wavelength = 248 nm) was delivered on a stoichiometric SRO and LNO target with a laser fluence of 3 J/cm^2. The pulse repetition rate of the laser was 5 Hz for the $SrRuO_3$ layers and 1 Hz for LNO layers, respectively. The growth of each layer was monitored by high oxygen pressure reflective high-energy electron diffraction (RHEED). The thickness of each $SrRuO_3$ layer is nominally 6 or 10 monolayers (ML), and the thickness of each $LaNiO_3$ layer is nominally 2 or 4 MLs (1 ML layer is ~0.4 nm thick). The samples were cooled in a 100-mbar oxygen atmosphere from 700℃ down to room temperature with a rate of 10 ℃/minute.

The microstructure of the multilayers was investigated by high angle annular dark-field scanning transmission electron microscopy (HAADF-STEM) of cross-section specimens. For the 4LNO/(10SRO/4LNO)*6 and 4LNO/6SRO/4LNO, the cross-sectional TEM specimens were prepared by a standard procedure that included mechanical grinding, tripod polishing, and argon ion beam milling in a stage cooled with liquid nitrogen. The elements distribution of samples was characterized by an FEI Titan 80–200 ChemiSTEM microscope with energy dispersive x-ray spectroscopy (EDS) mapping. The magnetization of all the samples was measured with a superconducting quantum interference device (SQUID) magnetometer (MPMS XL7 from Quantum Design, magnetic field up to 7 T). The surface morphology of our samples was characterized by atomic force microscopy (NX10, Park Systems). A homemade setup enables the simultaneous measurement of transverse Hall resistance in van der Pauw configuration and the polar magneto-optical Kerr effect (MOKE).

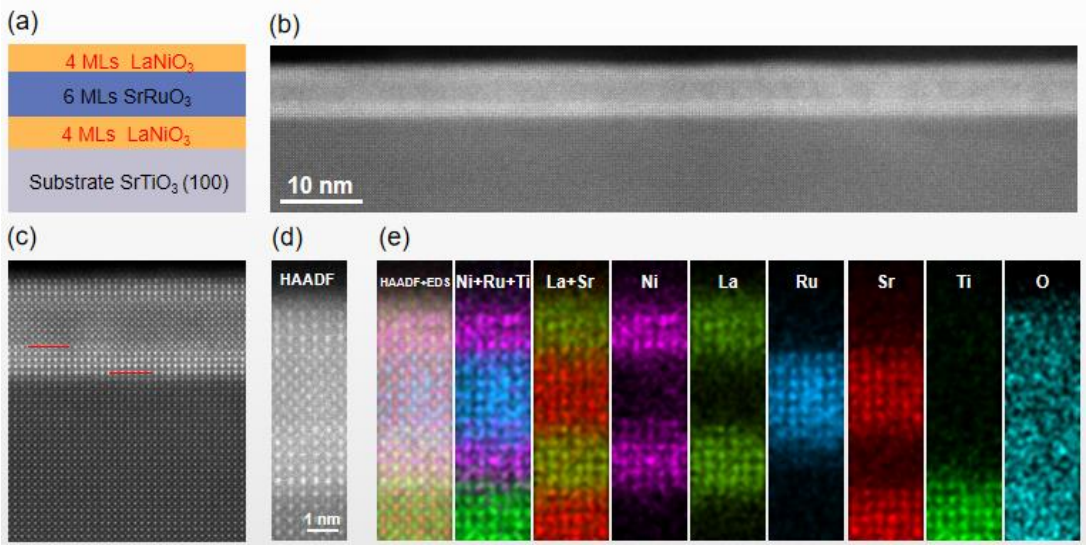

Figure 6.1: Microstructure of 4LNO/6SRO/4LNO heterostructure (a) schematic of the sample, (b) HAADF-STEM cross-sectional image, (c) high magnification micrograph, the red lines on the top micrograph indicate a region where the spacer $LaNiO_3$ layer has a one unit cell thickness step at the top interface, (d) an high magnification micrograph, (e) EDX elemental mapping of all the cations of the layers across the heterostructure in the area shown in (d) (Ni purple, La light green, Ru blue, Sr red, Ti green, O Cyan colors).

Silver paint was used to prepare the electrodes for the electrical measurements, and thin copper wires were used as connecting leads. The transverse Hall resistance R_{xy} can be expressed as the ratio of the Hall voltage and the excitation current I[40]. We acquired simultaneously Hall resistance and Kerr rotation hysteresis loops under the same field sweeping rates of 0.3 Tesla/min. The polar MOKE studies were performed with the magnetic field applied perpendicular to the thin film surface with incoherent light from a Xe lamp. Light of 560 nm wavelength was used for the sample 4LNO/(10SRO/4LNO)*6 multilayers, 570 nm wavelength was used for 2LNO/(10SRO/2LNO)*6, 520 nm wavelength was used for 4LNO/6SRO/4LNO, respectively.

6.4 Results and discussion

6.4.1 Investigation of microstructure

Figure 6.1 shows the growth characterization of the LNO/SRO/LNO heterostructures films. Figure 6.1(a) shows the schematic of the samples. The interface of the sample was observed in low magnification high angle annular dark-field (HAADF) STEM mode as shown in figure 6.1(b), with the layer sequence matching exactly the schematic sequence in figure 6.1(a). The high magnification HAADF-STEM micrograph is shown in figure 6.1(c) and highlights the three layers of the 4LNO/6SRO/4LNO heterostructure, which clearly indicate the separated layers and thickness of each layer. The steps feature at the interface was observed. To further investigate the

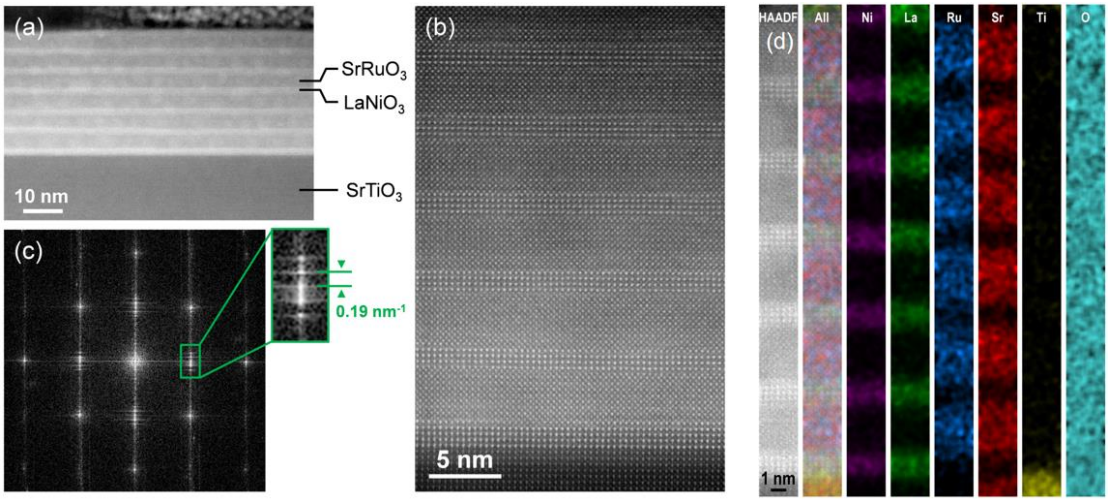

Figure 6.2: Microstructure of 4LNO/(10SRO/4LNO)*6 heterostructure (a) HAADF-STEM cross-sectional image, (b) high magnification HAADF-STEM micrograph, (c) FFT pattern obtained from the image shown in (b), (d) EDX elemental mapping all the cations of the layers across the heterostructure (Ni purple, La light green, Ru blue, Sr red, Ti green, O Cyan). colors).

heterostructure, we show arbitrary zoom area of high magnification micrographs, as shown in figure 6.1(d). Corresponding to the zoomed magnification micrograph, figure 6.1(e) displays the distribution of the chemical elements across the entire stack investigated by high-resolution EDX and enables us to check their uniform distribution and sharp interface. The slight observable signal intermixing, such as Sr traces at the adjacent Sr and La layers or Ni traces at the adjacent Ni and Ru layers, can be caused by electron beam spreading within the sample due to scattering delocalization. Therefore, here we cannot rule out an off - stoichiometry or intermixing for the sample.

Similarly, figure 2 shows a summary of the HAADF-STEM cross-sectional investigations of the 4LNO/(10SRO/4LNO)*6 multilayer: an overview image (see figure 6.2. (a)), a high magnification micrograph (see figure 6.2. (b)), and EDX elemental mapping of all the cations of the layers across the 4LNO/(10SRO/4LNO)*6 heterostructure (see figure 6.2. (d)) which imply the growth of layer sequence, the thickness of each layer, and elements of distribution as good as expected. In figure 6.2(c), a fast Fourier transform (FFT) of the STEM image is shown: the superlattice satellites spots marked with the green rectangle confirm the regular periodicity of the multilayer and the absence of the half-order refelctions indicate that the structure of the $SrRuO_3$ layers is not orthorhombic at room temperature [44]. The absence of diffraction spots may be summarized as: i) no or suppressed oxygen octahedra tilts in the structure; ii) too week intensity to be detected by this means.

6.4.2 Magnetic anisotropy

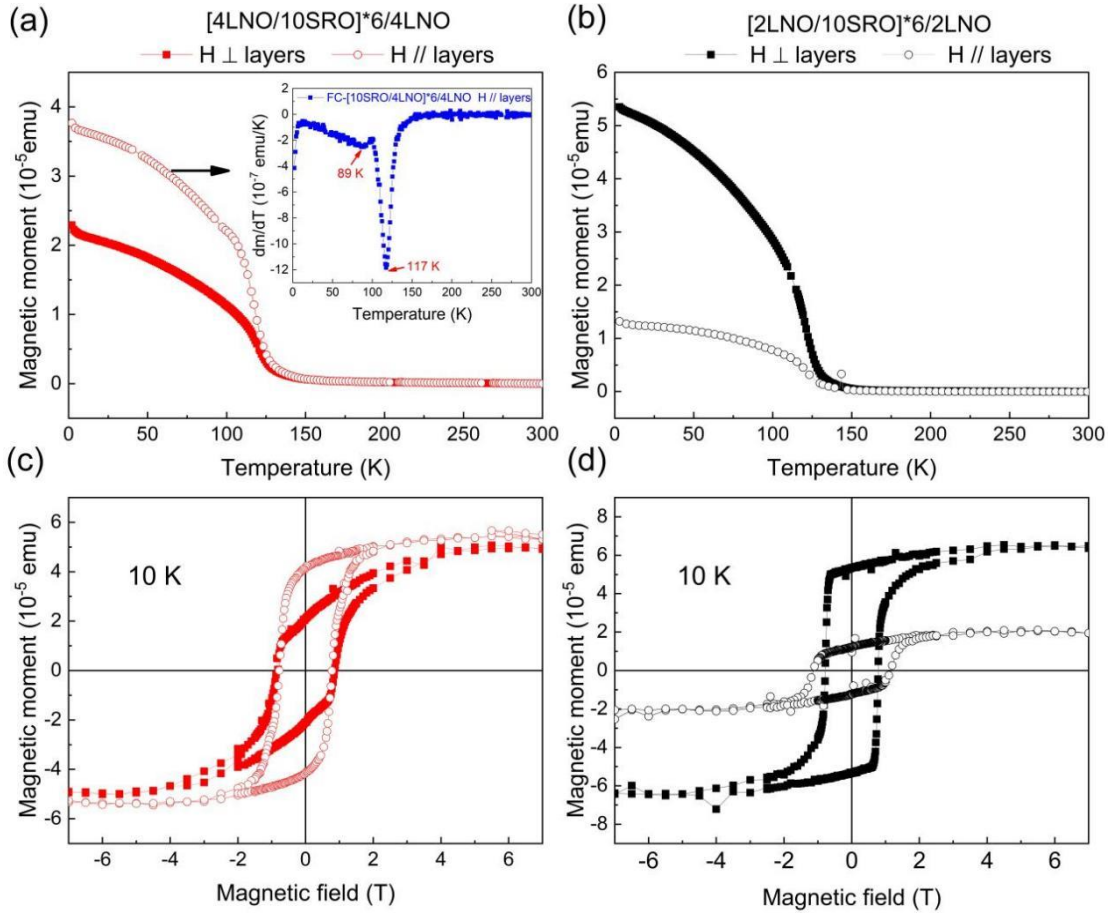

Figure 6.3: Comparison of the magnetic moments as a function of temperature and magnetic field of the (4LNO/(10SRO/4LNO)*6 and 2LNO/(10SRO/2LNO)*6 multilayers: (a) and (b) Magnetic moments as a function of temperature measured with field cooling (FC) mode; (c) and (d) Magnetic moments as a function of applied field along different directions (parallel and perpendicular to the layers) at 10 K.

To probe the magnetic anisotropy of the 4LNO/(10SRO/4LNO)*6 and 2LNO/(10SRO/2LNO)*6 multilayers, the measurement of temperature and magnetic field dependence of magnetic moment, i.e., M(T) and M(H), was done with the magnetic field directed along the different crystallographic direction. In figures 6.3(a) and 6.3(b), the magnetic moment of 4LNO/(10SRO/4LNO)*6 and 2LNO/(10SRO/2LNO)*6 multilayers were measured as a function of the temperature in a 0.1 T external magnetic field applied along with the film normal (the red or black solid-dot line) and parallel to the film surface (the red or black dash-dot line) during field cooling, respectively. For 2LNO/(10SRO/2LNO)*6, show the typically out-of-plane magnetic anisotropy. That is, the easy axis of the sample tends to align to sample normal rather than parallel to the sample surface, which is typical for $SrRuO_3$ layers of this thicknes deposited on $SrTiO_3$(100). While when the thickness of LNO layers increased to 4 MLs, the FC magnetization of the multilayer obtained in the magnetic field parallel to the surface of the sample were larger than the FC magnetic moments detected in the magnetic field along with the film normal, which means the easy axis

of the sample changed toward in-plane orientation.

In addition, we show the temperature dependence of the magnetization loops at 10 K in out-of-plane and in-plane magnetic field, as presented in figures 6.3(c) and 6.3(d). The diamagnetic contributions of the substrate, and of the ferromagnetic impurity introduced during the sample cutting and of the background were subtracted[9,41]. In agreement with the M(T) data, the in-plane hysteresis loop has a large saturation magnetization and the largest remnant magnetization at 10 K, indicating that the easy axis lies close to the in-plane direction for the multilayer with 4 MLs LNO spacers. To determine the Curie of 4LNO/(10SRO/4LNO)*6, we get the derivative of the M(T) curve, which shows two Curie temperature at 89 K and 117 K. The origin of these two transition temperatures may come from the slight homogeneity of the multilayer, similar to the case of the $SrRuO_3/SrIrO_3$ multilayers

As we stated at the beginning of this chapter, the rotations of oxygen octahedra can leadsto the change of magnetocrystalline anisotropy, and possibly this occurs in the two multilayer. Thsmeans that additional investigation of the distortionsof the oxygen octahedra at the interfaces is necessary to understand the strong modification of the magnetocrystalline anisotropy in the two multilayers. More precisely, high-resolution HAADF and ABF imaging, which are simultaneously acquired and enables us to image all the elements (Sr/La, Ru/Ni, and O) in the sample, can be used for the investigation of the atomic distortion at the interfaces. The oxygen octahedral tilting at the interfaces can be obtained from the atomic structure calculation and STEM image simulation[42-49].

6.4.3 Anomalous Hall effect (AHE) resistance and Kerr rotation

Our former work demonstrated that the origin of the hump anomalies in the Hall resistance loops of ultrathin $SrRuO_3/SrIrO_3$ multilayers could be attributed to the unavoidable differences in the electronic and magnetic properties of the individual $SrRuO_3$ layers[40]. Hence, we are also interesetd about the Hall effect of the SRO/LNO multilayers. Since the single LNO layer does not show strong SOC and shows paramagnetic properties, it means that if the hump anomalies in the Hall resistance loops of the sample were observed, one cannot attribute the hump-like features to the skyrmion[5].

I investigated the evolution of magnetotransport properties of SRO/LNO multilayers with different thicknesses and stacking. We characterized the transverse magnetotransport of these samples. The Hall resistance of samples can be expressed as $R_{xy} = R_{xy}^{OHE} + R_{xy}^{AHE}$, where the first term is the ordinary Hall resistance due to the Lorentz force and the second term is the anomalous Hall (AH) resistance (R_{xy}^{AH}), which is proportional to the out-of-plane magnetization of the films[50]. In figure 6.4, we show the anomalous Hall resistance loops and MOKE rotation angle loops of

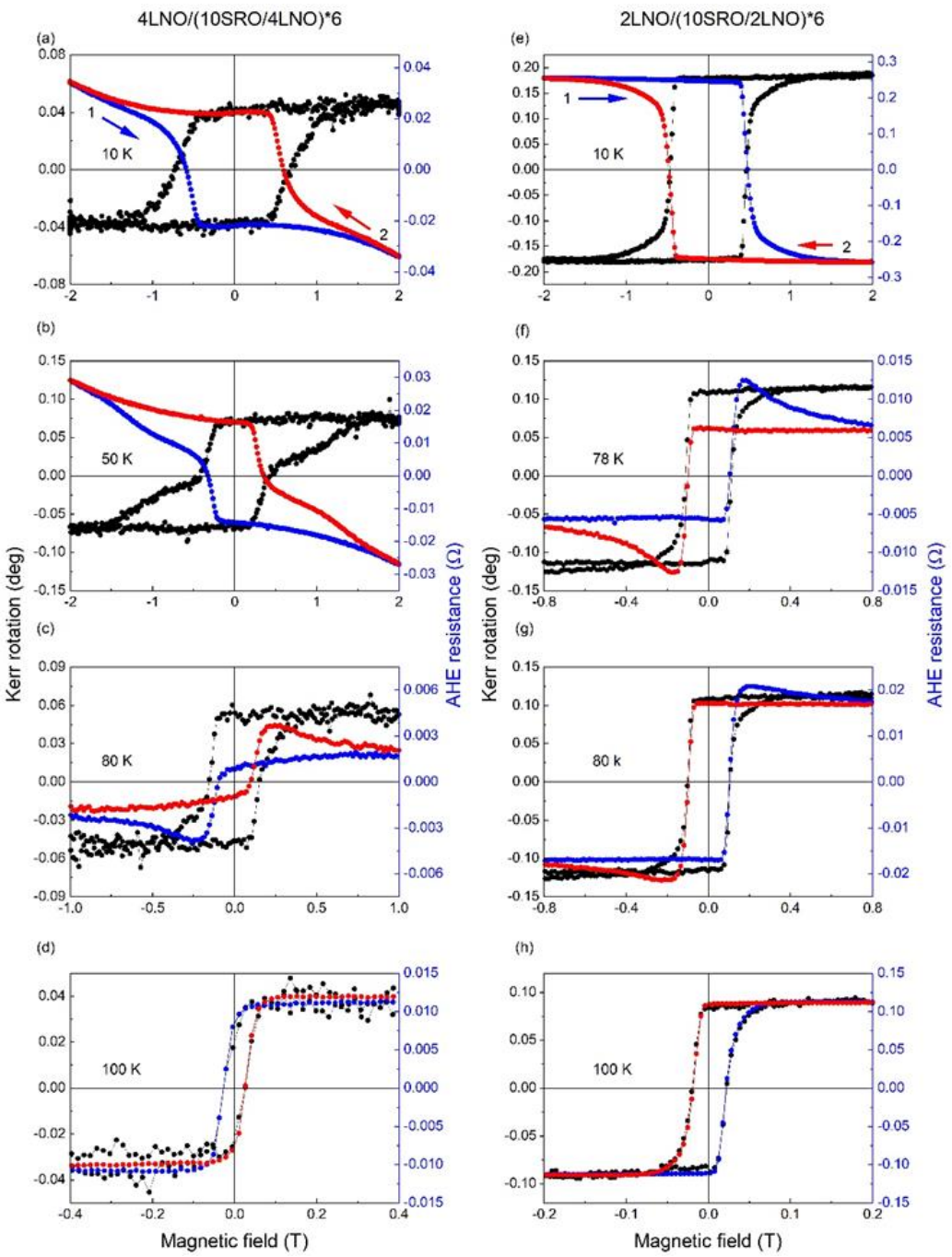

Figure 6.4: Comparison of anomalous Hall resistance loops (blue: the first half marked as 1, the rest marked as 2 and red) and of the MOKE rotation angle loops (black) measured at 10 K, 50 K, 80 K, and 100 K or at 10 K, 78 K, 80 K, and 100 K for sample 4LNO/(10SRO/4LNO)*6 and 2LNO/(10SRO/2LNO)*6, respectively.

4LNO/(10SRO/4LNO)*6 and 2LNO/(10SRO/2LNO)*6 at the temperature range of 10-100 K. Here, we note that the ordinary Hall resistance and the background and impurity contribution are subtracted from the total Hall resistance for the Hall loops and Kerr rotation angle for Kerr loops shown subsequently throughout the paper.

The main features of the data for these two multilayers can be extracted as the

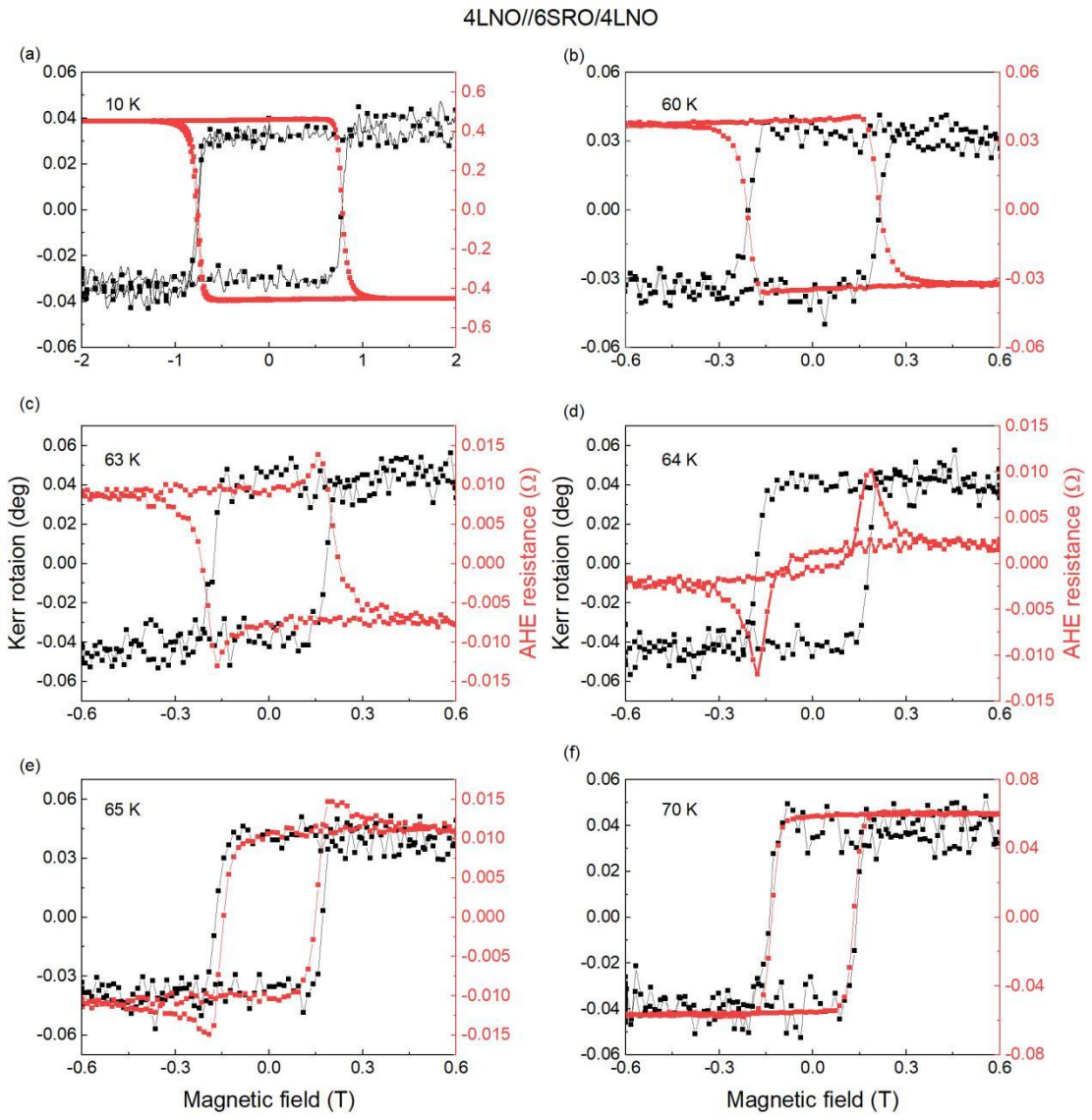

Figure 6.5: MOKE rotation angle loops (black) and the anomalous Hall resistance loops (red) measured at 10 K, 60 K, 63K, 64 K, 65 K, and 70 K for 4LNO/6SRO/4LNO trilayer reference sample are compared. Hump-like features appear in the Hall loops around 63 K, where the AHE changes its sign from negative to positive.

following points. First, the AHE resistance and MOKE loops show similar coercive fields at all temperatures, which means the two different measurements can detect the domain reversion and confirm that the coercive fields inferred by the AHE resistance loops agree with those determined by MOKE loops. However, the hump-like feature only occurs in AHE resistance loops but not in MOKE loops because the AHE resistance loops do not directly scale only with the evolution of magnetic domain[40,41,51]. Second, the hump-like features appear in the AHE loops for these symmetric multilayers without DMI, which means other sources than skyrmions and their topological Hall effect introduce the hump anomalies of the AHE hysteresis loops. Considering the steps features at the interface in STEM images for the 4LNO/6SRO/4LNO heterostructure, we assume that the hump-like features originate

from the inhomogeneity of multilayers which have several magnetic channels with distinct coercive fields and different temperatures at which the intrinsic AHE conductivity changes sign[52-54] TThe anomalous Hall resistances exhibit a sign change from negative (at low temperatures) to positive (at high temperatures) which is typical for $SrRuO_3$ epitaxial films as well as single crystals due to the sign change of the intrinsic anomalous Hall conductivity. In addition, the rotation of oxygen octahedral can be attributed to the hump-like features in the AHE resistance loops as M. Ziese *et al*. confirmed the $Pr_{0.7}Ga_{0.3}MnO_3/SRuO_3$ show interfacial oxygen octahedral tilting[55].

However, the difference in AHE resistance or MOKE loops for the two samples is also obvious. Firstly, the AHE resistance loops of the 4LNO/(10SRO/4LNO)*6 show the bend curve features at a high magnetic field but not for 2LNO/(10SRO/2LNO)*6 due to the 4 MLs metallic LNO with different ordinary Hall effect constants[56]. Then the MOKE loops of 4LNO/(10SRO/4LNO)*6 present the wasp-waisted features at 50 K and 100 K while they show a more square shape for 2LNO/(10SRO/2LNO)*6, which means the domain structure is more complex probably due to the rotation of the easy axis. Thus, we can infer that decreasing the thickness of LNO from 4 MLS to 2 MLs can tune the easy axis from in-plane to out-of-plane.

For the further investigation of the origin of the hump-like features of the multilayers, we characterize the AHE resistances angle of a symmetric 4LNO/6SRO/4LNO heterostructure (see figure 6.5). The main features of the AHE and MOKE loops for the sample, such as the hump-like features, the similar coercive field, and the sign change of AHE resistance, are quite similar to 4LNO/(10SRO/4LNO)*6 and 2LNO/(10SRO/2LNO)*6. We strength that the AHE resistance loops of the 4LNO/6SRO/4LNO show the obvious humps-like features again at narrow temperature ranges 63 K - 65 K, which is similar to that of the 2LNO/(10SRO/2LNO)*6, but different with other literature which stated skyrmions show at a larger temperature range for $SrRuO_3$ based heterostructures or $SrRuO_3$ signal layer[5,32,57]. Here we strengthen again that the 2 MLs or 4MLs are paramagnetic, and thus the AHE originates from the $SrRuO_3$ layers. In addition, the LNO layers show no strong SOC, and there is no DMI for the sample. The humps-like features of AHE loops tend to come from the inhomogeneity of the sample with differences in electronic and magnetic properties of the individual $SrRuO_3$ layers for 4LNO/(10SRO/4LNO)*6, 2LNO/(10SRO/2LNO)*6, while the humps-like features generated by the interfaces with different magnetic properties for 4LNO/6SRO/4LNO[2,40].

6.5 Conclusion

In summary, we studied the tailoring of magnetic anisotropy and the occurrence of hump-like features in AHE resistance loops for symmetric $SrRuO_3/LaNiO_3/SrRuO_3$ multilayers or asymmetric $LaNiO_3/SrRuO_3$ multilayers. To investigate magnetic anisotropy, we mainly performed measurements of the temperature and magnetic field dependence of magnetic moment by SQUID. The origin of magnetic anisotropy change

was revealed by atomic structure calculation and STEM image simulation. The symmetric $SrRuO_3/LaNiO_3/SrRuO_3$ multilayers and asymmetric $LaNiO_3/SrRuO_3$ multilayers, the magnetic anisotropy axes can be controlled from in-plane to out-of-plane by decreasing the thickness of $LaNiO_3$ layers from 4 MLs to 2 MLs probably due to the different oxygen octahedral connectivity at the $SrRuO_3$ /$LaNiO_3$ interfaces, which cause changes of the octahedral tilt angles and bond lengths and thus tune the effective magnetocrystalline anisotropy. Meanwhile, the strong interlayer coupling in the multilayers with 4 MLs LNO maybe also contribute to the tailoring of magnetic anisotropy. To study the magnetotransport of samples, we simultaneously measured the AHE and MOKE Kerr rotation angle loops by a homemade setup. The AHE resistance loops show hump-like features for the symmetric multilayers ((2LNO/(10SRO/2LNO)*6), (4LNO/(10SRO/4LNO)*6), and 4LNO/6SRO/4LNO). Considering the absence of strong SOC for $LaNiO_3$ layers and symmetry of the structure of multilayers, we conclude that the hump-like features most possibly originate from the inhomogeneous magnetic and electrical properties of individual $SrRuO_3$ layers and different magnetic properties at $LaNiO_3/SrRuO_3$ interfaces rather than the formation of skyrmions. I expect my work to promote the research on the spintronics with faerromagnetic oxide heterostructures.

6.6 References

1 X. K. Ning, Z. J. Wang, and Z. D. Zhang, Journal of Applied Physics **117** (9), 093907 (2015).

2 D. J. Groenendijk, C. Autieri, T. C. van Thiel, W. Brzezicki, J. R. Hortensius, D. Afanasiev, N. Gauquelin, P. Barone, K. H. W. van den Bos, S. van Aert, J. Verbeeck, A. Filippetti, S. Picozzi, M. Cuoco, and A. D. Caviglia, Physical Review Research **2** (2), 023404 (2020).

3 J. Xia, W. Siemons, G. Koster, M. R. Beasley, and A. Kapitulnik, Phys Rev B **79** (14), 140407 (2009).

4 Z. Wang, H. P. Nair, G. C. Correa, J. Jeong, K. Lee, E. S. Kim, A. Seidner H, C. S. Lee, H. J. Lim, D. A. Muller, and D. G. Schlom, APL Materials **6** (8), 086101 (2018).

5 J. Matsuno, N. Ogawa, K. Yasuda, F. Kagawa, W. Koshibae, N. Nagaosa, Y. Tokura, and M. Kawasaki, Science Advances **2** (7), e1600304 (2016).

6 M. Ziese and I. Vrejoiu, Physica status solidi (RRL) – Rapid Research Letters **7** (4), 243 (2013).

7 G. Koster, L. Klein, W. Siemons, G. Rijnders, J. S. Dodge, C.-B. Eom, D. H. A. Blank, and M. R. Beasley, Reviews of Modern Physics **84** (1), 253 (2012).

8 M. Kim and B. I. Min, Phys Rev B **91** (20), 205116 (2015).

9 M. Ziese, I. Vrejoiu, and D. Hesse, Phys Rev B **81** (18), 184418 (2010).

10 Y. Kats, I. Genish, L. Klein, J. W. Reiner, and M. R. Beasley, Phys Rev B **71** (10), 100403 (2005).

11 L. Klein, Y. Kats, A. F. Marshall, J. W. Reiner, T. H. Geballe, M. R. Beasley, and A. Kapitulnik, Physical Review Letters **84** (26), 6090 (2000).

12 A. Rastogi, M. Brahlek, J. M. Ok, Z. Liao, C. Sohn, S. Feldman, and H. N. Lee, APL Materials **7** (9), 091106 (2019).

13 Z. Q. Liu, Y. Ming, W. M. Lü, Z. Huang, X. Wang, B. M. Zhang, C. J. Li, K. Gopinadhan, S. W. Zeng, A. Annadi, Y. P. Feng, T. Venkatesan, and Ariando, Applied Physics Letters **101** (22), 223105 (2012).

14 S. Thota, S. Ghosh, S. Nayak, D. C. Joshi, P. Pramanik, K. Roychowdhury, and S. Das, Journal of Applied Physics **122** (12), 124304 (2017).

15 O. F. Shoron, S. Raghavan, C. R. Freeze, and S. Stemmer, Applied Physics Letters **110** (23), 232902 (2017).

16 B. Dieny, V. S. Speriosu, S. S. P. Parkin, B. A. Gurney, D. R. Wilhoit, and D. Mauri, Phys Rev B **43** (1), 1297 (1991).

17 X. Martí, F. Sánchez, J. Fontcuberta, M. V. García-Cuenca, C. Ferrater, and M. Varela, Journal of Applied Physics **99** (8), 08P302 (2006).

18 J. M. Rondinelli, M. Stengel, and N. A. Spaldin, Nat Nanotechnol **3** (1), 46 (2008).

19 M. Bibes, J. E. Villegas, and A. Barthélémy, Advances in Physics **60** (1), 5 (2011).

20 S. Lin, Q. Zhang, M. A. Roldan, S. Das, T. Charlton, M. R. Fitzsimmons, Q. Jin,

S. Li, Z. Wu, S. Chen, H. Guo, X. Tong, M. He, C. Ge, C. Wang, L. Gu, K.-J. Jin, and E.-J. Guo, Physical Review Applied **13** (3), 034033 (2020).

21 S. Yan, Z. Li, D. Wang, and W. Mi, The Journal of Physical Chemistry C, **125** (43), 24052 (2021).

22 W. Kang, C. Zheng, Y. Huang, X. Zhang, Y. Zhou, W. Lv, and W. Zhao, IEEE Electron Device Letters **37** (7), 924 (2016).

23 R. Tomasello, V. Puliafito, E. Martinez, A. Manchon, M. Ricci, M. Carpentieri, and G. Finocchio, Journal of Physics D: Applied Physics **50** (32), 325302 (2017).

24 E. J. Moon, P. V. Balachandran, B. J. Kirby, D. J. Keavney, R. J. Sichel-Tissot, C. M. Schlepütz, E. Karapetrova, X. M. Cheng, J. M. Rondinelli, and S. J. May, Nano Letters **14** (5), 2509 (2014).

25 W. Lu, W. Song, P. Yang, J. Ding, G. M. Chow, and J. Chen, Scientific Reports **5** (1), 10245 (2015).

26 D Sander, Journal of Physics: Condensed Matter Sander, **16** (20), R603 (2004).

27 A. Grutter, F. Wong, E. Arenholz, M. Liberati, and Y. Suzuki, Journal of Applied Physics **107** (9), 09E138 (2010).

28 Z. Liao, M. Huijben, Z. Zhong, N. Gauquelin, S. Macke, R. J. Green, S. Van Aert, J. Verbeeck, G. Van Tendeloo, K. Held, G. A. Sawatzky, G. Koster, and G. Rijnders, Nature Materials **15** (4), 425 (2016).

29 Z. Jiang, J. Zhang, D. Song, M. Zhu, W. Liu, Q. Wu, L. Ge, Z. Liao, Y. Yang, H. Huang, J. Wang, Z. Fu, and Y. Lu, Ceramics International **48** (12), 16825 (2022).

30 A. Huang, H.-T. Jeng, and C.-H. Chang, ACS Applied Nano Materials, (2021).

31 G. Herranz, F. Sánchez, N. Dix, D. Hrabovsky, I. C. Infante, J. Fontcuberta, M. V. García-Cuenca, C. Ferrater, and M. Varela, Applied Physics Letters **89** (15), 152501 (2006).

32 K.-Y. Meng, A. S. Ahmed, M. Baćani, A.-O. Mandru, X. Zhao, N. Bagués, B. D. Esser, J. Flores, D. W. McComb, H. J. Hug, and F. Yang, Nano Letters **19** (5), 3169 (2019).

33 S. Luo and L. You, APL Materials **9** (5), 050901 (2021).

34 L. Wang, Q. Feng, Y. Kim, R. Kim, K. H. Lee, S. D. Pollard, Y. J. Shin, H. Zhou, W. Peng, D. Lee, W. Meng, H. Yang, J. H. Han, M. Kim, Q. Lu, and T. W. Noh, Nature Materials **17** (12), 1087 (2018).

35 A. Soumyanarayanan, M. Raju, A. L. G. Oyarce, A. K. C. Tan, M.-Y. Im, A. P Petrović, Pin Ho, K. H. Khoo, M. Tran, C. K. Gan, F. Ernult, and C. Panagopoulos, Nature Materials **16** (9), 898 (2017).

36 C. Moreau-Luchaire, C. Moutafis, N. Reyren, J. Sampaio, C. A. F. Vaz, N. Van Horne, K. Bouzehouane, K. Garcia, C. Deranlot, P. Warnicke, P. Wohlhüter, J. M. George, M. Weigand, J. Raabe, V. Cros, and A. Fert, Nat Nanotechnol **11** (5), 444 (2016).

37 K. Terai, T. Ohnishi, M. Lippmaa, H. Koinuma, and . Kawasaki, Japanese

Journal of Applied Physics **43** (No. 2A), L227 (2004).

[38] C.-Z. Hu, Y.-S. Zhang, X. Niu, N. Zhong, P.-H. Xiang, and C.-G. Duan, J Applied Physics Letters, **118** (7), 072407 (2021).

[39] L. Yang, L. Jin, L. Wysocki, J. Schöpf, D. Jansen, B. Das, L. Kornblum, P. H. M. van Loosdrecht, and I. Lindfors-Vrejoiu, Phys Rev B **104** (6), 064444 (2021).

[40] L. Yang, L. Wysocki, J. Schöpf, L.Jin, A. Kovács, F. Gunkel, R. Dittmann, P. H. M. van Loosdrecht, and I. Lindfors-Vrejoiu, Physical Review Materials **5** (1), 014403 (2021).

[41] L. Wysocki, J. Schöpf, M. Ziese, L. Yang, A. Kovács, L. Jin, R. B. Versteeg, A. Bliesener, F. Gunkel, L. Kornblum, R. Dittmann, P. H. M. van Loosdrecht, and I. Lindfors-Vrejoiu, ACS Omega **5** (11), 5824 (2020).

[42] Z. Li, D. Song, R. Yu, B. Ge, Z. Liao, Y. Li, S. Dong, and J. Zhu, ACS Applied Materials & Interfaces **8** (36), 24192 (2016).

[43] R. Aso, D. Kan, Y. Shimakawa, and H. Kurata, Scientific Reports **3** (1), 2214 (2013).

[44] Z. Liao, Z. Li, and J. Zhu, Journal of the American Ceramic Society **99** (11), 3734 (2016).

[45] Y. Gu, Y.-W. Wei, K. Xu, H. Zhang, F. Wang, F. Li, M. S. Saleem, C.-Z. Chang, J. Sun, C. Song, J. Feng, X. Zhong, W. Liu, Z. Zhang, J. Zhu, and F. Pan, Journal of Physics D: Applied Physics **52** (40), 404001 (2019).

[46] S. G. Jeong, G. Han, S. Song, T. Min, A. Y. Mohamed, S. Park, J. Lee, H. Y. Jeong, Y.-M. Kim, D.-Y. Cho, and W. S. Choi, Advanced Science **7** (16), 2001643 (2020).

[47] A. Y. Borisevich, H. J. Chang, M. Huijben, M. P. Oxley, S. Okamoto, M. K. Niranjan, J. D. Burton, E. Y. Tsymbal, Y. H. Chu, P. Yu, R. Ramesh, S. V. Kalinin, and S. J. Pennycook, Physical Review Letters **105** (8), 087204 (2010).

[48] Y. Wang, U. Salzberger, W. Sigle, Y. E. Suyolcu, and P. A. van Aken, Ultramicroscopy **168**, 46 (2016).

[49] M. W. Lufaso and P. M. Woodward, Acta crystallographica. Section B, Structural science **57** (Pt 6), 725 (2001).

[50] C. Hurd, *The Hall effect in metals and alloys*. (Springer Science & Business Media, 2012).

[51] G. Malsch, D. Ivaneyko, P. Milde, L. Wysocki, L. Yang, P. H. M. van Loosdrecht, I. Lindfors-Vrejoiu, and L. M. Eng, ACS Applied Nano Materials **3** (2), 1182 (2020).

[52] Z. Fang, N. Nagaosa, K. S. Takahashi, A. Asamitsu, R. Mathieu, T. Ogasawara, H. Yamada, M. Kawasaki, Y. Tokura, and K. Terakura, **302** (5642), 92 (2003).

[53] N. Haham, Y. Shperber, M. Schultz, N. Naftalis, E. Shimshoni, J. W. Reiner, and L. Klein, Phys Rev B **84** (17), 174439 (2011).

[54] I. Lindfors-Vrejoiu and M. Ziese, **254** (5), 1600556 (2017).

[55] M. Ziese, L. Jin, and I. Lindfors-Vrejoiu, Journal of Physics: Materials, **2** (3), 034008 (2019).

[56] M. Golalikhani, Q. Lei, R. U. Chandrasena, L. Kasaei, H. Park, J. Bai, P. Orgiani,

J. Ciston, G. E. Sterbinsky, D. A. Arena, P. Shafer, E. Arenholz, B. A. Davidson, A. J. Millis, A. X. Gray, and X. X. Xi, Nature Communications **9** (1), 2206 (2018).

[57] Y. Gu, Y.-W. Wei, K. Xu, H. Zhang, F. Wang, F. Li, M. S. Saleem, C.-Z. Chang, J. Sun, C. Song, J. Feng, X. Zhong, W. Liu, Z. Zhang, J. Zhu, and F. Pan, Journal of Physics D: Applied Physics **52** (40), 404001 (2019).

Chapter 7 Summary and Outlook

Contents

7.1 Summary and Outlook

The work summarized in the thesis aims to investigate intriguing physical phenomena, i.e., anomalous Hall effect (AHE), magnetic interlayer coupling, and magnetic anisotropy in ferromagnetic oxide epitaxial multilayers for understanding how to control them and potentially make use of them in applications. I carried out studies mainly with $SrRuO_3$-based heterostructure and multilayers. A strong motivation for this choice was that heterostructures of $SrRuO_3/SrIrO_3$ were considered to have strong interfacial Dzyaloshinskii-Moriya interaction (DMI) due to the broken spatial inversion symmetry and the strong spin-orbit coupling in $SrIrO_3$, which would result in the formation of small Néel skyrmions.

The detection of skyrmions with an available approach for most of the research groups, i.e., magnetotransport measurement, has been intensively investigated since the interpretation of the observed humps in AHE resistance loops of $SrRuO_3/SrIrO_3$, bilayers as a fingerprint of the contribution of the topological Hall effect (THE) of skyrmions. However, increasing numbers of researchers doubted the reliability of the Hall measurements proof for the existence of skyrmion, because the hump-like features can also be explained by the two-channel AHE model or inhomogeneity. In chapter four, we prepared different $SrRuO_3/SrIrO_3/SrRuO_3$ symmetric heterostructures, which disfavor the occurrence of a net interfacial DMI and thus, the formation of skyrmions would not have the proper conditions to form. However, the hump-like structures were observed for the Hall resistance loops of multilayers, in which the trilayer was stacked several times, which is similar to the case of asymmetric $SrRuO_3/SrIrO_3$ bilayers. The Hall resistance loops of multilayers, in which the trilayer was stacked several times, did exhibit hump-like structures, similar to that of asymmetric $SrRuO_3/SrIrO_3$ bilayers. The magnetization as a function of temperature combined with the XMCD measurement for the individual $SrRuO_3$ layers and $SrIrO_3$ layers showed that the multilayers probably had a spread of the Curie temperatures, indicating the different magnetic properties of the individual $SrRuO_3$ layers. The origin of the Hall effect anomalies likely can be attributed to the unavoidable structural differences between the individual $SrRuO_3$ layers stacked in epitaxial multilayers. The slight structural differences, such as oxygen octahedra rotation angles, and bond lengths, of the individual ruthenate layers, lead to the inhomogeneous magnetic and electrical properties across the multilayer. Thus, the individual $SrRuO_3$ layers may generate several independent magnetotransport channels leading to the hump-like features of the AHE loops.

Hence, we proved that the presence of the possible magnetic skyrmions and THE in SRO heterostructures need to be determined by a set of complementary techniques, especially by real space observations by means of electron microscopy or magnetic force microscopy. Further theoretical studies on the electronic structure of SRO

heterostructures and understanding better the anomalous Hall effect in these heterostructures are required.

Then, considering a strong ferromagnetic coupling is beneficial to modifying or controlling the magnetic properties of the multilayer system, I studied coupling effects in $SrRuO_3/LaNiO_3$ multilayers systems. Strong ferromagnetic interlayer coupling benefits multilayers with topologically non-trivial magnetic domains propagating across the entire stacking. In chapter five, we found an easy but effective approach to enhance the ferromagnetic interlayer coupling between epitaxial $SrRuO_3$ layers. The metal-insulator transition related to thickness plays a significant role in the change of the interlayer exchange coupling mechanism. More precisely, the multilayer with 4 MLs metallic $LaNiO_3$ (LNO) spacers enables a ferromagnetic coupling via an RKKY type of interlayer exchange coupling. In contrast, the multilayer with 2 MLs insulating $LaNiO_3$ spacer shows weak coupling, which arises from a combination of tunneling through the insulating layer plus possibly the effect of pinholes.

In this work, we show a promising approach to enhance the ferromagnetic interlayer coupling between epitaxial $SrRuO_3$ layers, which contributes to the heterostructure design for ferromagnetic oxide multilayer system with attractive magnetic domains. Still further investigation of the RKKY coupling to understand the stronger interlayer coupling is necessary. For example, the RKKY coupling strength oscillation with the spacer thickness should be strengthened. Moreover, though the bare 4 and 8 MLs bare LNO thin films show the tendency of metal-insulator transition with the thickness decreasing, finding a way to check the conductivity of LNO spacer in multilayers can directly help us further figure out the coupling mechanism. Finally, stemming from this work, it should be valuable to the interlayer coupling in ferromagnetic oxide multilayers with high Curie temperature separated by spacers for the room temperature application.

Finally, effective magnetic anisotropy can tune the magnetic domain structure in ferromagnetic thin films and multilayers. In chapter six, we focus on tailoring the magnetic anisotropy of $SrRuO_3/LaNiO_3$ multilayers between out-of-plane and in-plane configurations, and this tunable magnetic anisotropy may provide a viable approach to stabilize magnetic skyrmions in $SrRuO_3$-based multilayers. We find that the magnetic anisotropy axes of our symmetric $SrRuO_3/LaNiO_3/SrRuO_3$ multilayers and asymmetric $LaNiO_3/SrRuO_3$ multilayers can be tuned from in-plane to out-of-plane by decreasing the thickness of $LaNiO_3$ layers from 4 MLs to 2 MLs probably due to the different oxygen octahedral connectivity at the $SrRuO_3$ /$LaNiO_3$ interfaces, distorting the octahedral tilt angles and bond lengths and then modifies the effective magnetocrystalline anisotropy. Additionally, the strong interlayer coupling in the multilayers with 4 MLs LNO spacers likely may also contribute to the tailoring of magnetic anisotropy. It is also interesting to find the AHE resistance loops of our symmetric multilayers ((2LNO/(10SRO/2LNO)*6), (4LNO/(10SRO/4LNO)*6), and 4LNO/6SRO/4LNO) show hump-like features. This observation confirmed the

conclusions of our work on $SrRuO_3/SrIrO_3$ multilayers, which stressed that the inhomogeneous magnetic and electrical properties of individual $SrRuO_3$ layers can lead to several independent magnetotransport channels.

In conclusion, we can tailor the magnetic anisotropy of $SrRuO_3$-based multilayers by inserting different thicknesses of ultrathin LNO spacers, making use of the thickness-dependent structural distortions and physical properties of perovskite oxides. To investigate octahedral tilt angles, the bond length, and atomic distortion in these multilayers, we should perform high-resolution x-ray diffraction studies and high angle annular dark-field scanning transmission electron microscopy as a function of temperature, as recently performed for bare $SrRuO_3$ films[1], and more in-depth atomic structure calculation is required.

7.2 References

[1] X. Zhang, A. N. Penn, L. Wysocki, Z. Zhang, P. H. M. van Loosdrecht, L. Kornblum, J. M. LeBeau, I. Lindfors-Vrejoiu, and D. P. Kumah, APL Materials **10** (5), 051107 (2022).

List of figures

List of tables

List of abbreviations

DMI Dzyaloshinskii-Moriya interaction
THE topological Hall effect
AHE anomalous Hall effect
MA magnetic anisotropy
IC interlayer coupling
SRO $SrRuO_3$
SIO $SrIrO_3$
SZO $SrZrO_3$
STO $SrTiO_3$
LNO $LaNiO_3$
LAO LaAlO3
MLs Monolayers
SOC spin orbit coupling
MOKE magneto-optical Kerr efffect
AFM atomic force microscopy
FM ferromagnetic
PEM photoelastic modulator
PSPD position sensitive photo detector
XMCD x-ray magnetic circular dichroism
RKKY Rudermann–Kittel–Kasuya–Yosida
MPMS magnetic property measurement system
LTEM Lorentz transmission electron microscopy
SQUID superconducting quantum interference device
SP-STM spin-polarized scanning tunneling microscopy
HAADF-STEM high-angle annular dark field scanning transmission electron microscopy
SPLEEM spin-polarized low energy electron microscopy
STXM scanning transmission x-ray microscopy
SAXS resonant small-angle x-ray scattering
SANS small-angle neutron scattering
OOR oxygen octahedral rotations
RHEED reflection high-energy electron diffraction
MCAE magnetocrystalline anisotropy energy
EDX energy dispersive x-ray spectroscopy
TEM transmission electron microscopy
ARPES angle-resolved photoemission
XAS x-ray absorption spectroscopy
BLS Brillouin light scattering
MIT metal-insulator transition
PLD pulsed-laser deposition

XRD x-ray diffraction
FFT Fourier transform
ZFC zero-field cooling
FC field cooled

Acknowledgments

From the bottom of my heart, I would like to express my sincere gratitude to several people without whom I would not have been able to complete my Ph.D. project.

First, I would like to thank Prof. Paul H. M. van Loosdrecht. Thanks for the decision to let me join the (Optical Condensed Matter Science) OCMS group and for your consistent support and guidance!

Paul, I am incredibly grateful for your guidance, kindness, understanding, and encouragement during the running of this project. Thank you for allowing me to work on my exciting project. I enjoy the atmosphere in our group where people are helpful. I am so grateful to get further support from you and the University of Cologne after ending the China Scholarship Council (CSC) scholarship. Without this help, I am sure I could not finish my Ph.D. thesis. Thank you for suggesting that I changed the topic of my Ph.D. work and recommended I work with my second supervisor Dr. Ionela Lindfors-Vrejoiu. This was a significant turning point in my Ph.D. work and life. You always provided invaluable feedback on my work during our discussions. Thank you for sharing your Ph.D. experience with me. This let me learn how to improve myself and succeed with my Ph.D.. I benefited greatly from your wealth of knowledge and meticulous editing. I am impressed with your guidance on inserting the Helium transport tube. You are an ideal supervisor; I am proud of my time working with you.

Ionela, I would like to express my gratitude and appreciation to you for many things. To begin with, thanks for showing me what qualities a scientist should have, such as critical thinking, curiosity, patience, and creativity. You pointed out we should be careful to conclude about our research findings. You always shared literature, comments on the papers and came out with lots of good ideas during our meeting. Then, I am also thankful to you for supporting me in attending lots of workshops and conferences and cooperating with others, such as the cooperation with Lei Jin (Ernst Ruska-Centre for Microscopy and Spectroscopy with Electrons, Forschungszentrum Jülich), Sonia Francoual, and Jose Renato Linares Mardegan (Deutsches Elektronen-Synchrotron), this provided me the access to communicate with other excellent researchers. I realized again how important it is to be open-minded. In the end, thank you for your kind patience and encouragement. You are always ready to help me with my Ph.D. work. Just as you said, “don’t be shy. If you need any help, ask by any means”. I want to show the highest respect and gratitude to you here. In a word, your insightful feedback pushed me to sharpen my thinking and improve my work to a higher level.

Then I would like to thank my collaborators, Lena Wysocki, Jörg Schöpf, Lei Jin, Daniel Jansen, Felix Gunkel, Regina Dittmann, Brajagopal Das, Lior Kornblum and András Kovács.

Lena, thank you for your help with the growth of samples, SQUID measurements, AFM, and MOKE measurements. The high-quality samples and good measurement designs ensured that we could obtain valuable data. Thanks for sharing your research experience; you are careful, well-organized, and hardworking. Thanks to you for all the fruitful discussion; this helps me to quickly solve problems. Thank you for the relaxed communication about Ph.D. students' life; this let me find a way to balance my life and work.

Jörg, I'd like to acknowledge you for improving MOKE-Hall homemade setup; without your help, I think I would have had to change the topic of my Ph.D. project. Thank you for the assistance of MOKE, Hall, and SQUID measurement. You are kind and helpful; I enjoyed the teamwork with you.

Lei, thanks for your help with STEM measurement and data analysis. You always work efficiently, just as Ionela said, "you are an expert in this field, and you are always the best collaborator in this area." I feel fortunate and grateful for your help through my Ph.D. project.

Daniel, thank you for your help preparing samples and AFM measurements. You are always accommodating and energetic. I also enjoyed the chat with you about the difference between the culture of Germany and China; this helps me get a better understanding of Germany and adapt the life here.

Sonia Francoual and Linares Mardegan, Jose Renato, thanks for your help with the x-ray magnetic circular dichroism (XMCD) measurement and data analysis. Besides, I would like to thank you for your warm welcome when Lena and I arrived at DESY; both of you are very favorable and kindhearted.

András Kovács, Felix Gunkel and Regina Dittmann thank you for the help at Research Centre Jülich with STEM and PLD.

Brajagopal Das and Lior Kornblum, I would like to thank you for helping me record and analyze x-ray diffraction (XRD) data.

Mengmeng Bai, thank you for depositing PMMA by spin coating and fabricating electrodes for some of my samples.

Yongjian Wang, thank you for the magnetotransport resistance measurements, which helped me better understand the magnetic anisotropy, magnetic resistance, and conductivity of the samples.

Xiao Wang, thank you for the correction of my Ph.D. thesis. You always encouraged me a lot and helped me improve my thesis.

I want to thank all our OCMS group members. Jingyi Zhu, was a teacher and my

best friend in Cologne. I still felt touched by your warm welcome when I arrived at Dusseldorf airport and your invitation to celebrate the first Chinese New Year (2017) in Germany. That time was extremely challenging for me since everything was new. Besides, thanks for the fruitful discussion about my work, it happened in the office and during our lunchtime. Finally, thanks a lot for your support on my lab problems and daily life. Raphael German, Philipp Stein, Christoph Boguschewski, and Kuhn Henning: thank you help me translate German to English for different documents. This makes my life easier. Rolf B. Versteeg, Anuja Sahasrabudhe, Julian Wagner, Chris Reinhoffer, Hamoon Hedayat Zadeh Roodsari, Semyon Germanskiy, Zhe Wang, Kestutis Budzinauskas, Yu Mukai and Evgeny Mashkovich: thank you for the discussion about our research topics in the office and during different meetings, it broadened my insight and help me to find the solutions to proceed my project. Omar Abdul-Aziz, it was a pleasure to discuss the thesis writing experience with you. This makes me relax!

Furthermore, I want to thank Prashant Padmanabhan and Fumiya Sekiguchi. You helped me start my lab life in this group and learn the basic theory and technique of the time-resolved magneto-optical Kerr effect (MOKE). It was challenging for me but very interesting and impressive.

My special thanks to Thomas Koethe: you are the second person I met when I joined the OCMP group. You helped me a lot, such as with the accommodation, work contract, extension of visa, expenses for business trips, etc. This made life easier.

I further want to thank our engineer Jens Koch. Thanks for the assistance with my experiment. You are very helpful! I am sure I could not have performed my experiment without interruptions without your help.

I also want to thank many friends, such as Zhiqiang Zeng, Ling Zhao, Wen Yan, Jun Wang, Shuangping Han, LuyaoHuang, Binbin Wang, Ruyan Chen, Jialu Jiang, Liangsheng Wang, Zhiming Zou, Xiao Qu, Lujuan Jia, LuPeng Jia, Congjiang, Xin Ying, all played a vital role in my Ph.D. life and thus definitely made a considerable contribution to the success of my life and work.

In the end, special thanks to my Country, China, and my dear parents, Xiquan Yang and Ziping Tan, my brother Zhi Yang. I couldn’t continue the scientific work and have done my Ph.D. project without your support.

Publications and posters

Papers：

1. L. Wysocki, R. Mirzaaghayev, M. Ziese, **L. Yang**, J. Schöpf, R. B. Versteeg, A. Bliesener, J. Engelmayer, A. Kovács, L. Jin, F. Gunkel, R. Dittmann, P. H. M. van Loosdrecht, and I. Lindfors-Vrejoiu, Magnetic coupling of ferromagnetic $SrRuO_3$ epitaxial layers separated by ultrathin nonmagnetic $SrZrO_3$/$SrIrO_3$, **Appl. Phys. Lett.** 113, 192402 (2018).
2. C.-A. Wang, C.-H. Chang, A. Huang, P.-C. Wang, P.-C. Wu, **L. Yang**, C. Xu, P. Pandey, M. Zeng, R. Böttger, H.-T. Jeng, Y.-J. Zeng, M. Helm, Y.-H. Chu, R. Ganesh, and S.-Q. Zhou, Tunable disorder and localization in the rare-earth nickelates, **Phys. Rev. Materials** 3, 053801 (2019)
3. **L. Yang,** C.-A.Wang, M. Zeng, Z. Hou, Z. Fan, D. Chen, M.-H. Qin, X.-B. Lu, Q. Li, X.-S. Gao, Polarization tunability in multiferroic $DyMn_2O_5$: Influence of Y and Eu co-doping and 3*d*-4*f* exchange"**Solid State Communications** 307,113809 (2020)
4. L. Wysocki, J. Schöpf, M. Ziese, **L. Yang**, A. Kovács, L. Jin, R. B. Versteeg, A. Bliesener, F. Gunkel, L. Kornblum, R. Dittmann, P. H. M. van Loosdrecht, and I. Lindfors-Vrejoiu, Electronic inhomogeneity influence on the anomalous Hall resistivity loops of $SrRuO_3$ epitaxially interfaced with 5d perovskites, **ACS Omega** 5, 5824 (2020).
5. L. Wysocki, **L. Yang,** F. Gunkel, R. Dittmann, P. H. van Loosdrecht, and I. Lindfors-Vrejoiu, Validity of magnetotransport detection of skyrmions in epitaxial $SrRuO_3$ heterostructures, **Phys. Rev. Materials** 4, 054402 (2020).
6. G. Malsch, D. Ivaneyko, P. Milde, L. Wysocki, **L. Yang**, P. H. van Loosdrecht, I. Lindfors-Vrejoiu, and L. M. Eng, Correlating the nanoscale structural, magnetic, and magneto-transport properties in $SrRuO_3$-based perovskite thin films: Implications for oxide skyrmion devices, **ACS Appl. Nano Mater.** 3, 1182 (2020).
7. **L. Yang,** L. Wysocki, J. Schöpf, L. Jin, A. Kovács, F. Gunkel, R. Dittmann, P. H. van Loosdrecht, and I. Lindfors-Vrejoiu, Origin of the hump anomalies in the Hall resistance loops of ultrathin $SrRuO_3$/$SrIrO_3$ multilayers, **Phys. Rev. Materials** 5, 014403 (2021).
8. **L. Yang,** L. Jin, L. Wysocki, J. Schöpf, D. Jansen, B. Das, L. Kornblum, P. H. van Loosdrecht, and I. Lindfors-Vrejoiu, Enhancing the ferromagnetic interlayer coupling between epitaxial $SrRuO_3$ layers, **Phys. Rev. B**, 104,064444 (2021).
9. L. Wysocki, S. E. Ilse, **Lin Yang**, E. Goering, F. Gunkel, R. Dittmann, P. H. M. van Loosdrecht, I. Lindfors-Vrejoiu, Magnetic interlayer coupling between ferromagnetic $SrRuO_3$ layers through a $SrIrO_3$ spacer, **J Appl Phys** 131, 133902 (2022)

Posters：

1. 2019.03.31-04.05 DPG Spring Meeting-Regensburg, Germany, Anomalous Hall

effect and magneto-optical Kerr effect of $SrRuO_3$ based epitaxial multilayers (version I).
2. 2019.9.17-19 seminar “Skyrmionics Workshop for Young Researchers”, Main, Germany, Anomalous Hall effect and magneto-optical Kerr effect of $SrRuO_3$ based epitaxial multilayers (version II).
3. 2019.12.2-5 seminar Binationales Seminar (Britisch-Deutsch): “Skyrmions in Magnetic Materials”, Bad Honnef, Germany, Anomalous Hall effect and magneto-optical Kerr effect of $SrRuO_3$ based epitaxial multilayers (version III).
4. 2020.01.6-8, seminar, Magnetism at the Nanoscale: Imaging-Fabrication–Physics, Bad Honnef, Germany, Anomalous Hall effect and magnetic anisotropy of $SrRuO_3/LaNiO_3$ superlattices grown on $SrTiO_3$ (100).